U. S. Army Communications-Electronics Command

Night Vision & Electronics Sensors Directorate

Title: APPLIED NONLINEAR OPTICS
FOR SENSOR PROTECTION

Author(s): GREGORY J. SALAMO

Address: UNIVERSITY OF ARKANSAS
PHYSICS DEPARTMENT
FAYETTEVILLE, AR 72701

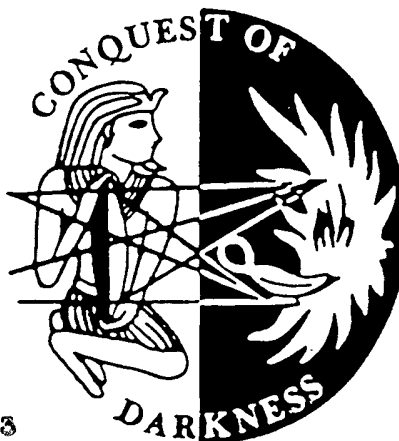**Type of Report (Final, Interim, etc.):**

FINAL REPORT

Date: NOVEMBER 30, 1989 - MAY 31, 1995

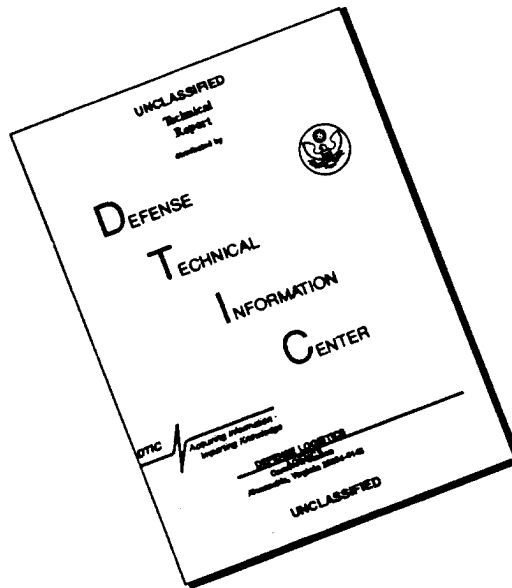## Contract Number

DAAB07-90-C-F402

Report Number

NV-95-C04

DTIC QUALITY INSPECTED 3

CONQUEST OF DARKNESS

Fort Belvoir, Virginia 22060-5806

19960812 182

DISCLAIMER NOTICE

IN REPLY
REFER TO

1 AUG 96

DTIC-OMI

SUBJECT: Distribution Statements on Technical Documents

TO:
   U.S. ARMY COMMUNCATIONS-ELECTRONICS COMMAND
   NIGHT VISION ¢ ELECTRONICS SENSORS DIRECTORATE
   FT. BELVOIR, VA 22060-5806

1. Reference: DoD Directive 5230.24, Distribution Statements on Technical Documents,
18 Mar 87.

2. The Defense Technical Information Center received the enclosed report (referenced
below) which is not marked in accordance with the above reference.

   "APPLIED NONLINEAR OPTICS FOR SENSOR PROTECTION" CONTRACT #DAA807-90-C-F402
   FINAL REPORT FOR PERIOD OF 30 NOV 1989-31 MAY 1995

3. We request the appropriate distribution statement be assigned and the report returned
to DTIC within 5 working days.

4. Approved distribution statements are listed on the reverse of this letter. If you have
any questions regarding these statements, call DTIC's Input Support Branch,
(703) 767-9092, 9088 or 9086 (DSN use prefix 427).

FOR THE ADMINISTRATOR:

1 Encl

CRYSTAL RILEY
Chief, Input Support Branch

FL-171
Dec 95

DoD Directive 5230.24, "Distribution Statements on Technical Documents," 18 Mar 87, contains seven distribution statements, as described briefly below. Technical Documents that are sent to DTIC **must** be assigned one of the following distribution statements:

☒ **DISTRIBUTION STATEMENT A:**

APPROVED FOR PUBLIC RELEASE; DISTRIBUTION IS UNLIMITED.

❑ **DISTRIBUTION STATEMENT B:**

DISTRIBUTION AUTHORIZED TO U. S. GOVERNMENT AGENCIES ONLY; (FILL IN REASON); (DATE STATEMENT APPLIED). OTHER REQUESTS FOR THIS DOCUMENT SHALL BE REFERRED TO (INSERT CONTROLLING DoD OFFICE).

❑ **DISTRIBUTION STATEMENT C:**

DISTRIBUTION AUTHORIZED TO U. S. GOVERNMENT AGENCIES AND THEIR CONTRACTORS; (FILL IN REASON); (DATE STATEMENT APPLIED). OTHER REQUESTS FOR THIS DOCUMENT SHALL BE REFERRED TO (INSERT CONTROLLING DoD OFFICE).

❑ **DISTRIBUTION STATEMENT D:**

DISTRIBUTION AUTHORIZED TO DoD AND DoD CONTRACTORS ONLY; (FILL IN REASON); (DATE STATEMENT APPLIED). OTHER REQUESTS SHALL BE REFERRED TO (INSERT CONTROLLING DoD OFFICE).

❑ **DISTRIBUTION STATEMENT E:**

DISTRIBUTION AUTHORIZED TO DoD COMPONENTS ONLY; (FILL IN REASON); (DATE STATEMENT APPLIED). OTHER REQUESTS SHALL BE REFERRED TO (INSERT CONTROLLING DoD OFFICE).

❑ **DISTRIBUTION STATEMENT F:**

FURTHER DISSEMINATION ONLY AS DIRECTED BY (INSERT CONTROLLING DoD OFFICE AND DATE), OR HIGHER DoD AUTHORITY.

❑ **DISTRIBUTION STATEMENT X:**

DISTRIBUTION AUTHORIZED TO U. S. GOVERNMENT AGENCIES AND PRIVATE INDIVIDUALS OR ENTERPRISES ELIGIBLE TO OBTAIN EXPORT-CONTROLLED TECHNICAL DATA IN ACCORDANCE WITH DoD DIRECTIVE 5230.25 (DATE STATEMENT APPLIED). CONTROLLING DoD OFFICE IS (INSERT).

(Reason)	(Controlling DoD Office Name)
(Assigning Office)	(Controlling DoD Office Address (City/State/Zip)
(Signature & Typed Name)	(Date Statement Assigned)

APPLIED NONLINEAR OPTICS FOR

SENSOR PROTECTION

FINAL REPORT

GREGORY J. SALAMO

DARPA

AWARD NO: DAA B07-90-C-F402

UNIVERSITY OF ARKANSAS

SUMMARY

We have investigated the potential of photorefractive beam fanning as an optical limiting device. Beam fanning is attractive as an optical limiter since it provides the possibility of allowing the outside world to be monitored, while it simultaneously rejects a laser threat. As a device it also has the potential to be sensitive over a broad spectral range, operate with a large field-of-view, provide protection against continuous and pulsed laser sources, protect against a laser threat from any direction, simultaneously block multi-wavelength laser radiation, and to transmit a scene without significant degradation or attenuation.

The major obstacle preventing the beam fanning limiter from reaching this potential has been speed of response. Because the photorefractive beam fanning phenomenon involves charge transport, it is inherently slow. Its relatively slow speed and the corresponding reputation it has acquired, suggests that the beam fanning limiter may not switch fast enough to stop a laser threat before sensor damage occurs.

In the present project we have developed several techniques which are successful in enhancing the photorefractive beam fanning response time. In particular, we demonstrate and characterize the use of applied d.c.and a.c. electric fields, use of a grating to seed the beam fan, use of cylindrical and spherical lens, control of the acceptor and donor concentrations, and control of crystal temperature. Each can lead to an improved response time.

As part of the project we carried out a demonstration of the beam fanning optical limiter. Using a combination of spherical and cylindrical lenses and an applied d.c.electric field, we demonstrated the beam fanning limiter for a laser threat of 1m w/cm^2 over a two inch diameter aperture. The limiter switched in 6 msec with an O.D. of 3 to 4. This limiter, therefore, allows only 6 ujoules to be transmitted before the O.D. of 3 to 4 was in effect. For both higher and lower intensities the limiter switched faster and slower, as expected, still limiting at 6 ujoules with an O.D. of 3 to 4. The demonstration was at the 488 nm and 514.5 nm wavelengths. While the limiter operated, the outside world could still be monitored, a large field-of-view was in effect, and about 50% absorption existed for outside world scenes.

TABLE OF CONTENTS

I. OVERVIEW OF THE PROBLEM

The existence of high powered lasers is a severe threat to all optical sensors. Widespread use of lasers as range finders and target designators makes this threat a present and immediate danger. The human eye, as well as man-made detectors such as the many FLIR devices presently employed in the battlefield, are extremely vulnerable to stray and directed laser radiation. The eye is easily attacked by light from a laser source at a considerable distance. Damage caused to optical sensors is extensive and crippling. With the success of many military operations dependent on effective use of optical sensors, the development of sensor protection is imperative.

The laser threat itself is highly agile. The high powered output radiation can occur in a short pulse or continuously, while the wavelength of the output radiation can be either fixed, shifted, or mixed. One example of a threat laser is the short-pulsed neodymium-doped yittrium aluminum garnet or YAG laser. The output wavelength of the laser is in the near infrared at about one micron. However, it can easily be altered via frequency doubling, a process which produces an additional output in the green at about 0.5 microns. The output can be further modified, producing laser radiation at a series of wavelengths scattered over the visible spectrum via the process called Raman scattering. This type of laser threat can, therefore, deliver several laser frequencies simultaneously onto a sensor. It is commonly referred to as a "rainbow" or "white-light" laser. The actual spectrum of the output laser light can be varied and difficult to predict.

While the output of the YAG laser is usually a short pulse, there are also serious laser threats which can provide a continuous output of laser light. The argon-ion and krypton-ion lasers are prime examples. These lasers emit radiation at seven to eight wavelengths simultaneously and can be regarded as continuous wave "rainbow" or "white-light" lasers. While the spectral output of these lasers is fixed, the development

1

of continuously tunable dye lasers and solid state lasers presents a threat with a complex and variable spectral structure.

The ideal protector must provide complete blocking of laser radiation above a predetermined threshold value. It must:

(i)   *be sensitive over a broad spectral range;*

(ii)   *not significantly degrade or attenuate the desired scene to be interrogated;*

(iii)   *operate with a large field-of-view;*

(iv)   *provide protection against continuous and pulsed laser sources;*

(v)   *protect against laser radiation coming from any direction;*

(vi)   *be capable of simultaneously blocking multi-wavelength laser radiation emitted from a single source.*

No such protection device presently exists.

Protection devices or "optical limiters" can be classified as one of two types: active or passive. Active optical limiters require an auxiliary feedback system which is initiated by the incoming laser radiation. A simple example of an active optical limiter is a mechanical shutter which closes when incident laser radiation is detected by an optical diode and a corresponding electrical signal is sent to the shutter. Since lasers with nanosecond rise times are now common, there is very little time for an active protection device to switch. However. electro-optic switches make active switches a realistic possibility. Meanwhile, passive optical limiters rely solely on the incoming laser radiation for switch activation. As a result, the switching time can be minimized and very little, if any, auxiliary equipment is required.

Passive optical limiters can be constructed by using a nonlinear optical material in a specific geometrical configuration. A nonlinear material is one which displays an

2

index of refraction or an absorption which is dependent on the incident laser intensity. The deflection of radiation or the absorption of radiation can thus increase as the incident laser radiation increases. This increase in energy absorbed or deflected produces a decrease in transmission and thereby provides self-generated protection against a laser threat.

The effort described here will concentrate on a dynamic passive device via photorefractive beam fanning. The device operates on the principle of *dynamic gratings*. In the formation of a dynamic grating the incoming laser radiation produces a modulation in the material index of refraction. The index modulation then acts as a *real time* phase grating and deflects, or scatters, the incident laser light as depicted in Figure 1-1.

There are many benefits which can be derived from the development of photorefractive dynamic grating devices. For example, they offer the following desirable features (Figure 1-2):

(i)   *low switching threshold to protect against jamming and spoofing;*

(ii)   *high optical density (OD) to protect against laser-induced damage;*

(iii)   *broad spectral bandwidth to cover in-band agile threats;*

(iv)   *can protect against short plusses well as cw radiation;*

(v)   *direction insensitivity to protect against off-angle radiation;*

(vi)   *allow the outside world to be monitored while it simultaneously rejects laser radiation.*

Lets look at one of these features more closely. A photorefractive limiter has the potential to protect against both short pulse and c.w. threats. This capability is a

3

SIMPLE LIMITER

INPUT LASER
BEAM

LASER LIGHT
THROUGH-PUT

BEAM FAN

4

ATTRACTIVENESS

5
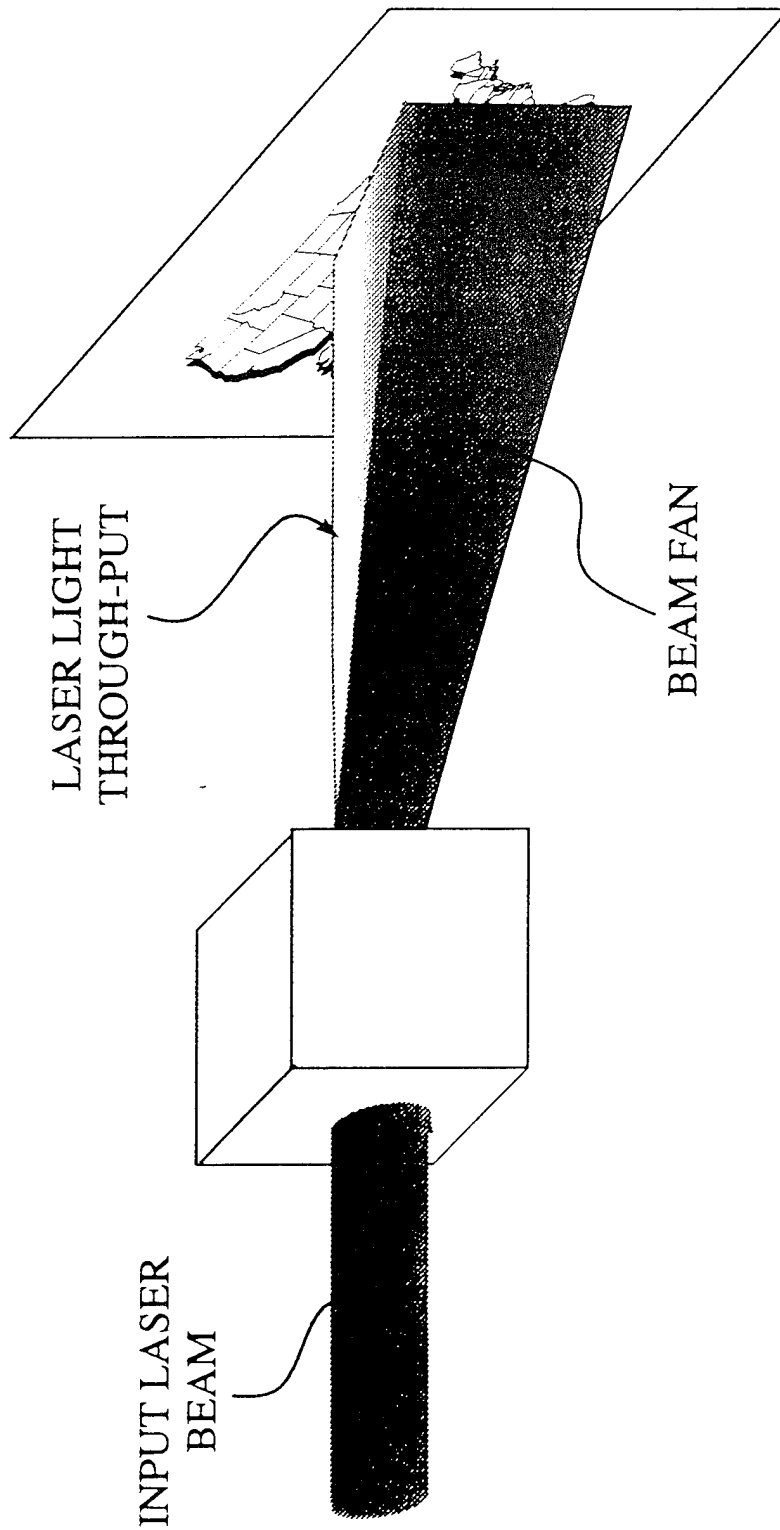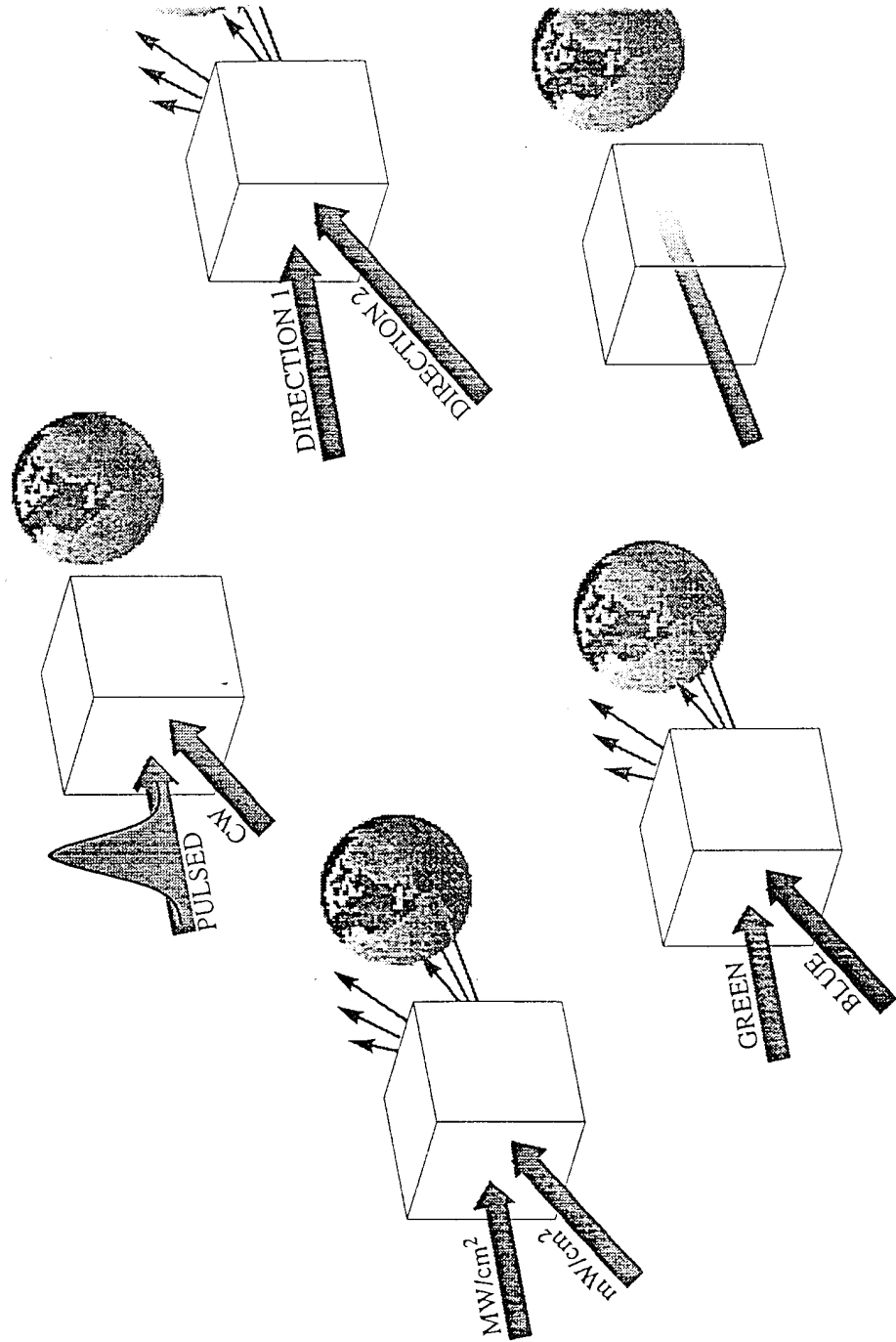
result of the fact that the laser light intensity transmitted through a photorefractive limiter, I_T falls off nearly exponentially in time, i.e.

$$I_T = I_o e^{-t/\tau} \tag{1-1}$$

where the characteristic response time is found to be inversely proportional to the incident intensity, I_o, and given by

$$\tau = \frac{A}{I_o} \tag{1-2}$$

A is a constant.

As a result, the energy per unit area which passes through the crystal is therefore given as

$$\int_0^\infty I_T \, dt = \int_0^\infty I_o e^{-t/\tau} \, dt \tag{1-3}$$

Using (1-2) in (1-3) we find

$$\int_0^\infty I_T dt = \frac{I_o}{\tau} = A. \tag{1-4}$$

Experimental values of the constant "A" are on the order of .1 to .01 Joules per cm^2. It is immediately obvious that if "A" could be reduced by about four to five orders of magnitude, the energy transmitted trough the beam fanning limiter would be clamped in the microjoule range. Amazingly this limiting value would be, therefore, independent of the input temporal width or input intensity. Physically, this attractive feature is due to the fact that if the incident intensity increases the photorefractive limiter response time decreases proportionally, switching off the higher incident intensity more quickly. The faster shutter speed results in the transmitted energy remaining constant at the value "A". Of course, in practice, the transmitted energy does not drop to zero but rather to an equilibrium value I_{eq}. The comparison between I_o and I_{eq} is called the optical density, or O.D., of the limiter. That is,

$$O.D. \equiv \log \frac{I_o}{I_{eq}} \qquad (1\text{-}5)$$

The steady O.D. is determined by the photorefractive index change which depends on the magnitude of the effective electro-optic coefficient of the crystal. Presently available materials, such as $BaTiO_3$ and SBN, have large electro-optic coefficients and consequently display strong photorefractive index changes. When this strong photorefractive index change is maintained by preserving the gain-length product, then significant improvements in the performance of beam fanning limiters can be realized by using a number of different techniques to enhance (speed-up) the decay time of the transmitted beam.

Any technique employed to improve the beam fanning response time, τ_{BF}, must not be accompanied by a loss of gain or the value of the O.D. will suffer. Optical densities in the steady-state should approach 3 or 4. Although the parameter A has not been studied in great detail, however, it is known to be a function of dopants, wavelength, temperature, focusing geometry, length, seeding, applied electric field, and surface quality. A number of techniques have been devised recently for improving the response time of photorefractive materials without sacrificing gain. These include for example, the techniques of increasing the laser intensity, using applied electric fields, seeding the scattering, causing self-focusing and defocusing, controlling the dopant concentration and changing the crystal temperature. To discuss the merit of the results of our investigation of these enhancement techniques we now discuss a model for the photorefraction limiter.

Conclusion

It is clear that our goal is to improve the photorefractive response time by 4 to 5 orders of magnitude while maintaining an O.D. or 3 to 4.

II. PHOTOREFRACTION

The most widely accepted model used to explain the photorefractive effect is the band transport model. This model assumes the existence of mobile charge carriers (which are usually electrons in SBN) residing in traps in the material. When an intensity distribution is incident on the material, the charge carriers in the bright regions of the material are photoexcited from the traps into the conduction band. These excited charges then migrate via drift and diffusion leaving behind ionized traps. The excited charge carriers are continually retrapped and excited again as they migrate until they are eventually retrapped in thr dark regions of the material, where the rate of photoexcitation is greatly reduced. As a result of this migration, a charge distribution forms in the material consisting of the ionized traps in the bright regions and the retrapped charge carriers in the dark regions. This charge distribution generates a space-charge field in the material in accordance with Gauss's law. The space-charge field, in turn, produces a change in the refractive index of the material through the linear electro-optic (Pockel's) effect.

If two plane waves interfere coherently in the material so that the intensity distribution varies periodically, then the resulting index change will be periodic as well. Thus, an index grating is produced in the material. According to Gauss's law, there will be a $\pi/2$ phase shift between the incident intensity distribution and the induced index grating. The $\pi/2$ phase shift will cause the two waves to couple as the propagate through the material and will transfer energy from one wave to the other in the process. In general, this phase shift between the incident intensity distribution and the induced index grating is uniquely responsible for phenomena which make photorefractive materials inviting as an optical limiter.

One of the goals of the mathematical analysis of the band transport model is an expression for the space-charge field in the photorefractive material. A preliminary framework must be established in order to analyze the problem. The positive x-axis
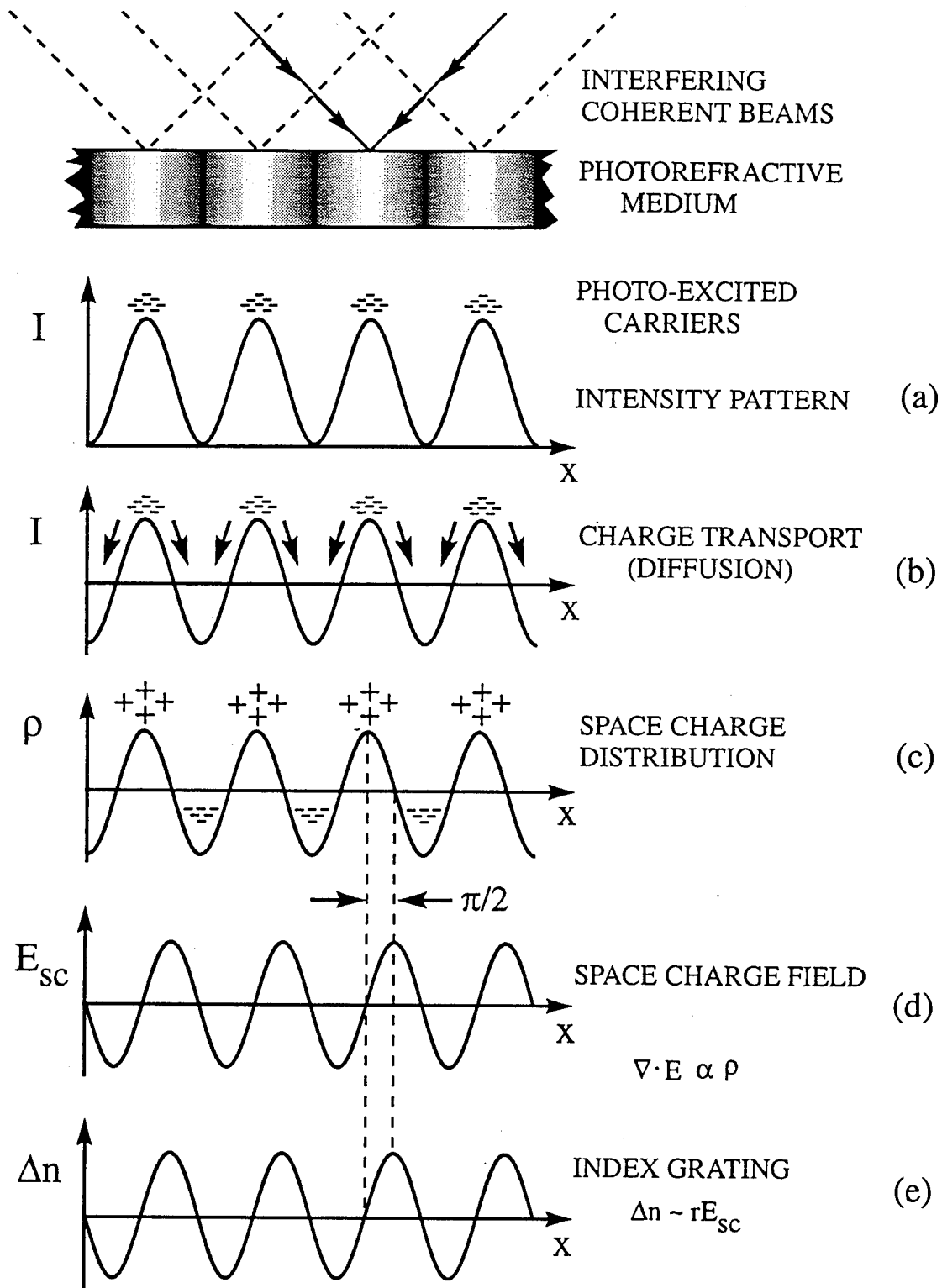
8

INTERFERING
COHERENT BEAMS

PHOTOREFRACTIVE
MEDIUM

PHOTO-EXCITED
CARRIERS

INTENSITY PATTERN   (a)

CHARGE TRANSPORT
(DIFFUSION)   (b)

SPACE CHARGE
DISTRIBUTION   (c)

$\pi/2$

SPACE CHARGE FIELD
(d)

$\nabla \cdot E \; \alpha \; \rho$

INDEX GRATING
$\Delta n \sim rE_{sc}$ (e)

Fig. 3-4 The steps composing the photorefractive effect

9

will be defined by the c-axis of the photorefractive material. Two monochromatic plane waves of the same frequency propagate through the material with wavevectors k_1 and k_2. These plane waves interfere coherently to produce a sinusoidal intensity pattern whose grating wavevector is $k_g = k_1 - k_2$. To simplify the problem, the following constraints are placed on the wavevectors of the plane waves: $K_{y1} = k_{y2} = 0$, $k_{z1}>0$ and $k_{z2}>0$, i.e. the propagate in the xz plane.

Two species of impurity atoms are present in the photorefractive material. The density of acceptor impurities is given by N_A and is assumed constant. The density of donor impurities is given by N_D likewise considered constant. The energy state of the acceptors is assumed to be lower than that of the donors. Thus, each acceptor takes an electron from a donor, producing an ionized donor capable of trapping excited charge carriers. It is assumed that the acceptor impurities N_A are fully occupied at all times, so they do not participate actively in the charge transport mechanism. The density of ionized donors is denoted by $N^+_D(x,t)$, while the density of electrons in the conduction band is given by n_e (x,t). When no light is incident on the material, $n_e(x,t) = 0$ and $\langle N^+_D \rangle = N_A$.
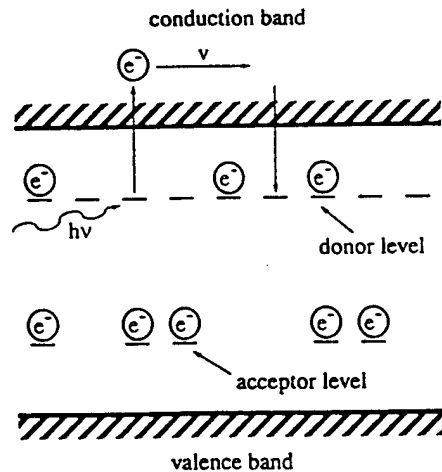
**PHOTOREFRACTIVE
ENERGY LEVEL DIAGRAM**

10

- Rate Equation : the rate of change in the number of ionized donor atoms (neglecting thermal ionization) is the difference in the rate at which the donors are excited and the rate at which ionized donors recapture electrons:

$$\frac{\partial N_D^+}{\partial t} = sI(x)\,(N_D - N_D^+) - \gamma_R n_e N_D^+ \,, \tag{2.1}$$

where s is the photoionization cross-section, $I(x)$ is the incident intensity distribution along the x-axis and γ_R is the recombination coefficient of a free electron at the site of an ionized donor.

- Current Density : the (conventional) current density, $j_x(x, t)$, is composed of drift and diffusion terms:

$$j_x = q_e \mu_e n_e E_x + \mu_e k_B T \frac{\partial n_e}{\partial x} \,, \tag{2.2}$$

where q_e is the magnitude of electron charge, μ_e is the electron mobility, $E_x(x, t)$ is the total electric field (internal and external), k_B is Boltzmann's constant and T is the temperature (in Kelvin).

- Continuity Equation : any spatial variation of the current density must be accompanied by the accumulation or depletion of charge carriers in the region of variation:

$$\frac{\partial j_x}{\partial x} = -q_e \frac{\partial}{\partial t}(N_D^+ - n_e) \,. \tag{2.3}$$

- Gauss's Law : the spatial variation of the electric field is dependent upon the charge distribution in the material:

$$\frac{\partial E_x}{\partial x} = \frac{q_e}{\varepsilon}\,(N_D^+ - n_e - N_A) \,, \tag{2.4}$$

where ε is the static permittivity of the material.

11

Solution for the Space-Charge Field

The equations in the preceding section form a highly nonlinear system which, in general, cannot be solved analytically. However, a closed form solution can be obtained with some assumptions. The interference of two monochromatic plane waves results in an intensity distribution which is modulated sinusoidally. Hence, if $I(x)$ is expressed as a Fourier series and it is assumed that all but the zeroth- and first-order terms are negligible, then the intensity distribution can be written as follows:

$$I(x) = I_0 + \frac{1}{2} [I_1 e^{ik_g x} + \text{c.c.}] = I_0 + \frac{m}{2} [I_0 e^{ik_g x} + \text{c.c.}] , \qquad (2.5.\text{a})$$

where $m = I_1/I_0$ is the modulation ratio. The other variables then assume similar forms:

$$n_e(x, t) = n_{e0}(t) + \frac{1}{2} [n_{e1}(t) e^{ik_g x} + \text{c.c.}] , \qquad (2.5.\text{b})$$

$$N_D^+(x, t) = N_0^+(t) + \frac{1}{2} [N_1^+(t) e^{ik_g x} + \text{c.c.}] , \qquad (2.5.\text{c})$$

$$j_x(x, t) = j_0(t) + \frac{1}{2} [j_1(t) e^{ik_g x} + \text{c.c.}] , \qquad (2.5.\text{d})$$

$$E_x(x, t) = E_0(t) + \frac{1}{2} [E_1(t) e^{ik_g x} + \text{c.c.}] , \qquad (2.5.\text{e})$$

where E_0 is any applied external field and E_1 is the space-charge field in the photorefractive material. Substituting these equations into (2.1)-(2.4), the following set of linearized equations is obtained:

$$\frac{dN_0^+}{dt} = sI_0(N_D - N_0^+) - \gamma_R n_{e0} N_0^+ , \qquad (2.6.\text{a})$$

$$\frac{dN_1^+}{dt} = smI_0(N_D - N_0^+) - sI_0 N_1^+ - \gamma_R(n_{e0} N_1^+ + n_{e1} N_0^+) , \qquad (2.6.\text{b})$$

12

$$j_0 = q_e \mu_e n_{e0} E_0 \ , \tag{2.6.c}$$

$$j_1 = q_e \mu_e (n_{e0} E_1 + n_{e1} E_0) + i \mu_e k_B T k_g n_{e1} \ , \tag{2.6.d}$$

$$0 = \frac{dN_0^+}{dt} - \frac{dn_{e0}}{dt} \ , \tag{2.6.e}$$

$$ik_g j_1 = -q_e \left(\frac{dN_1^+}{dt} - \frac{dn_{e1}}{dt} \right) , \tag{2.6.f}$$

$$0 = N_0^+ - n_{e0} - N_A \ , \tag{2.6.g}$$

$$ik_g E_1 = \frac{q_e}{\varepsilon} (N_1^+ - n_{e1}) \ . \tag{2.6.h}$$

With these, one can obtain the following second-order differential equation for E_1:

$$\frac{d^2 E_1}{dt^2} + (\frac{1}{\tau_+} + \frac{1}{\tau_{di}} + \frac{1}{\tau_D} - \frac{i}{\tau_E}) \frac{dE_1}{dt} + (\frac{1}{\tau_+ \tau_{di}} + \frac{1}{\tau_I \tau_D} - \frac{i}{\tau_I \tau_E}) E_1 = \frac{q_e}{ik_g \varepsilon} (\frac{1}{\tau_D} - \frac{i}{\tau_E}) sm I_0 (N_D - n_{e0} - N_A) \ , \tag{2.7}$$

where the time constants in (2.7) are

$$\tau_D \equiv \text{mean diffusion time} \ = \ \frac{q_e}{\mu_e k_B T k_g^2} \ , \tag{2.8.a}$$

$$\tau_E \equiv \text{mean drift time} \ = \ \frac{1}{\mu_e k_g E_0} \ , \tag{2.8.b}$$

$$\tau_{di} \equiv \text{dielectric relaxation time} \ = \ \frac{\varepsilon}{q_e \mu_e n_{e0}} \ , \tag{2.8.c}$$

$$\tau_I \equiv \text{excitation time} \ = \ \frac{1}{s I_0 + \gamma_R n_{e0}} \ , \tag{2.8.d}$$

$$\tau_+ \equiv \frac{1}{sI_0 + 2\gamma_R n_{e0} + \gamma_R N_A} \quad . \tag{2.8.e}$$

For low irradiances, i.e. few photoexcited carriers ($N_A \gg n_{e0}$) and fast trapping ($\gamma_R N_A \gg sI_0$), τ_+ reduces to τ_R, the recombination time:

$$\tau_+ \approx \frac{1}{\gamma_R N_A} \equiv \tau_R \quad . \tag{2.9}$$

A detailed derivation of (2.7) is given in Appendix I, as well as derivations of the steady-state and time-dependent forms of the space-charge field in the photorefractive material.

Steady-State Solution

The steady-state solution for the space-charge field is easy to obtain since the time derivatives in (2.7) vanish. For low irradiances, the equilibrium space-charge field is given by

$$E_1^{ss} = mE_{sc}e^{i\phi} , \tag{2.10}$$

where the amplitude, E_{sc}, and the phase shift, ϕ, are

$$E_{sc} = E_N \sqrt{\frac{E_D^2 + E_0^2}{(E_D + E_N)^2 + E_0^2}} , \tag{2.11.a}$$

$$\tan\phi = \frac{E_D}{E_0}\left(1 + \frac{E_D}{E_N} + \frac{E_0^2}{E_D E_N}\right) , \tag{2.11.b}$$

and E_D and E_N are defined as

$$E_D = \frac{k_B T k_g}{q_e} , \tag{2.12.a}$$

$$E_N = \frac{q_e N_{eff}}{k_g \varepsilon} = \frac{q_e N_A}{k_g \varepsilon}\left(1 + \frac{N_A}{N_D - N_A}\right)^{-1} \quad . \tag{2.12.b}$$

14

The electric field E_D is the effective field causing electron diffusion while the electric field E_N is the maximum space-charge field attainable without applying an external field. The total electric field at equilibrium is then

$$E_x^{ss}(x) = E_0 + \frac{m}{2} E_{sc} [e^{i(k_g x + \phi)} + \text{c.c.}] \ . \tag{2.13}$$

Time-Dependent Solution

Due to the form of (2.7), some damped, oscillatory behavior in the space-charge field would be expected as it evolves from its initial value to its equilibrium value. If no gratings exist in the photorefractive material at time $t = 0$ and if we assume that $\tau_+ \ll \tau_{di}$, $\tau_+ \ll \tau_D$ and $\tau_+ \ll \tau_I$, then the time-dependent form of the space-charge field is given by

$$E_1(t) = E_1^{ss} [1 - e^{-t/\tau} e^{i\omega t}] \ , \tag{2.14}$$

where τ and ω are

$$\tau = \tau_{di} \cdot \frac{\left(1 + \frac{\tau_+}{\tau_D} + \frac{\tau_+}{\tau_{di}}\right)^2 + \left(\frac{\tau_+}{\tau_E}\right)^2}{\left(1 + \frac{\tau_+ \tau_{di}}{\tau_I \tau_D}\right)\left(1 + \frac{\tau_+}{\tau_D} + \frac{\tau_+}{\tau_{di}}\right) + \frac{\tau_{di}}{\tau_I}\left(\frac{\tau_+}{\tau_E}\right)^2} \ , \tag{2.15.a}$$

$$\omega = \frac{1}{\tau_{di}} \cdot \frac{\left(\frac{\tau_+}{\tau_E}\right)\left(\frac{\tau_{di}}{\tau_I} - 1\right)}{\left(1 + \frac{\tau_+}{\tau_D} + \frac{\tau_+}{\tau_{di}}\right)^2 + \left(\frac{\tau_+}{\tau_E}\right)^2} \ . \tag{2.15.b}$$

The time-dependent form of the total electric field is then

$$E_x(x, t) = E_0 + \frac{m}{2} E_{sc} [e^{i(k_g x + \phi)} [1 - e^{-t/\tau} e^{i\omega t}] + \text{c.c.}] \ . \tag{2.16}$$

15

Pockel's Effect and Grating Formation

The space-charge field produced by charge separation in the photorefractive crystal induces a change in the refractive index of the crystal via Pockel's effect. Given an electric field in the material, the change in the impermeability tensor is given by

$$\Delta \eta_{ij} = r_{ijk} E_k ,$$
(2.17)

where r_{ijk} is the linear electro-optic tensor. This results in an index change given by

$$\Delta n = -\frac{1}{2} n_0^3 r_{eff} E ,$$
(2.18)

where n_0 is the unperturbed refractive index of the medium and r_{eff} is a linear combination of elements of r_{ijk} that depends on both orientation of the crystal and direction of the electric field (see Appendix II). By substituting (2.13) into (2.18), we obtain the following expression for the equilibrium change in the refractive index due to the electric field in the material:

$$\Delta n = -\frac{1}{2} n_0^3 r_{eff} E_0 - \frac{m}{4} n_0^3 r_{eff} E_{sc} \left[e^{i(k_g x + \phi)} + \text{c.c.} \right] .$$
(2.19)

The spatial variation of the refractive index in the material can be expressed as

$$n(x) = n_1 + \frac{1}{2} \left[n_2 e^{ik_g x} + \text{c.c.} \right] .$$
(2.20)

By comparing (2.19) and (2.20), n_1 and n_2 must be given by the following:

$$n_1 = n_0 - \frac{1}{2} n_0^3 r_{eff} E_0 ,$$
(2.21.a)

$$n_2 = -\frac{m}{2} n_0^3 r_{eff} E_{sc} e^{i\phi} .$$
(2.21.b)

16

Assuming r_{eff} is positive, (2.21.b) shows that the modulation of the refractive index is in phase with the space-charge field and, thus, shifted by the phase angle Φ with respect to the incident intensity distribution.

Summary

Having coumpleted a description of the basic underlying physics for the photorefractive limiter we can now turn our attention to a discussion of the most significant results of our efforts to enhance the photorefractive response time without a reduction in the O.D.

III. INCREASING THE INTENSITY

The photorefractive response time is given in expression (2.15.a). For our materials, $\tau_+ \sim \tau_R \ll \tau_D, \tau_{di}, \tau_I$. a result, for zero applied field (2.15.a) becomes

$$\tau = \tau_{di} \qquad (3\text{-}1)$$

Since τ_{di} is inversely proportional to n_{eo} which is itself proportional to the incident total intensity I_0, τ_{di} is inversely proportional to I_0, i.e.

$$\tau = \frac{A}{I_0} \qquad (3\text{-}2)$$

Physically, this is the case because a higher intensity means more charges in the conduction band and therefore an increased diffusion rate and a faster approach to equilibrium.

Given that the photorefractive response time can increase due to a higher intensity it is easy to see that one approach to achieving our goal of a faster response time would be to focus the incident laser power to a small spot size. In this way, for a given incident power the photorefractive response time will shorten dramatically. This approach, however, is not straight forward.

The beam fan originates from conventional scattered light which crosses the incident beam and writes index gratings in the crystal via the photorefractive effect. As a result of these index gratings, energy is coupled from the incident beam into the weaker scattered beams, which can result in significant depletion of the incident beam. The magnitude of the coupling depends on the number of scatterers, the gain of the crystal, and the available length ((interaction length) over which the incident beam and the scattered beam the interaction length can typically be several millimeters long (i.e., of the order of a few beam waists). This interaction length does not change as the intensity is increased by turning up the laser power and an intensity dependence of approximately I^{-1} is typically observed for the beam fanning time response. However, for a beam focused with a spherical lens the interaction length may be of the order 50
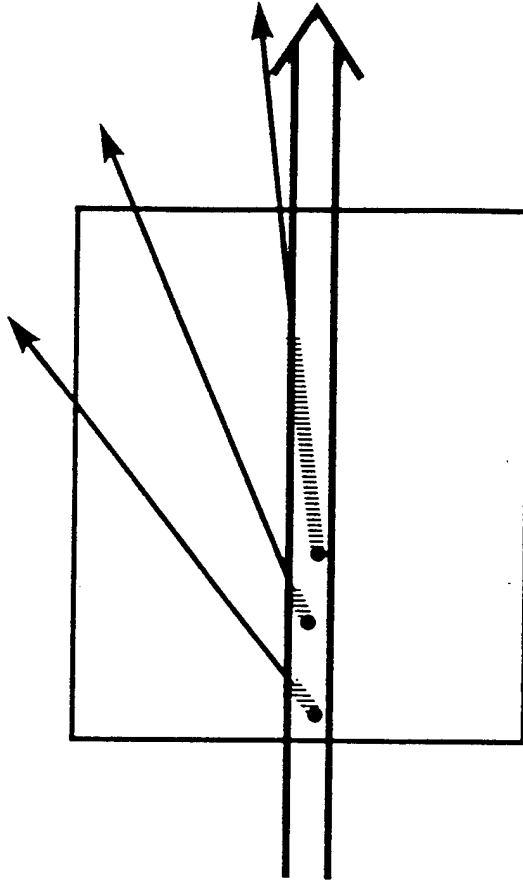
18

DECREASING THE RESPONSE TIME

1 W/cm^2

1 W/cm^2

1 W/cm^2

1 MW/cm^2

19
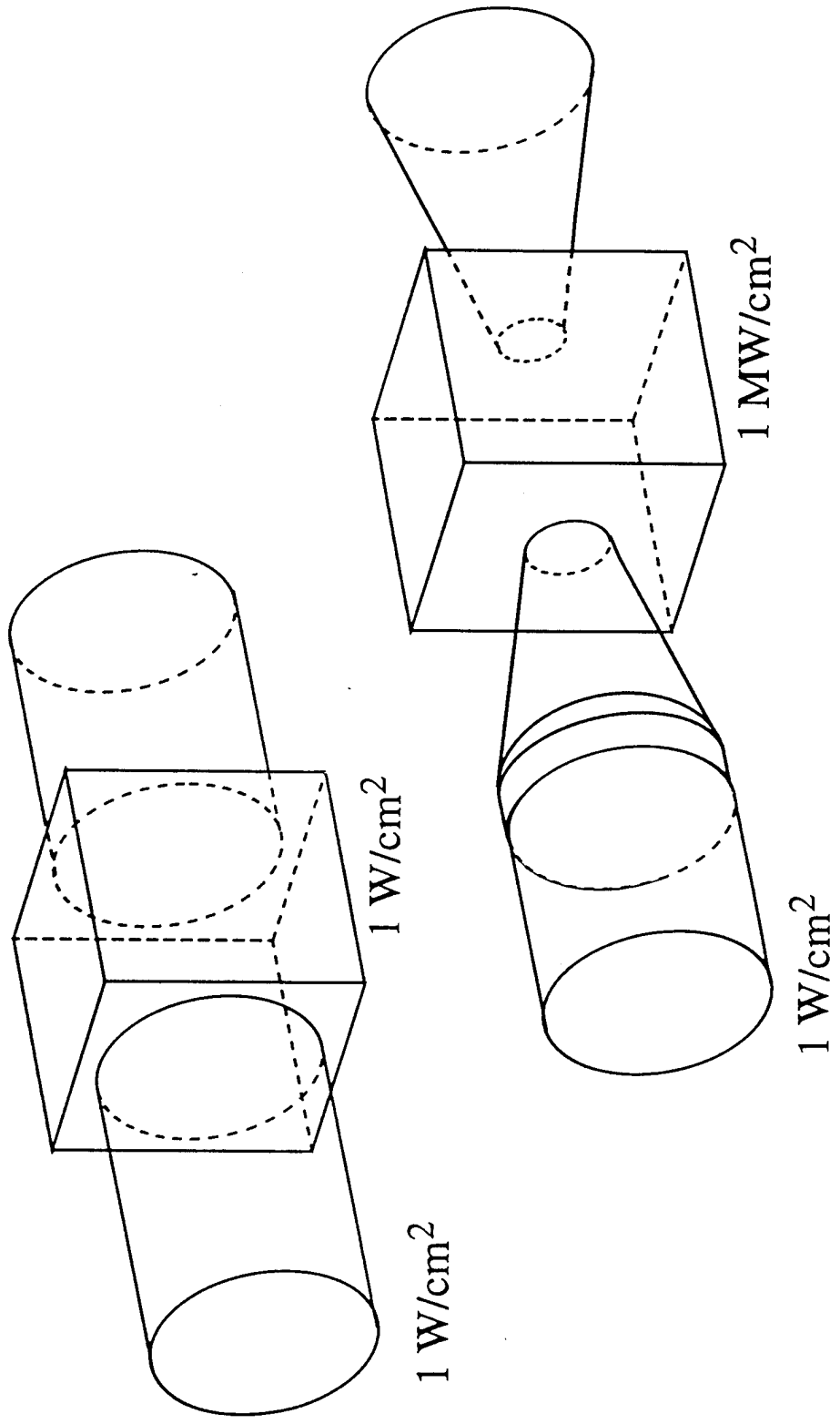
INTERACTION LENGTH
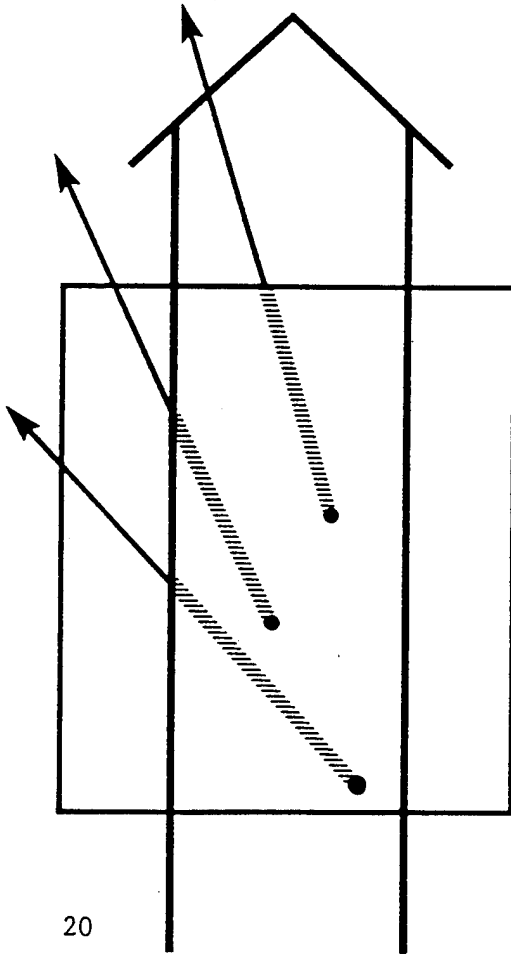
UNFOCUSSED
Interaction length or
γL mostly large

FOCUSSED
Interaction length or
γL mostly small

20

μm or less. Beam fanning is almost absent for such small interaction lengths even though the time response still exhibits an I^{-1} intensity dependence.

The situation is different with a cylindrical lens which can produce faster response times without a reduction in coupling strength. This is because a cylindrical lens focuses in one dimension. It can, therefore, produce a tight focus in the dimension which has a small gain and still maintain a large interaction length in the other dimension. For example, in SBN the relevant EO coefficients are $r_{33} = 2224 \times 10^{-12}$m/V and $r_{13} = 55 \times 10^{-12}$m/V, where r_{33} provides the maximum gain for extraordinary polarized beams propagating at near normal incidence to the c-axis (the grating wave vector parallel with the c-axis). As a result, the greatest beam depletion is achieved by combining the large gain associated with r_{33} and the large interaction length associated with the major axis of the elliptical beam spot produced by the cylindrical lens. The gain coefficient in the other direction is dominated by r_{13} and is small by comparison, so little is lost by having a tight focus in this direction. In the cylindrical focusing geometry the intensity is increased although not as much as the spherical lens case (i.e., πr_0^2 vs $\pi r_0 r$). However, the increase in intensity decreases the response time at no cost to beam depletion.

A comparison of the beam fanning response is shown in Fig. 3.1. In this figure the c-axis of the crystal is into the plane of the page and the beams are focused in the crystal. In these conditions there is virtually no beam fanning produced when focusing to a spot size of 0.1mm (FW1/e^{2}M) with a spherical lens. This comparison is somewhat striking since the unfocused spot size was 2.12mm, and the cylindrical lens focused the beam to an elliptical spot with axes of 0.11 x 2.12mm.

The response times vs power for unfocused and cylindrical focusing are compared in Fig. 3.2 for the same spot sizes used in the measurements of Fig. 3.1. The observed shortening of the response time (factor of 20) by the cylindrical lens compares well with the ratio of the areas of the focused and unfocused beams. In other

21

words, the improvement in the time response obtained for the cylindrical lens is just due to the increase in intensity achieved by reducing the spot size. The parameters A and b, given in the caption, were obtained from a least-squares fit to the data and agree well with previous measurements of the beam fanning response time where approximate I^{-1} intensity dependence was found for Ce doped SBN crystals. The present measurements indicate that the I^{-1} intensity dependence of the time response is valid over at least 3 orders of intensity variation.

Conclusion

We have demonstrated that the use of a cylindrical lens to focus the incident laser power down to a small spot size can reduce the response time while maintaining an O.D. of 2 to 3. This means that an incident beam of 5cm x 5cm can be focused using a cylindrical lens 50 microns x 5cm or a reduction in size, in one dimension, of 10^{-3}. This results in an intensity increase of 10^3 and a corresponding decrease in response time of 3 orders of magnitude. Since this is close to our 4 to 5 orders of magnitude goal, it is clear that this technique is significant when coupled with others may produce a viable photorefractive limiter.

C

TIGHT FOCUS

INTERACTION
LENGTH

23
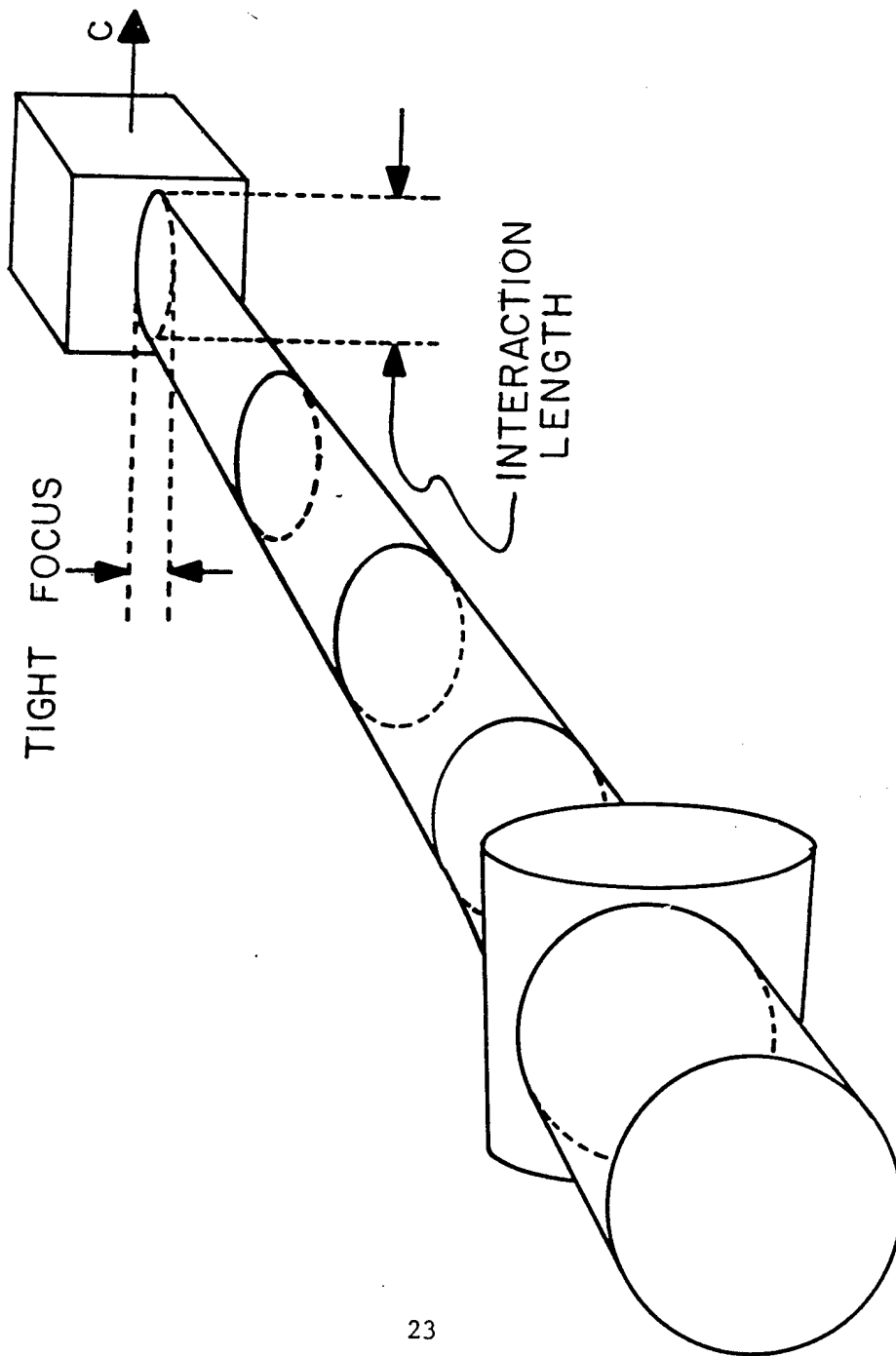
BEAM FANNING AT THE FOCAL POINT
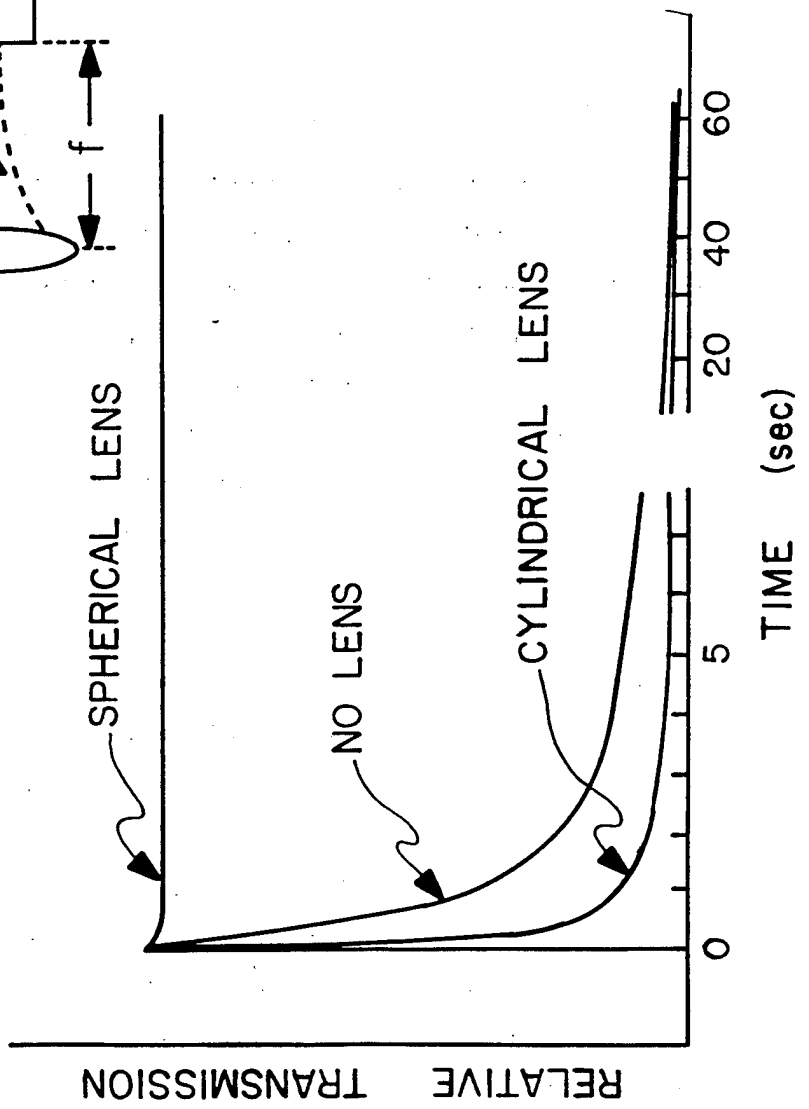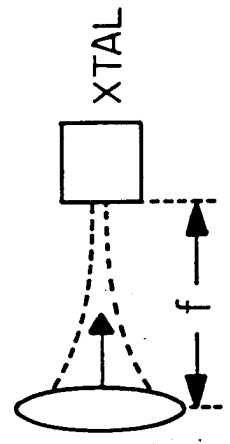
BEAM FANNING RESPONSE TIME
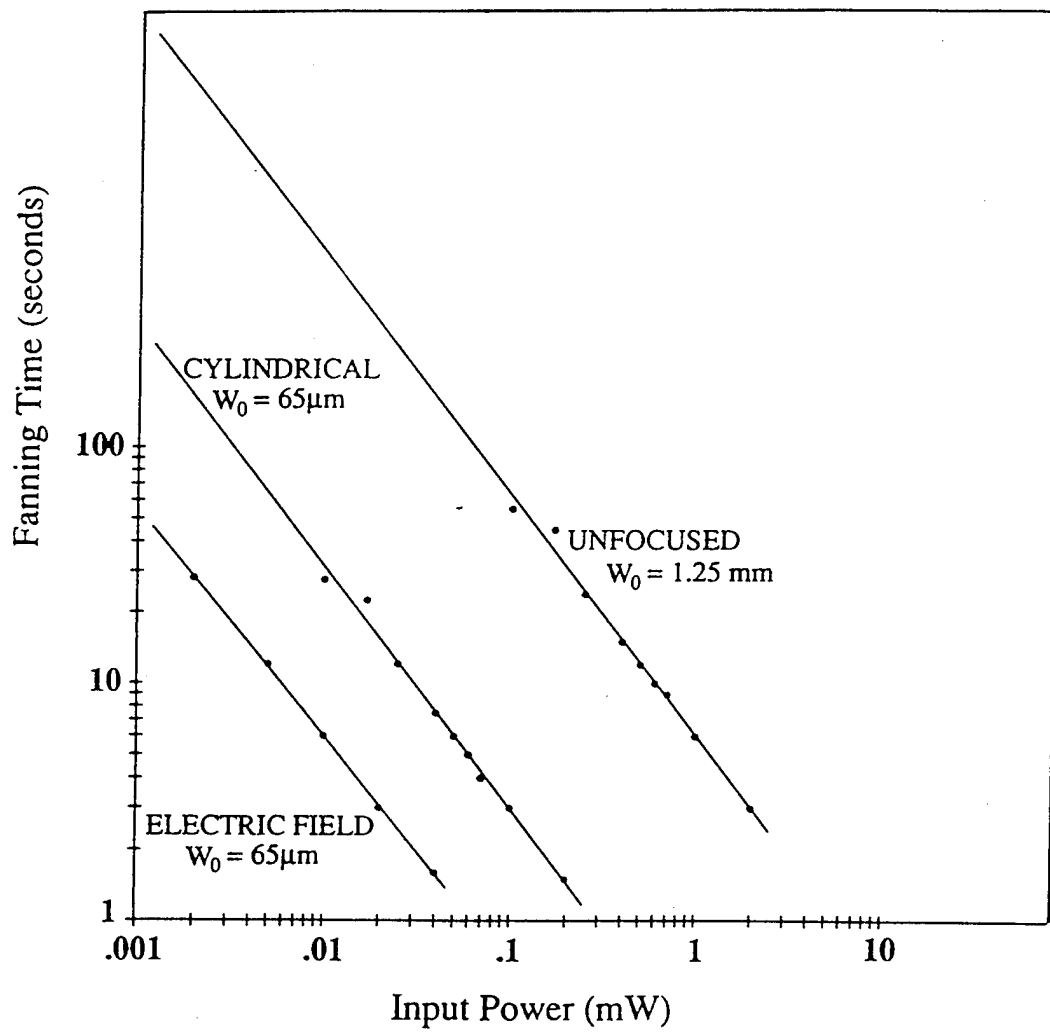
IV. APPLIED DC ELECTRIC FIELD

As can be seen from expressions (2.11.a) and (2.15.a), both the magnitude of the space charge electric field and its time of formation response time can be enhanced with the application of a d.c. electric field.

The dependence of the space charge field and its formation time on the applied field can be seen from

$$E_x(x,t) = E_O + \frac{m}{2} E_{sc} \left[e^{i(Kgx+\phi)} \left[1 - e^{-t/\tau} e^{i\omega t} + c.c \right] \right] \qquad (4\text{-}1)$$

where

$$m = 2(I_1 I_2)^{1/2} / (I_1 + I_2) \qquad (4\text{-}2)$$

= fringe visibility

$$E_{sc} = E_q \frac{E_D^2 + E_O^2}{\left(E_D + E_q\right)^2 + E_O^2} \rightarrow E_q \qquad (4\text{-}3)$$

approaching E_q or E_N large applied fields and

$$\tan \phi = -\frac{E_D}{E_O} \left[1 + \frac{E_D}{E_q} + \frac{E_O^2}{E_D E_q} \right] \rightarrow -\infty \qquad (4\text{-}4)$$

approaching $\Phi = -90°$ for large applied fields

and $\qquad \tau \rightarrow \tau_I \qquad\qquad\qquad\qquad (4\text{-}5)$

approaching τ_I for large applied fields

26

$$\text{and} \qquad \omega = \frac{1}{\tau_{di}} \frac{\dfrac{\tau_R}{\tau_E}\left(\dfrac{\tau_{di}}{\tau_I} - 1\right)}{\left(1 + \dfrac{\tau_R}{\tau_D} + \dfrac{\tau_R}{\tau_{di}}\right)^2 + \left[\dfrac{\tau_R}{\tau_E}\right]^2} \rightarrow \frac{\tau_R}{\tau_E}\frac{1}{\tau_I} \qquad (4\text{-}6)$$

approaching a number which make possible to observation of oscillations.

Physically, E_q or E_N is the electric field that would exist if all available charge carrier bright to the dark regions of an interference pattern. Meanwhile, τ_I is the time to excite all the charges will be transported. In addition, the period of oscillation T is now the ratio of τ_E to τ_R times the response time τ_I. In other words it is related to the number of grating periods the carriers travel before re-trapped.

While these limiting values provide a sense of the potential of using an applied electric field, numerical solutions can be used to focus more at finding optimum crystal parameters.

The numerical method used in our computer program and the physical parameters are listed in Appendix IV and V. The computer program was run for different trap number densities of the crystal. For each value of N_A the total space-charge field was calculated for both the no field case and the DC field case. The calculated results for the space-charge field time evolution are shown in Fig. 4-1 through Fig. 4-6.

no field $N_A = 5 \cdot 10^{16}$ cm^{-3} $N_D = 5 \cdot 10^{17}$ cm^{-3}

$k_g = 2.4 \cdot 10^4$ 1/cm   I = 100 mw/cm^2

E_{sc}^* $(\tau \cong 2.3$ s $)$

(Relative Units)

5000

4000

3000

2000
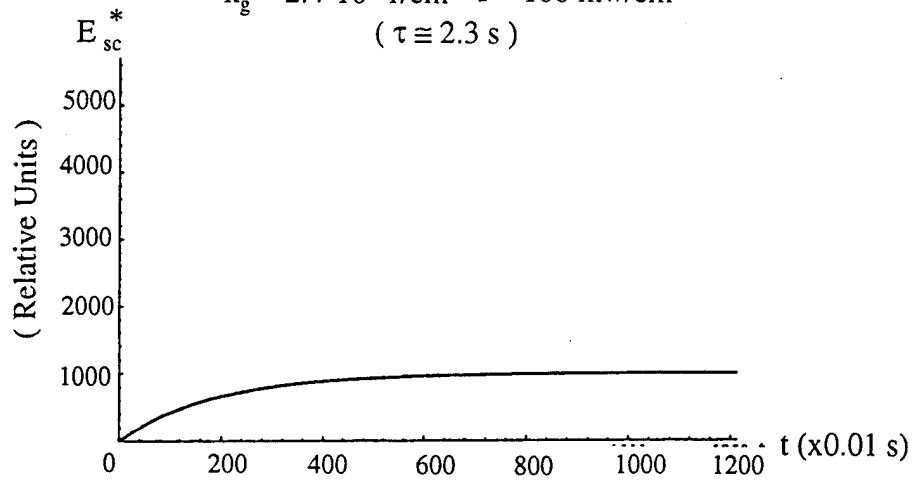
1000

0   200   400   600   800   1000   1200   t (x0.01 s)

Fig. 4-1

* E_{sc} is the total space-charge field

DC field: 4 kv/cm $N_A = 5 \cdot 10^{16}$ cm^{-3} $N_D = 5 \cdot 10^{17}$ cm^{-3}

$k_g = 2.4 \cdot 10^4$ 1/cm   I = 100 mw/cm^2

E_{sc} $(\tau \cong 1.6$ s $)$

(Relative Units)

5000

4000

3000

2000

1000

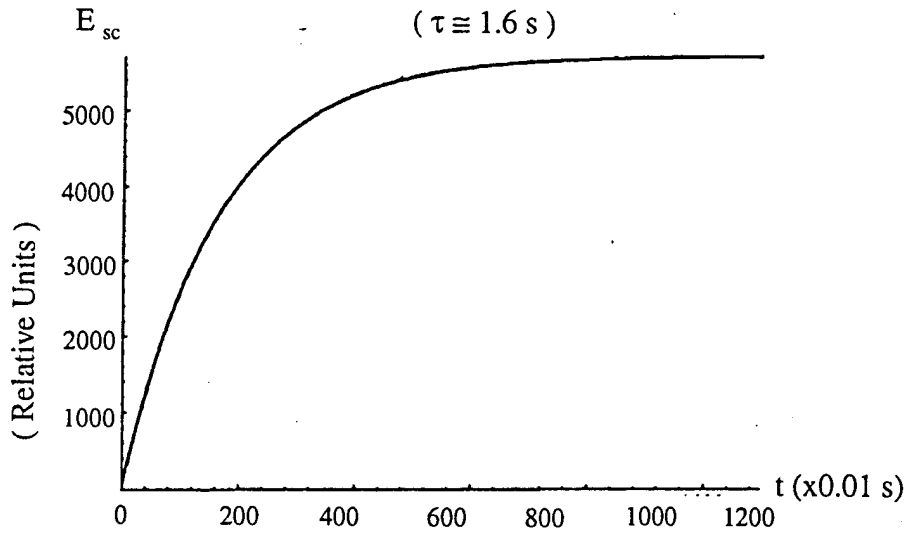0   200   400   600   800   1000   1200   t (x0.01 s)

Fig. 4-2

no field $N_A = 1.5 \cdot 10^{16}\,\text{cm}^{-3}$ $N_D = 5 \cdot 10^{17}\,\text{cm}^{-3}$

$k_g = 2.4 \cdot 10^4\ 1/\text{cm}$ $I = 100\ \text{mw/cm}^2$

E_{sc}

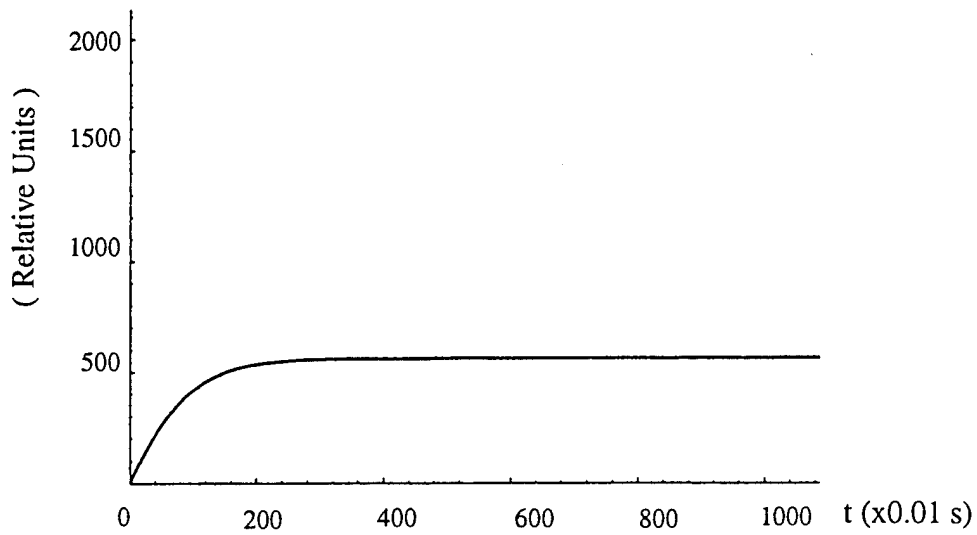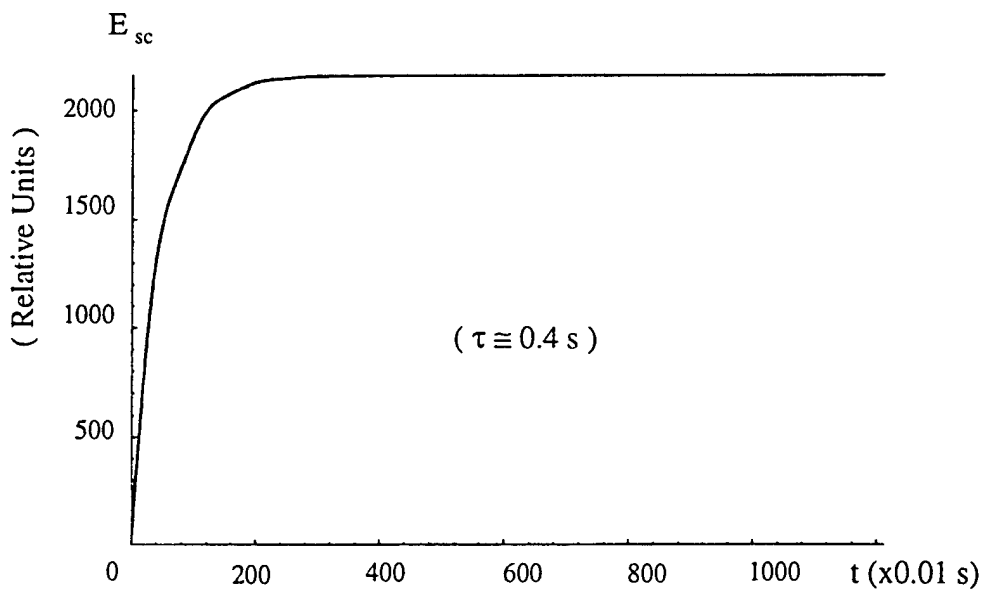$(\ \tau \cong 0.8\ \text{s}\ )$

Fig. 4-3

DC field: 4 kv/cm $N_A = 1.5 \cdot 10^{16}\,\text{cm}^{-3}$ $N_D = 5 \cdot 10^{17}\,\text{cm}^{-3}$

$k_g = 2.4 \cdot 10^4\ 1/\text{cm}$ $I = 100\ \text{mw/cm}^2$

E_{sc}

$(\ \tau \cong 0.4\ \text{s}\ )$

Fig. 4-4

29

no field $N_A = 5 \cdot 10^{15}$ cm^{-3} $N_D = 5 \cdot 10^{17}$ cm^{-3}

$k_g = 2.4 \cdot 10^4$ 1/cm $I = 100$ mw/cm^2

E_{sc} $(\tau \cong 1.2$ s $)$

Fig. 4-5

DC field: 4kv/cm $N_A = 5 \cdot 10^{15}$ cm^{-3} $N_D = 5 \cdot 10^{17}$ cm^{-3}

E_{sc} $k_g = 2.4 \cdot 10^4$ 1/cm $I = 100$ mw/cm^2

$(\tau \cong 0.6$ s $*)$

Fig. 4-6

*Note: The response time τ is measured from a curve drawn by connecting the bottom points on this curve.

30

These curves show that due to a DC field (1) the magnitude of the space-charge field was increased; (2) the photorefractive response time was reduced; and (3) an oscillation of the space-charge field appeared (see Fig.4-6).

For the curves Fig.4-1 through Fig.4-6 all the parameters are the same except N_A, the trap number density in the crystal. The N_A values picked in different curves are $5 \cdot 10^{16}$ cm^{-3} in Fig.4-1 and 4-2, $1.5 \cdot 10^{16}$ cm^{-3} in Fig.4-3 and 4-4, and $5 \cdot 10^{15}$ cm^{-3} in Fig.4-5 and 4-6. By analyzing and comparing these curves we found that for crystals with different N_A values, the enhancement of the photorefractive effect was different even with the same DC field. Looking at Fig.4-1 and Fig.4-2, it is seen that for a large N_A value the applied DC field doesn't change the photorefractive response time substantially. However, by reducing the N_A value from $5 \cdot 10^{16}$ cm^{-3} to $1.5 \cdot 10^{16}$ cm^{-3}, the results shown in Fig.4-3 and Fig.4-4 are exciting. We see that with the same DC field as used in the above case a larger enhancement is observed in both the magnitude and the speed of the photorefractive effect. The response time is reduced by about one half with a DC field of 4 kv/cm to a crystal. In Fig.4-5 and Fig.4-6 the N_A value was decreased further to $5 \cdot 10^{15}$ cm^{-3}. We see that the response time is also reduced to about one half with a DC field of 4 kv/cm, but the actual response time in this case is longer than that in the case of $N_A = 1.5 \cdot 10^{16}$ cm^{-3}. Moreover, an oscillation with time in the space-charge field is observed. From eq.(4-6) we can get a dependence of ω on N_A and N_D, which is

$$\omega \propto (N_D^2 - N_A^2)/[c_1(N_A^2 + c_2) + c_3] \qquad\qquad (4\text{-}7)$$

where c_1, c_2 and c_3 are constants independent of N_A and N_D. From (4-7) we can see that a smaller N_A will cause a bigger ω. Physically, a smaller N_A makes a longer recombination time τ_R, which results in that the electrons in conduction band can move freely across one or more grating space periods without being recombined. That's why Fig.4-6 showed an oscillation.

Therefore, the conclusion is that if the N_D value is fixed an appropriate N_A value of a crystal is vital to observe an enhancement of the photorefractive response time with an applied field. This important result can be explained physically. The recombination time τ_R is inversely proportional to the crystal trap number density. With N_A decreasing τ_R is increasing. As τ_R is increased to be longer than the field drift time τ_E, electrons in the conduction band can move further without being recombined. A longer recombination time makes it possible for the space-charge field to be built up in a shorter time. This is why the photorefractive response time is getting shorter for the same magnitude of an applied field as the crystal has a smaller N_A value. However, if N_A is too small, or in other words, the recombination time τ_R is too long, electrons in conduction band can move freely across several grating space periods without recombination. This will result in an oscillation of the space-charge field, and it will take longer time to have the space-charge field reach an equilibrium. So it seems that there is a compromise for a trap number density of the crystal between a big number and a small number. The value of N_A should be chosen such that by applying an external electric field across a crystal the resulted space-charge field will be able to

reach an equilibrium faster but without causing oscillations. We also ran the computer

program for the space-charge field by keeping N_A constant while changing the N_D

value and k_g value, respectively. The parameters and results are as follows:

1.　Varying N_D value

DC field:　4 kv/cm　　$N_A = 1.5 \cdot 10^{16} cm^{-3}$　$N_D = 5 \cdot 10^{17} cm^{-3}$

$k_g = 2.4 \cdot 10^4$ 1/cm　$I = 100$ mw/cm^2

$(\tau \cong 0.4 \, s)$
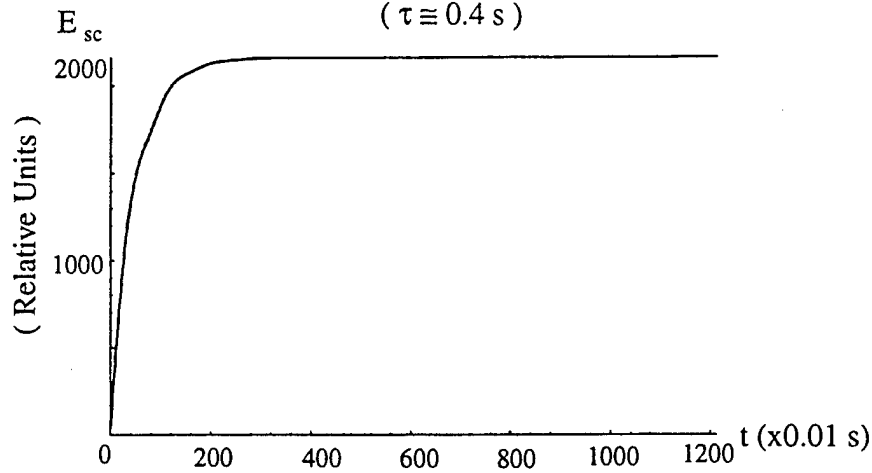
Fig. 4-7

DC field:　4 kv/cm　　$N_A = 1.5 \cdot 10^{16} cm^{-3}$　$N_D = 1.5 \cdot 10^{17} cm^{-3}$

(smaller N_D)　　　$k_g = 2.4 \cdot 10^4$ 1/cm　$I = 100$ mw/cm^2

$(\tau \cong 3.6 \, s)$
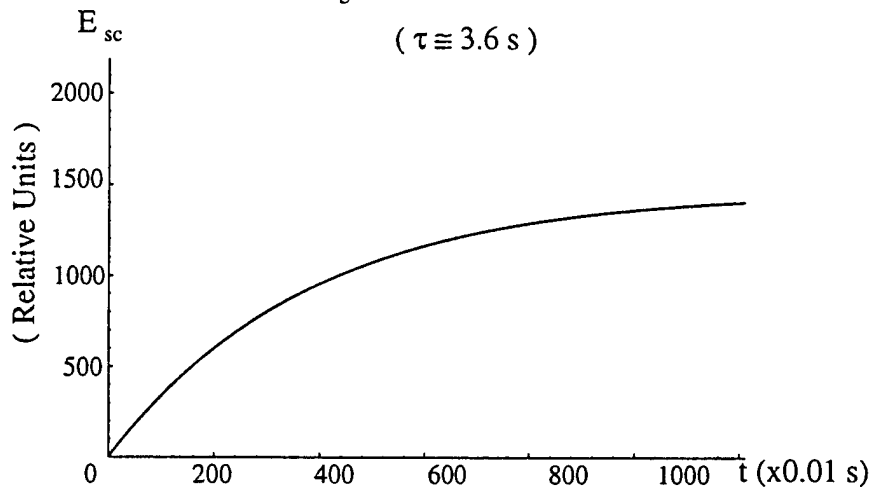
Fig. 4-8

DC field: 4 kv/cm $N_A = 1.5 \cdot 10^{16} cm^{-3}$ $N_D = 1.5 \cdot 10^{18} cm^{-3}$

(bigger N_D) $k_g = 2.4 \cdot 10^4$ 1/cm $I = 100$ mw/cm^2

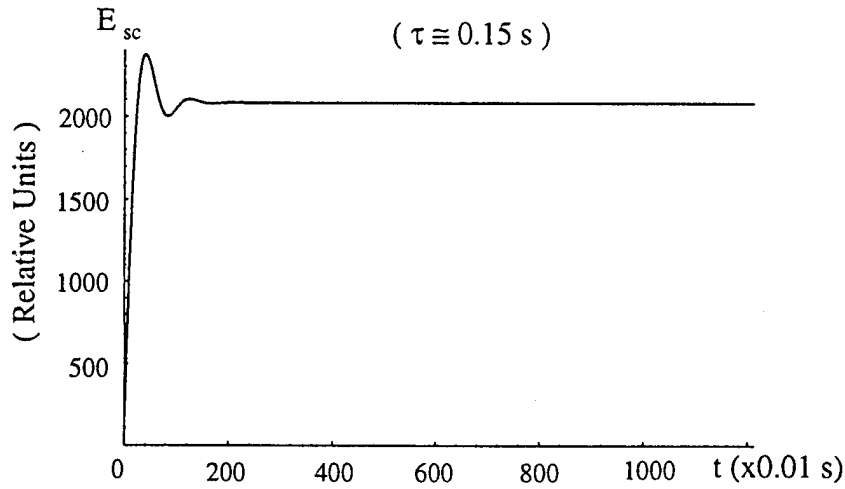E_{sc} $(\tau \cong 0.15 s)$

Fig. 4-9

The curves showed that (1) a smaller N_D made a longer response time; (2) a

larger N_D caused an oscillation of the space-charge field. Mathematically, from

expression (4-7) we see that a bigger N_D causes a bigger ω. Physically, with

same optical intensity, if N_D is bigger, more electrons will be excited to the

conduction band than the case with smaller N_D. This will make more electrons in

conduction band moving freely across one or more grating space periods.

Therefore, an oscillatory space-charge field is produced.

2.   Varying k_g value

In Fig.4-7, $N_A = 1.5 \cdot 10^{16}$ cm^{-3}, $N_D = 5 \cdot 10^{17}$ cm^{-3}, $k_g = 2.4 \cdot 10^4$ cm^{-1};

In Fig.4-10, $N_A = 1.5 \cdot 10^{16}$ cm^{-3}, $N_D = 5 \cdot 10^{17}$ cm^{-3}, $k_g = 8 \cdot 10^3$ cm^{-1} (smaller k_g);

In Fig.4-11, $N_A = 1.5 \cdot 10^{16}$ cm^{-3}, $N_D = 5 \cdot 10^{17}$ cm^{-3}, $k_g = 7.2 \cdot 10^4$ cm^{-1} (bigger k_g).

DC field: 4 kv/cm

$N_A = 1.5 \cdot 10^{16}$ cm^{-3} $N_D = 5 \cdot 10^{17}$ cm^{-3}
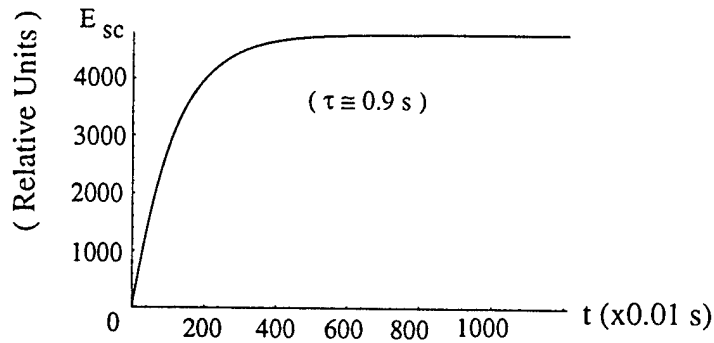
smaller k (k=8.0$\cdot 10^3$ 1/cm)

($\tau \cong 0.9$ s)

Fig. 4-10

DC field: 4 kv/cm

$N_A = 1.5 \cdot 10^{16}$ cm^{-3} $N_D = 5 \cdot 10^{17}$ cm^{-3}
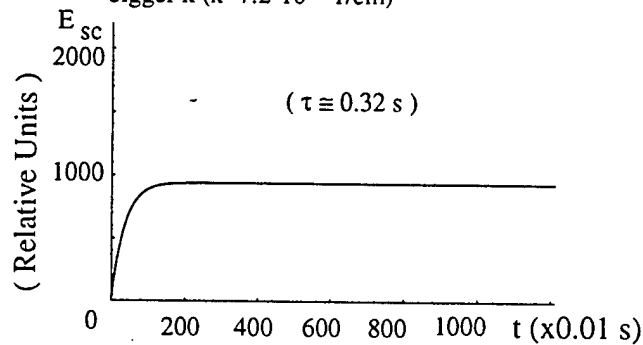
bigger k (k=7.2$\cdot 10^4$ 1/cm)

($\tau \cong 0.32$ s)

Fig. 4-11

The curves showed that (1) a smaller k_g produced a longer response time ; (2) a

bigger k_g produced a shorter response time but a smaller enhancement in the

magnitude of the space-charge field. We plotted the curves of τ versus N_D and τ
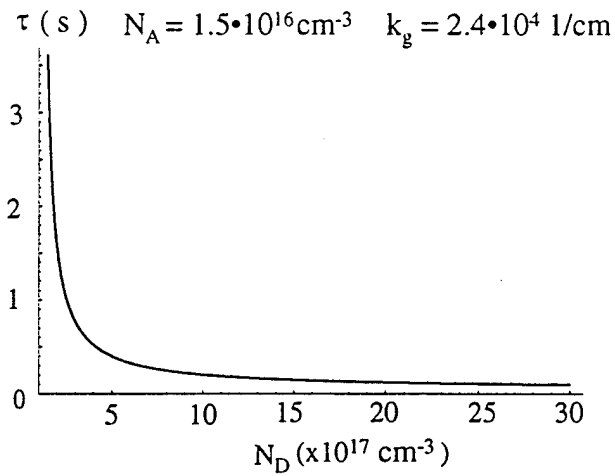
versus k_g, which are shown in Fig.4-12 and Fig.4-13.

τ (s) $N_A = 1.5 \cdot 10^{16} cm^{-3}$ $k_g = 2.4 \cdot 10^4$ 1/cm

Fig. 4-12 Dependence of Response Time on N_D

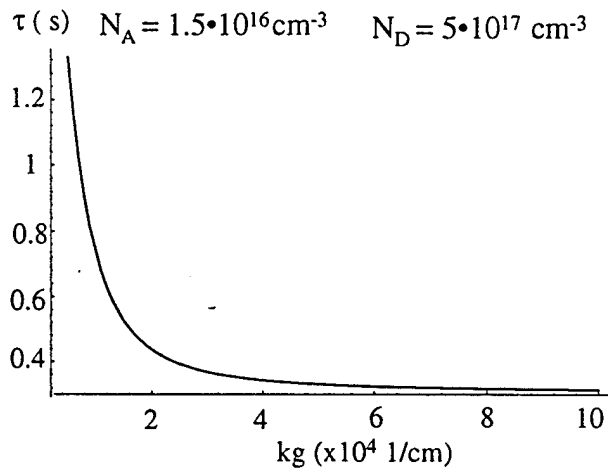τ (s) $N_A = 1.5 \cdot 10^{16} cm^{-3}$ $N_D = 5 \cdot 10^{17} cm^{-3}$

Fig. 4-13   Dependence of Response Time on kg

From Fig.4-12 we can see that a bigger N_D makes a shorter τ, and from Fig.4-13 we see that a bigger k_g makes a shorter τ. The physical explanation is that (1) A bigger N_D makes a shorter τ_I, thereby, produces a shorter response time; (2) A bigger k_g makes a shorter τ_E. As τ_E gets approximately equal to or less than τ_R, the response time will be reduced. So from these two curves we are able to

36

predict the optimum N_D and k_g values. For a DC field of 4 kv/cm, if N_A value was more or less than $1.5 \cdot 10^{16}$ cm^{-3}, the numerical results showed that the response time was longer than the case with N_A value of $1.5 \cdot 10^{16}$ cm^{-3}. Therefore, for a DC field of 4 kv/cm and $\gamma_R = 10^{-9}$ cm^3/s, the N_A value of $1.5 \cdot 10^{16}$ cm^{-3} is the optimum value for getting a fast response time, and the optimum N_D and k_g values are $5 \cdot 10^{17}$ cm^{-3} and $2.4 \cdot 10^4$ cm^{-1}, respectively. In the general case, for a DC field of 4 kv/cm the optimum N_A value is about $1.5 \cdot 10^7 / \gamma_R$ cm^{-3}, and the curve of response time versus N_D and the curve of response time versus k_g are similar to Fig.4-12 and Fig.4-13. Therefore, we can estimate that the optimum N_D value is about 30 times of N_A value and the optimum k_g value is in the range of $2 \cdot 10^4$ cm^{-1} to $3 \cdot 10^4$ cm^{-1}. In other words, the optimum full crossing angle between two beams is in the range of $8°$ to $13°$.

Experimental Setup And Data Presentation

Experimentally, we measured the photorefractive signals by applying a DC field across a crystal. Our experimental research can be described as follows.

(1). The measurement technique adopted in the experiment included beam fanning and two beam coupling.

(2). Samples measured by us included a heavily doped BSKNN crystal which had a larger value of N_D and N_A, and an undoped BSKNN crystal which had a smaller

value of N_D and $N_A.$

(3). Each sample was measured with no field and with an applied field across it .

Experimental Apparatus

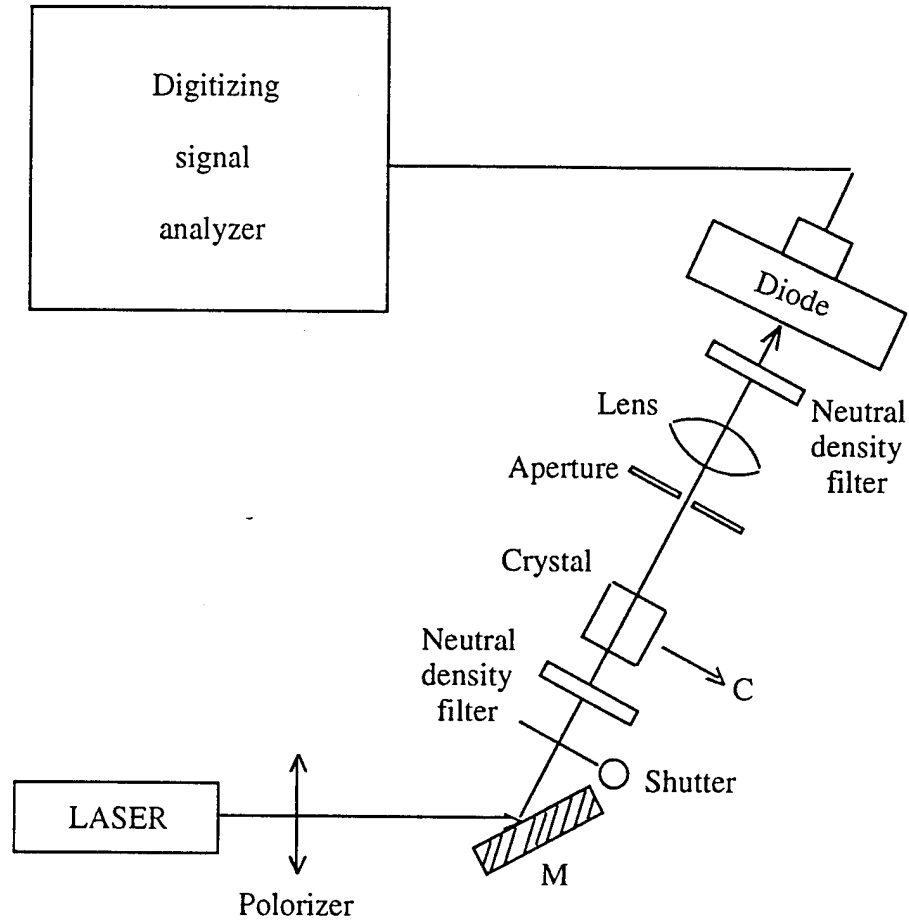The experimental setup for beam fanning is shown in Fig.4-14. The laser we used

Fig. 4-14 Experimental setup for beam fanning

experiment was a Coherent Argon-ion Laser. The laser beam of 458 nm wavelength

with an extraordinary polarization was incident to a crystal in the direction

perpendicular to the c-axis of the crystal. The transmitted beam was detected by a

photodiode through an aperture. The signal was then sent to a 602A Digitizing Signal

Analyzer to be measured. In order to measure the photorefractive effect with a DC

field a high voltage needs to be applied across a crystal. Two copper tapes were pasted

on a crystal by using silver paste and the electrodes were connected to a high voltage

supply. A high voltage was provided by a TREK Model 610C H.V. SUPPLY

AMPLIFIER/CONTROLLER which had a maximum output of 10 kv/cm.

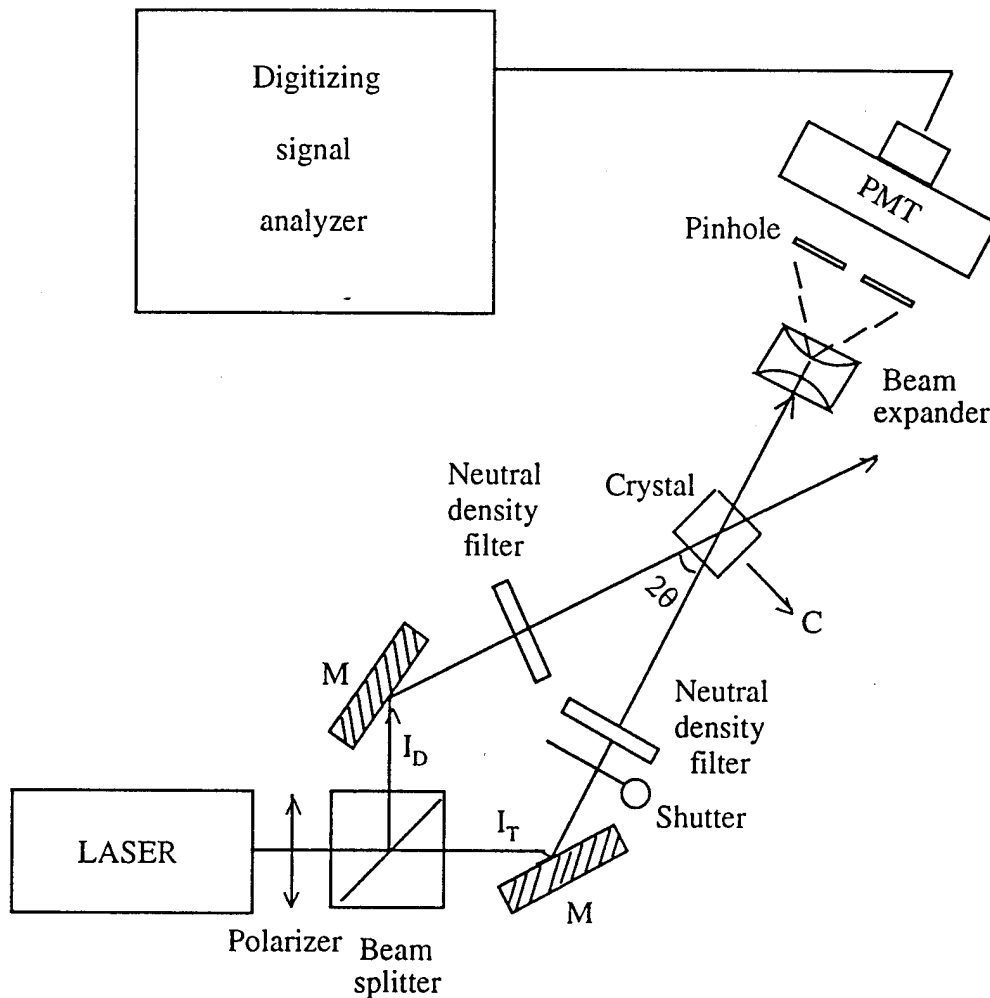The setup for two beam coupling is shown in Fig.4-15. The laser output with

Fig. 4-15   Experimental setup for two beam coupling

ordinary polarization and a wavelength of 458 nm was split into two beams. By using

neutral density filters we made the intensity of one beam much stronger than the other.

The full crossing angle between two beams was 10°. The crystal was oriented to have

its normal line bisecting the two beams. In our experiment the transmitted intensity of

the weak beam was measured. The signal was detected by a photomultiplier (PMT)

and sent to a 602A DSA to be measured.

Measurement and Data Presentation

Experimentally, we measured the beam fanning signal for two different BSKNN

crystals with no field and with a DC field. For the BSKNN sample which was heavily

doped, the measured results are shown in Fig.4-16 (no field), 4-17 (DC field 3.6

kv/cm), and 4-18 (DC field 5.6 kv/cm). The data measured from Fig.4-16 through

Fig.4-18 are listed in table 4-1.

Table 4-1 Data of Beam Fanning with a DC Field

Sample 1: BSKNN heavily doped

Wavelength: 458 nm (Extraordinary polarization)

Figure No	Magnitude of Field E_0 (kv/cm)	Optical Intensity I (mw/cm^2)	Transmission Coefficient* T	Response Time τ (s)
Fig.4-16	0	250	3.0%	3.5
Fig.4-17	DC: 3.6	250	1.4%	1.0
Fig.4-18	DC: 5.6	250	1.1%	0.46

* The transmission coefficient T is defined as a ratio of the

transmitted beam intensity at equilibrium to the initial

intensity of that beam.

Beam Fanning

BSKNN heavily doped

$I = 250 \ mw/cm^2$

no field $\qquad$ ($\tau \cong 3.5 \ s$)
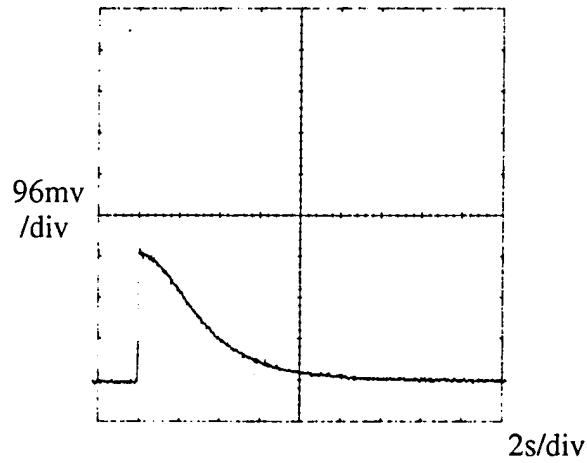

96mv /div

2s/div

Fig. 4-16

Note: This experimental curve was shown on the screen of DSA oscilloscope. The vertical axis gave the intensity of the transmitted beam.

Beam Fanning

BSKNN heavily doped

$I = 250 \text{ mw/cm}^2$

DC field: 3.6 kv/cm ($\tau \cong 1.0$ s)

95.5mv
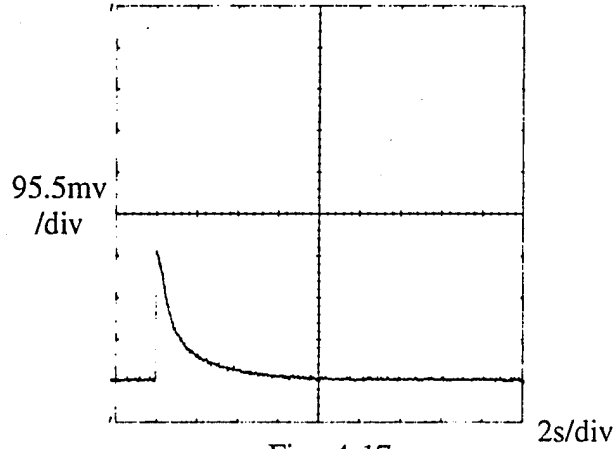/div

2s/div

Fig. 4-17

Beam Fanning

BSKNN heavily doped

$I = 250 \text{ mw/cm}^2$

DC field: 5.6 kv/cm   ($\tau \cong 0.46$ s)
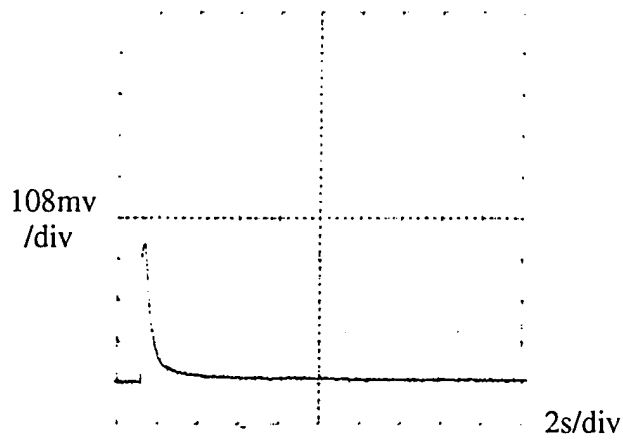
108mv
/div

2s/div

Fig. 4-18

Using an undoped BSKNN sample, the measurement results are shown in Fig.4-19 (no

field) and 4-20 (DC field 4 kv/cm). For the undoped BSKNN crystal we also

43

measured a beam fanning signal while focusing the beam into the crystal in order to make the optical intensity in the crystal about 4 times stronger. The results are shown in Fig.4-21 (no field) and 4-22 (DC field 4 kv/cm). The data measured from Fig.4-19 through Fig.4-22 are listed in table 4-2.

<div align="center">Table 4-2 Data of Beam Fanning with DC Field</div>

Sample 2: BSKNN undoped

Wavelength: 458 nm (Extraordinary polarization)

Figure No	Magnitude of Field E_0 (kv/cm)	Optical Intensity I (mw/cm^2)	Transmission Coefficient* T	Response Time τ (s)
Fig.4-19	0	160	90.0%	5.6
Fig.4-20	DC: 4.0	160	18.5%	1.5

The following figures are for beam fanning with focusing.

Fig.4-21	0	640	90.0%	1.1
Fig.4-22	DC: 4.0	640	19.8%	0.6

* The transmission coefficient T is defined as a ratio of the transmitted beam intensity at equilibrium to the initial intensity of that beam.

Beam Fanning

BSKNN undoped $I = 160$ mw/cm^2

no field   ($\tau \cong 5.6$ s)
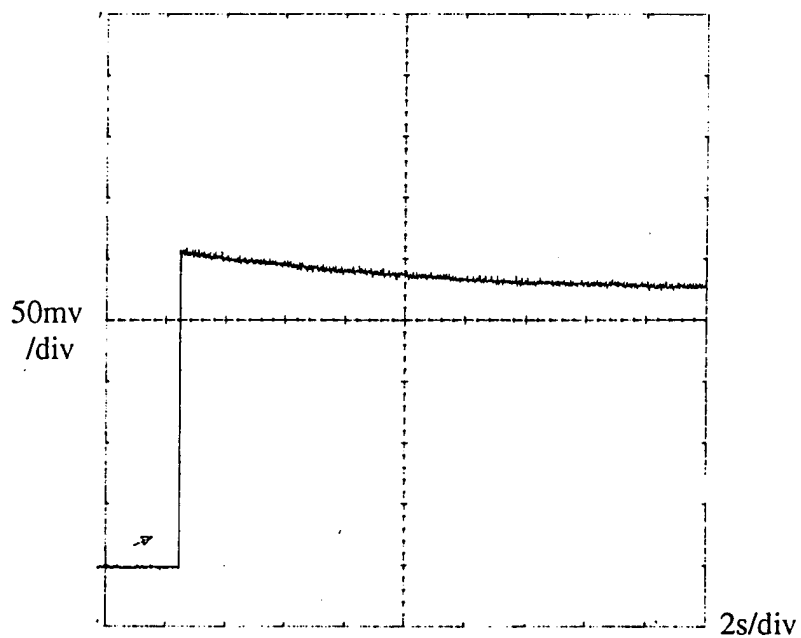

50mv
/div

2s/div

Fig. 4-19

DC field: 4 kv/cm   ($\tau \cong 1.5$ s)
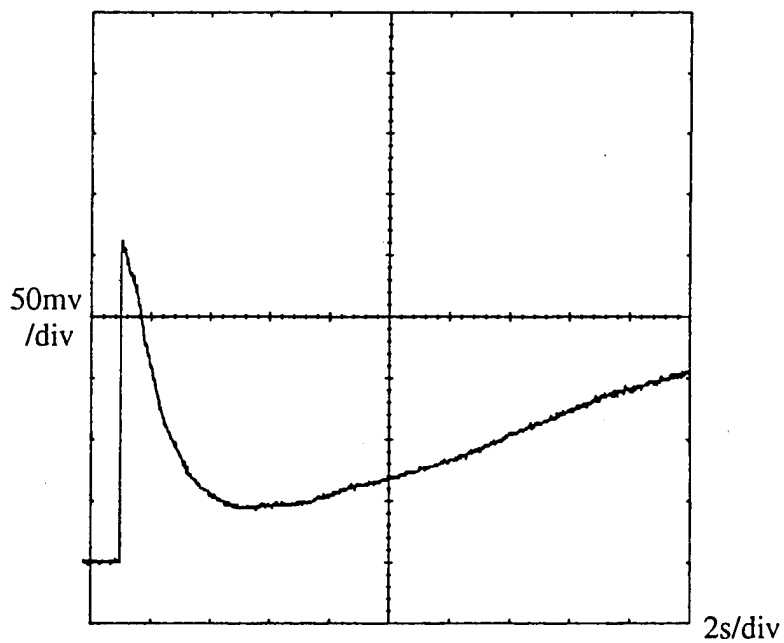
50mv
/div

2s/div

Fig. 4-20

45

Beam Fanning with Focusing

BSKNN undoped $I = 640$ mw/cm^2

no field   ($\tau \cong 1.1$ s)

50mv
/div

Fig. 4-21   2s/div

DC field: 4 kv/cm   ($\tau \cong 0.6$ s)

50mv
/div

Fig. 4-22   2s/div
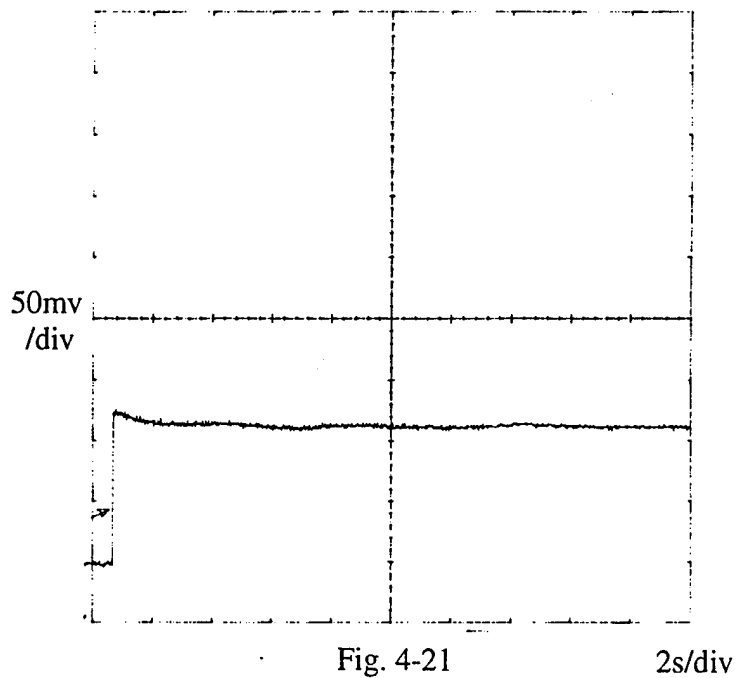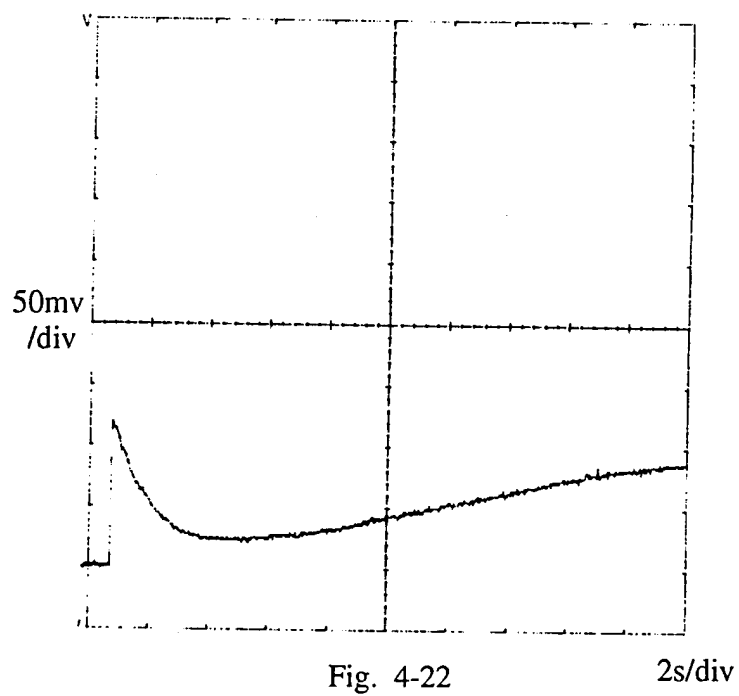
As expected these results show that by focusing the speed of response can be decreased. In fact, when the spot size is greatly reduced to 30 μm (in SBN) the response time was extremely fast. The experimental results are shown in Fig.4-23, which gave the transmitted intensity as a function of time for an input power of about 0.04 mw. As can be seen from the curve, the characteristic response time is on the order of 800 ms.
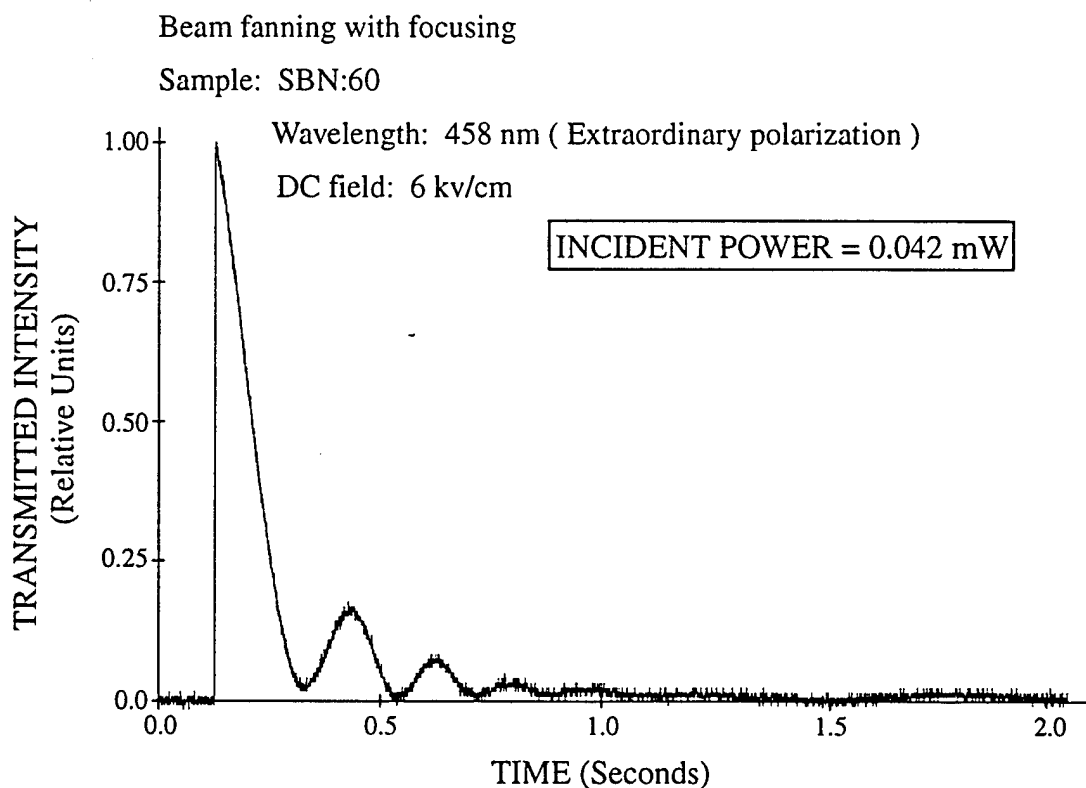
Beam fanning with focusing

Sample: SBN:60

Fig. 4-23 Transmitted Intensity with Applying Field and Focusing Beam

Comparing the data shown in Fig.4-16, 4-17 and 4-18, we see that with an increase in applied DC field: (1) the transmission coefficient is decreasing which

means the energy exchange is increasing; and (2) the response time is getting shorter. Similar results are also obtained from the comparison of Fig.4-19 with Fig.4-20.

By comparing Fig.4-19 with 4-21 and Fig.4-20 with 4-22, we see that with focusing the beam, the photorefractive response time gets shorter without a trade off in sensitivity. So on the use of an applied field, the response time can be further decreased with focusing the laser beams.

In Fig. 4-20 (also in Fig. 4-22) we see a field screening that is caused by the applied DC field. A few seconds after turning the laser beam on, the intensity of the transmitted beam starts increasing. In other words, the space-charge field was getting smaller. This is due to the electric field screening.

In Fig.4-23 we see an oscillation in the beam fanning signal. This agrees with the theoretical prediction in section I of this chapter. According to eq.(4-6), the oscillation frequency of the space-charge field is

$$\omega \propto (\tau_R/\tau_E)/[\, (1+\tau_R/\tau_D)^2 + (\tau_R/\tau_E)^2 \,]$$

With no applied field ($1/\tau_E = 0$), ω is zero. With an increase in an applied field, ω can be seen to increase. In this experiment, we applied a strong electric field ($E_0 = 6$ kv/cm) to the crystal. Therefore, with a strong applied field we can make the frequency very large. That's why we see an oscillation in the beam fanning signal.

In the two beam coupling experiments we measured an intensity time evolution of the weak beam for the BSKNN undoped crystal. Fig.4-24 is the experimental curve

48

with no field and Fig.4-25 is with a DC field of 3.6 kv/cm. The data measured from

Fig.4-24 and Fig.4-25 are listed in table 4-3.

Table 4-3 Data of Two Beam Coupling with DC Field

Sample 2: BSKNN undoped

Wavelength: 458 nm (Ordinary polarization)

Full Crossing Angle: $2\theta=10°$

Figure No	Magnitude of Field E_0 (kv/cm)	Intensity of Weak Beam I_1 (mw/cm^2)	Intensity of strong Beam I_2 (mw/cm^2)	m	Relative Energy Exchange** $\Delta I_1/I_1$	Response Time τ (s)	Modu-lation*
Fig.4-24	0	0.6	64	0.2	0.1		9.0
Fig.4-25	DC: 3.6	0.6	64	0.2	0.9		5.0

$$m =2(I_1 I_2)^{1/2}/ (I_1+I_2)$$

* The modulation is defined as a ratio of the oscillation amplitude to

  the signal magnitude.

** The relative energy exchange is defined as a ratio of the intensity

  gain to the original intensity.

The basic idea is to examine if the two-beam coupling can be enhanced in both magnitude and speed with an applied D.C. field. In fact we will show that for SBN and BSKNN this is indeed the case. The problem however is that screening of the applied field leads to a loss of this enhancement after a time about equal to the dielectric response time, or about ten times longer than the photorefractive response time. Figure 4-24 and 4-25 demonstrate that the response time and the magnitude of the two-beam coupling are enhanced with an applied field. In fact the response time improves from 9 seconds to 5 seconds and the energy transfer increases many fold over the no field case. The only difference between figures 4-24 and 4-25 is that a field of 3.6 KV/cm is applied for figure 4-25. Notice that the enhancement, however, is gradually lost as a function of time due, to screening of the applied field.

Two - beam coupling   BSKNN undoped   Total I = 64 mw/cm^2

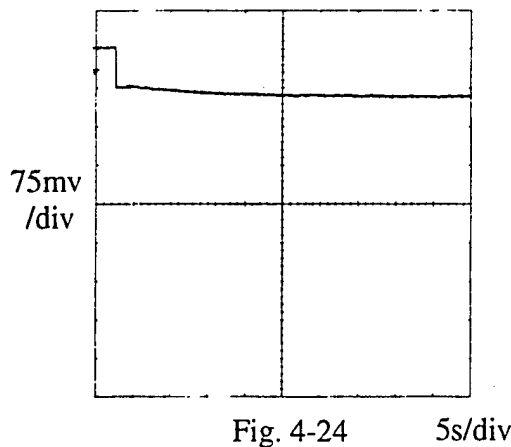Full crossing angle: 10° no field   ($\tau \cong 9.0$ s)

75mv
/div

Fig. 4-24   5s/div

Two - beam coupling   BSKNN undoped   Total I = 64 mw/cm^2

Full crossing angle: 10° DC field: 3.6 kv/cm   ($\tau \cong 5.0$ s)

68.5mv
/div

Fig. 4-25   5s/div
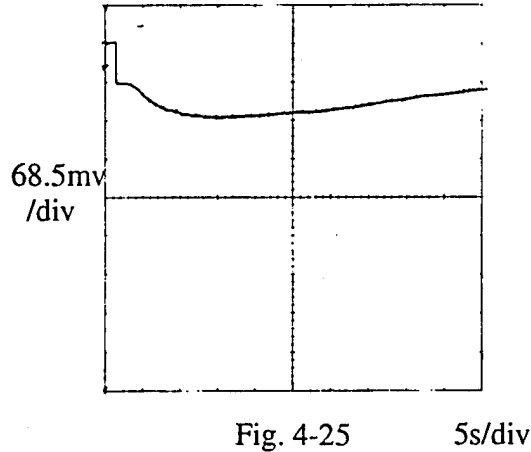
We also measured the signal of the weak beam by focusing both beams into the crystal.

The results using two focused beams are shown in Fig.4-26, 4-27, 4-28 and 4-29. The

51

data measured from Fig.4-26 through Fig.4-29 are listed in table 4-4.

Table 4-4 Data of Two Focused Beam Coupling with DC Field

Sample 2: BSKNN undoped

Wavelength: 458 nm (Ordinary polarization)

Full Crossing Angle: $2\theta=10°$ (Focal Length of the Lens: 100 cm)

Figure No	Magnitude of Field E_0 (kv/cm)	Intensity of Weak Beam I_1 (mw/cm^2)	Intensity of strong Beam I_2 (mw/cm^2)	m	Relative Energy Exchange** $\Delta I_1/I_1$	Response Time τ (s)	Modulation*
Fig.4-26	0	2.6	260	0.2	0.1	4.0	
Fig.4-27	DC: 3.6	2.6	260	0.2	1.4	1.7	
Fig.4-28	0	26	2600	0.2	0.3	0.9	
Fig.4-29	DC: 3.6	26	2600	0.2	1.3	0.2	

$$m =2(I_1 I_2)^{1/2}/ (I_1+I_2)$$

* The modulation is defined as a ratio of the oscillation amplitude to the signal magnitude.

** The relative energy exchange is defined as a ratio of the intensity gain to the original intensity.

Two focused beam coupling   BSKNN undoped
Full crossing angle: 10° Total I = 260 mw/cm^2
no field   ($\tau \cong 4.0$ s)

75mv
/div

1s/div
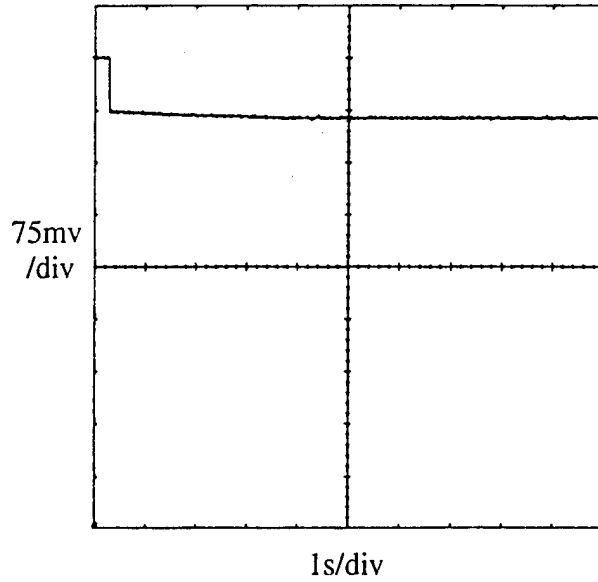
Fig. 4-26

DC field: 3.6 kv/cm   ($\tau \cong 1.7$ s)

75mv
/div

1s/div
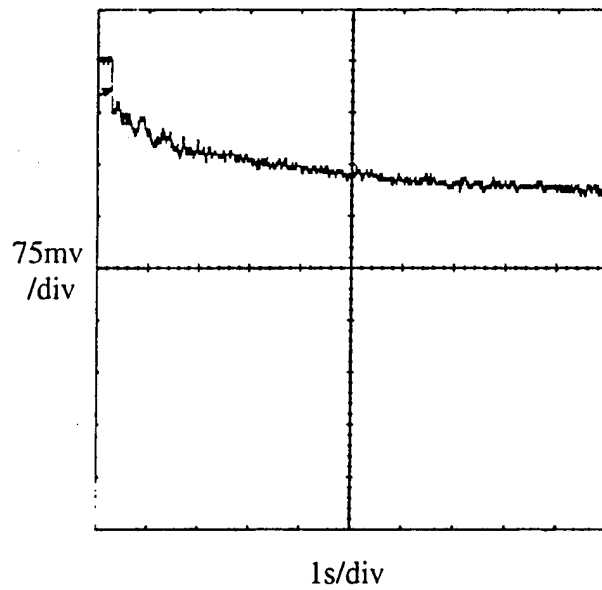
Fig. 4-27

Two focused beam coupling   BSKNN undoped

Full crossing angle: 10° Total I = 2.6 w/cm²
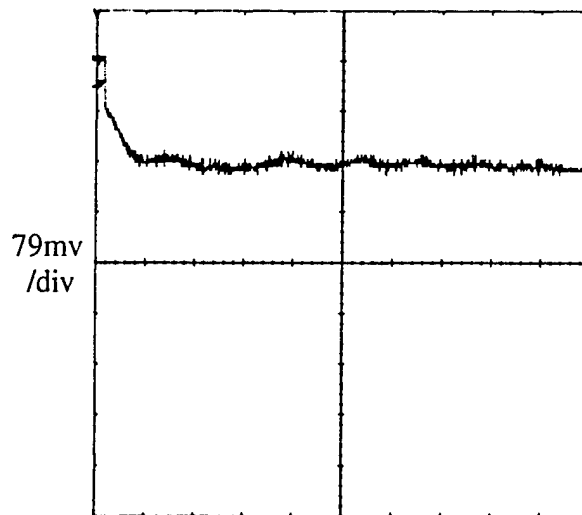
no field   ($\tau \cong 0.9$ s)

40mv
/div
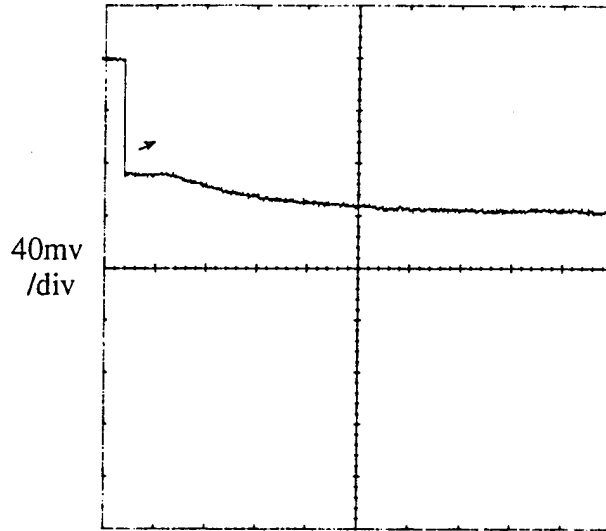
500ms/div

Fig. 4-28

DC field: 3.6 kv/cm   ($\tau \cong 0.2$ s)

79mv
/div

500ms/div

Fig. 4-29

By comparing Fig.4-24 (no field) with Fig.4-25 (DC field), Fig.4-26 (no field) with Fig.4-27 (DC field), Fig.4-28 (no field) with Fig.4-29 (DC field), it is shown that an applied DC field can really enhance the photorefractive effect in both the magnitude and the speed.

Direct Comparison Of The Theoretical Analysis

With The Experimental Results

Experimentally, we measured the intensity change of the weak beam due to two beam coupling. The gain of the weak beam is given by

$$I_{1c}/I_1 = (1 + c)\exp(\Gamma L_{eff})/[1 + c \bullet \exp(\Gamma L_{eff})] \qquad (4\text{-}8)$$

But as the weak beam is much weaker than the strong beam, then the diffraction signal due to the strong beam can not be neglected. Under this circumstance, the intensity measured from the weak beam would include two parts: one is the energy gain of the weak beam and the other is the diffraction signal of the strong beam due to the grating. If the two-beam energy-coupling gain coefficient of the weak beam is Γ and the diffraction signal from the strong beam is D, Γ in eq. (4-8) would be replaced by (Γ^2 + D^2)$^{1/2}$.

$$\frac{I_{1c}}{I_1} = \frac{(1+ c) \, e^{\sqrt{\Gamma^2 + D^2} L_{eff}}}{1 + c \, e^{\sqrt{\Gamma^2 + D^2} L_{eff}}} \qquad (4\text{-}9)$$

By using eq. (4-9) we can convert the measured intensity change to $(\Gamma^2 + D^2)^{1/2}$. On the other hand we can convert the space-charge field obtained numerically to the gain coefficient Γ of the weak beam. Then the comparison of two gains, experimental and theoretical, will give us a direct comparison.

A. Gain coefficient obtained from the experimental data

The experimental data we used for deriving $(\Gamma^2 + D^2)^{1/2}$ are shown in Fig. 4-28 and Fig. 4-29. For the data we used, c is 1/100 and L_{eff} is about 4 mm. For small gain, therefore according to eq. (4-8), we can get

$$I_{1c}/I_1 \cong \exp(\sqrt{\Gamma^2 + D^2}L_{eff})$$

Then
$$\sqrt{\Gamma^2 + D^2} \cong \ln(I_{1c}/I_1)\Big/L_{eff}$$

This equation enables us to obtain the total magnitude of both the gain coefficient and the diffraction signal from the intensity change which we measured experimentally. In the experiment, after a grating was formed inside the crystal we blocked the weak detected beam and measured only the diffraction signal from the strong beam. The diffraction signal was found to be one fourth of the energy exchange signal. So we can get $(\Gamma^2 + D^2)^{1/2} \cong (\Gamma^2 + \Gamma^2/4)^{1/2} \cong 1.1\Gamma$. Then based on the data in Fig. 4-28 (no field) and Fig. 4-29 (DC field) we calculated the corresponding Γ versus time, which are shown in Fig. 4-30 and 4-32. From these figures we can determine the response time for each case.

B. Gain coefficient obtained from the numerical computation

Numerically, by using the same data as in the experiment and varying the parameters

Using a Cylindrical Lens and an Applied Electric Field.

While focusing coupled with an applied D.C. seems promising it suffers from the screening effect seen in figures 4-20 and 4-22. That is, after some time charges move to the edges of the incident beam and produce a screening field which brings to zero the enhancement of the applied field. This can be avoid using a c focus the incident beam in one direction only and maintains an optically induced electrical path between electrodes. As a result, using both an applied D.C. field along with the cylindrical lens for focusing an enhancement of four orders of magnitude is possible. While this is still marginal it does accomplish the speed enhancement without loss of O.D. due to screening.

Conclusions

Our results, both theory and experiment, clearly show that the application of an electric field can enhance both the speed and the magnitude of the photorefractive effect. In fact, the data and modeling clearly show that the use of a sperical lens to focus to about 100 micron spot size with an applied field gives the four order of magnitude improvement in the response time that we were seeking. This is accomplished without sacrificing O.D. The problem is that focusing with an applied field leads to the screening effect. However, the case of an applied field with a cylinderical lens is very successful since the incident light fills the crystal.

V. APPLIED A.C. ELECTRIC FIELD

The photorefractive effect can be enhanced by applying a DC field across a crystal. An applied DC electric field can (1) enhance the magnitude of the space-charge field and corresponding photorefractive-index change and (2) speed up the photorefractive response time. However, the technique of applying a DC field has some drawbacks or disadvantages of its own (Ref. [1]-[4]. Equation (4-4) showed a phase shift between the space-charge field and the intensity pattern. When there is no applied field, the phase shift is 90°, which gives the maximum energy exchange between two beams. But, if a DC field E_0 is turned on the phase will no longer preserve the 90° shift and energy exchanged between two beams is diminished. A second problem is that screening of the DC field is observed. That is, when a DC field is applied across a crystal the electrons in the conduction band move in one direction. As electrons move to the edge of the illuminated area the separated positive and negative charges will be frozen there and a screening of the applied field will occur. As a result of screening the enhancement in the magnitude and speed of the photorefractive effect is lost. Experimentally, it is easy to observe the screening effect. Fig. 4-20, Fig. 4-22 and Fig. 4-25 in last chapter demonstrates a field screening with an applied field. After a short time the enhancement in magnitude of the photorefractive effect is lost. These two disadvantages, however, can be avoided using an applied AC field.
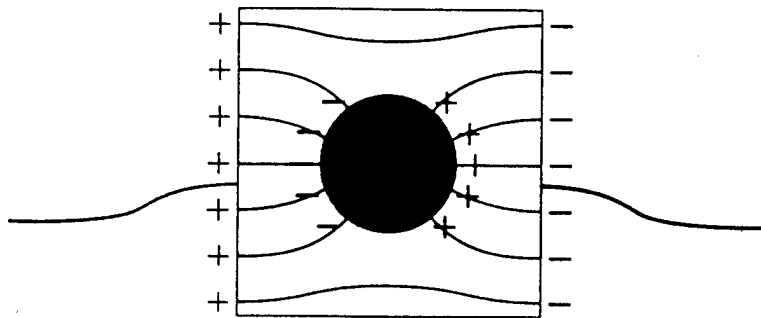
SCREENING OF EXTERNAL FIELD

58

Two focused beam coupling

BSKNN undoped

Full crossing angle: 10°

no field

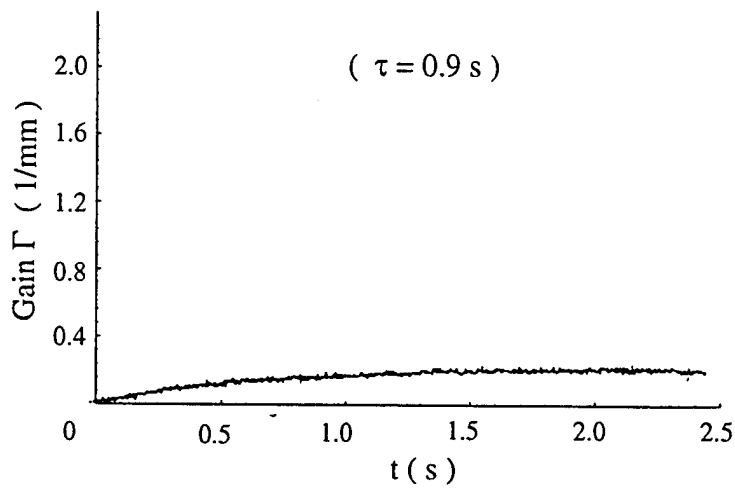Total I = 2.6 w/cm²

(τ = 0.9 s)

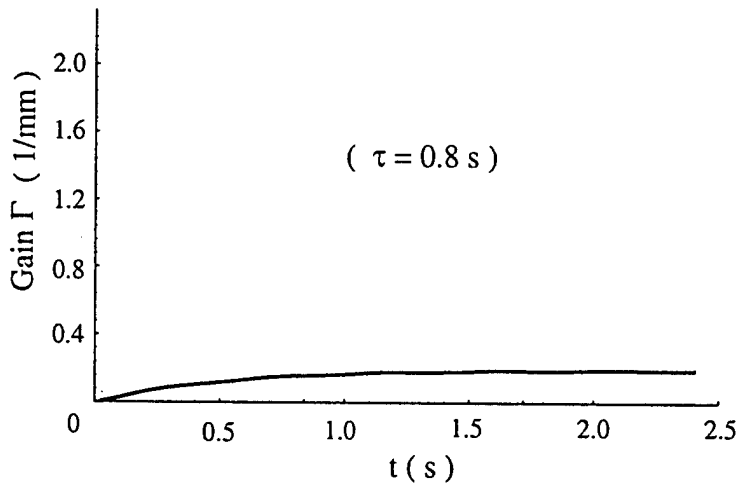Fig. 4-30 Experimental curve

(τ = 0.8 s)

Fig. 4-31 Theoretical curve

Two focused beam coupling

BSKNN undoped

Full crossing angle: 10°

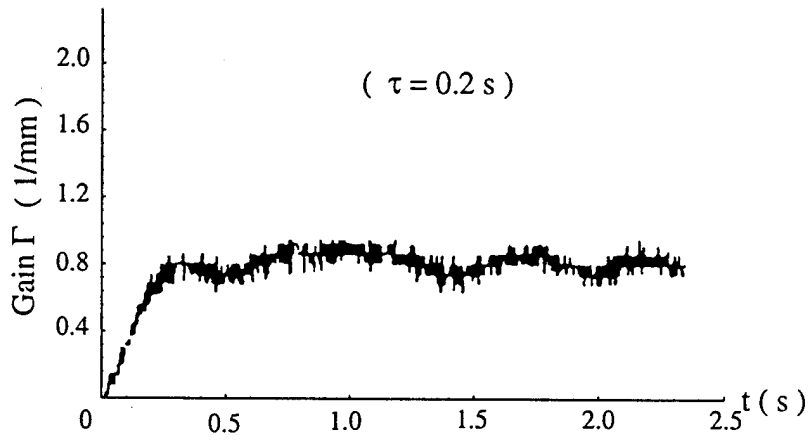DC field: 3.6 kv/cm

Total I = 2.6 w/cm²
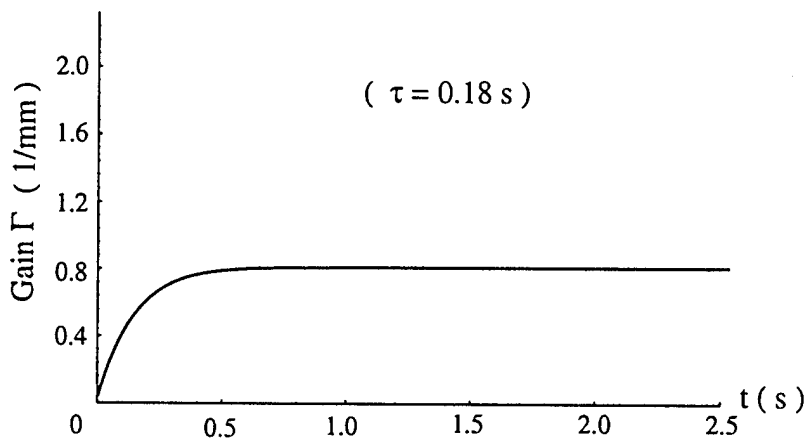

Fig. 4-32 Experimental curve

Fig. 4-33 Theoretical curve

Analytical Solution For Space-Charge Field With An

Applied Square-Wave AC Field Of A Short Period

The applied square-wave AC field is

$$E_{AC} = E_0 \text{ for } 0 < t \leq T/2 \text{ or}$$

$$= -E_0 \text{ for } T/2 < t \leq T$$

where T is the period of square-wave field and the range of T is $\tau_R \ll T \ll \tau$ (τ: the photorefractive response time).

The space-charge field with a DC field is given by Eq. (4-2)

$$E_1(t) = E_{SC}(-e^{i\varphi} \cdot e^{-t/\tau} \cdot e^{-i\omega t} + e^{i\varphi})$$

where E_{SC} is given by Eq. (4-3).

We define a non-dimensional physical quantity $E_1'(t)$ as

$$E_1(t) = E_{sc} \cdot E_1'(t)$$

Then E_1' at the end of each negative half period, i.e., when $t = nT$, is given by (see Appendix II)

$$E_1'(nT) = (\frac{1-e^{-nT/\tau}}{1-e^{-T/\tau}})(-e^{i\varphi} \cdot e^{-T/\tau} + e^{i\varphi} \cdot e^{i\omega T/2} \cdot e^{-T/2\tau}$$

$$-e^{-i\varphi} + e^{-i\varphi} \cdot e^{i\omega T/2} \cdot e^{-T/2\tau}) \qquad (5-1)$$

(n = 1, 2, 3... is the period order of the square-wave field)

Meantime, E_1' at the end of each positive half period, i.e. when $t = (n + 1/2) T$, is

$$E_1'[(n+\frac{1}{2})T] = (\frac{1-e^{-nT/\tau}}{1-e^{-T/\tau}}) \cdot (e^{-i\varphi} \cdot e^{-T/\tau} - e^{-i\varphi} \cdot e^{-i\omega T/2} \cdot e^{-T/2\tau})$$

$$+ (\frac{1-e^{-(n+1)T/\tau}}{1-e^{-T/\tau}})(e^{i\varphi} - e^{i\varphi} \cdot e^{-i\omega T/2} \cdot e^{-T/2\tau}) \quad (5\text{-}2)$$

Since the solution to the differential equation of space-charge field (see eq. (4-1)) can also be written as

$$E_1(t) = E_{SC}\{[E_1'(t_0) - e^{i\varphi}] \cdot e^{-(t-t_0)/\tau} \cdot e^{-i\omega(t-t_0)} + e^{i\varphi}\}$$

Therefore, E_1' during each positive half period is

$$E_1'(t) = [E_1'(nT) - e^{i\varphi}] \cdot e^{-t'/\tau} \cdot e^{-i\omega t'} + e^{i\varphi} \quad (0 < t' \le T/2) \quad (5\text{-}3)$$

During each negative half period

$$E_1'(t) = \{E_1'[n+1/2)T] + e^{-i\varphi}\} \cdot e^{-t'/\tau} \cdot e^{-i\omega t'} - e^{-i\varphi} \quad (0 < t' \le T/2) \quad (5\text{-}4)$$

Eqs. (5-1), (5-2), (5-3) and (5-4) constitute the basic equations for space-charge field under an applied square-wave AC field. In the case of $T \ll \tau$ two results can be derived.

1.   In general $\tau_D \gg \tau_R$, so that $\tau_R/\tau_D \approx 0$. In addition, for not very large applied field $\tau_E \gg \tau_R$, so that $\tau_R/\tau_E \approx 0$. We, therefore, can write the following expression.

$$(\frac{\tau_R}{\tau_E}) - \frac{\tau_R}{\tau_D} - (\frac{\tau_R}{\tau_E})^2 < \frac{\tau_I}{\tau_{di}} + \frac{\tau_I}{\tau_{di}}(\frac{\tau_R}{\tau_E})$$

$$(\frac{\tau_R}{\tau_E})(1 - \frac{\tau_I}{\tau_{di}}) < \frac{\tau_I}{\tau_{di}}[1 + \frac{\tau_R}{\tau_D}\frac{\tau_{di}}{\tau_I} + (\frac{\tau_R}{\tau_E})^2(\frac{\tau_{di}}{\tau_I})]$$

$$\frac{\tau_R}{\tau_E}(\frac{\tau_{di}}{\tau_I} - 1) < [1 + \frac{\tau_R \tau_{di}}{\tau_D \tau_I}] + (\frac{\tau_R}{\tau_E})^2(\frac{\tau_{di}}{\tau_I})$$

Then we get

$$-\frac{\tau_R}{\tau_E}\left(\frac{\tau_{di}}{\tau_I}-1\right)<\left[1+\frac{\tau_R\tau_{di}}{\tau_D\tau_I}\right]\left(1+\frac{\tau_R}{\tau_D}\right)+\left(\frac{\tau_R}{\tau_E}\right)^2\left(\frac{\tau_{di}}{\tau_I}\right)\tag{5-5}$$

Let's go back to Ch.4 and look at Eq. (4-5) and Eq. (4-6). It's not difficult to find that Eq. (5-5) yields a relation of $1/\tau > \omega$. Therefore, if $T \ll \tau$, then $T \ll 1/\omega$ or $\omega T \ll 1$. This relation will be used in the following derivation.

2. In the case of $T \ll \tau$ only after many many periods of AC field (in other words., n must be a very large number) an equilibrium can be reached. So we will have

$$(n + 1)\, T/\tau \approx n\, T/\tau \qquad \text{for } n \gg 1$$

Thus Eq. (5-2) becomes

$$E_1{}'[(n+\frac{1}{2})\,T] = \left(\frac{1-e^{-nT/\tau}}{1-e^{-T/\tau}}\right)\cdot\left(e^{-i\varphi}\cdot e^{-T/\tau}-e^{-i\varphi}\cdot e^{-i\omega T/2}\cdot e^{-T/2\tau}\right.$$
$$\left.+\ e^{i\varphi}-e^{i\varphi}\cdot e^{-i\omega T/2}\cdot e^{-T/2\tau}\right)\tag{5-6}$$

From either Eq. (5-1) or Eq. (5-6), both will have the same result for the imaginary part

$$\operatorname{Im}E_1{}'[\ nT\ \text{or}\ (n+1/2)T\ ] =$$

$$\left(\frac{1-e^{-nT/\tau}}{1-e^{-T/\tau}}\right)[-e^{-T/\tau}\sin\varphi+e^{-T/2\tau}\sin\left(\omega T/2+\varphi\right)$$
$$+\sin\varphi+e^{-T/2\tau}\sin\left(\omega T/2-\varphi\right)]\tag{5-7}$$

Eq. (5-7) shows that in the end of each half period of AC field (whatever

63

positive or negative half period) the space-charge field stands the same.

From this analysis we can examine the response time and the phase shift.

When an equilibrium state is established n must be a large number, or in other

words, $n \to \infty$ in Eq. (5-7), then the equilibrium value of the imaginary part

of the space-charge field is

$$\text{Im } E_1'^{eq} = (\frac{1}{1 - e^{-T/\tau}}) \, [-e^{-T/\tau} \sin \varphi + e^{-T/2\tau} \sin (\omega T/2 + \varphi)$$

$$+ \sin \varphi + e^{-T/2\tau} \sin (\omega T/2 - \varphi)] \qquad (5\text{-}8)$$

When $\text{Im } E_1'^{eq}$ reaches its e^{-1} value or when $nT/\tau = 1$, Eq. (5-7) becomes

$$\text{Im } E_1'(nT/\tau = 1) = (\frac{1 - e^{-1}}{1 - e^{-T/\tau}}) \, [-e^{-T/\tau} \sin \varphi + e^{-T/2\tau} \sin (\omega T/2 + \varphi)$$

$$+ \sin \varphi + e^{-T/2\tau} \sin (\omega T/2 - \varphi)]$$

$$= (1 - 1/e) \, \text{Im } E_1'^{eq}$$

$$(5\text{-}9)$$

That is the field reaches its e^{-1} value after time $nT/\tau = 1$ or $nT = \tau$. But τ is

also the time for the space-charge field to reach its e^{-1} value for same applied

DC field. Therefore, this tells us that the response time, in the case of

applying a square-wave AC field, with a period of $T \ll \tau$, is the same as in

the case of applying a DC field.

To see the phase shift in equilibrium, for $T \ll \tau$ we can make an

approximation

$$e^{-T/(2\tau)} \approx e^0 = 1$$

Then from Eq. (5-1), for $n \to \infty$

$$\text{Re}E_1' (nT) = (\frac{1}{1-e^{-T/\tau}}) [-\cos\varphi + \cos(\omega T/2 + \varphi)$$
$$-\cos\varphi + \cos(\omega T/2 + \varphi)]$$

$$= -(\frac{1}{1-e^{-T/\tau}}) \cos\varphi (\frac{\omega T}{2})^2 \quad \text{since } \omega T/2 << 1$$

Due to the same reason, for $n \to \infty$

$$\text{Im}E_1' (nT) = (\frac{1}{1-e^{-T/\tau}}) \cos\varphi (\omega T)$$

If we write the complex number $E_1' (nT)$ as

$$E_1' (nT) = | E_1' (nT) | \cdot e^{i\vartheta}$$

then $\tan\vartheta = \text{Im}E_1' (nT)/\text{Re}E_1' (nT) = -4/(\omega T) \to -\infty$ for $\omega T << 1$

we will get

$$\vartheta \approx 90° + \varepsilon \qquad\qquad (5\text{-}10)$$

where ε is an infinitesimal.

Also from eq (5-2), by using the same way as above we can get for $n \to \infty$

$$\text{Re}E_1' ((n+1/2) T) = (\frac{1}{1-e^{-T/\tau}}) \cos\varphi (\frac{\omega T}{2})^2$$

$$\text{Im}E_1' ((n+1/2) T) = (\frac{1}{1-e^{-T/\tau}}) \cos\varphi (\omega T)$$

We write $E_1' ((n+1/2) T) = |E_1' ((n+1/2) T)| \cdot e^{i\psi}$

$$\tan\psi = \text{Im}E_1' ((n+1/2) T)/\text{Re}E_1' ((n+1/2) T) = 2/(\omega T) \to \infty$$

for $\omega T << 1$

$$\psi \approx 90° - \varepsilon \qquad\qquad (5\text{-}11)$$

65

Eqs (5-10) & (5-11) show that the phase shift is always about 90° in both the positive and negative half periods. Physically, this means that we can get a maximum energy exchange between two beams by applying a square-wave short period AC field to the crystal. This is a remarkable result.

Numerical Solution For Space-Charge Field With An
Applied Square Wave AC Field Of An Arbitrary Period

We have already obtained an analytical solution for the space-charge field with an applied square wave AC field of a very short period ($T \ll \tau$). But, in general, the photorefractive effect can be enhanced by applying an AC field with any period. Therefore, we have to resort to numerical solution for the space-charge field with an external square wave AC field of an arbitrary period. Considering that the applied AC field changes its value through a process of $+E_0 \rightarrow 0 \rightarrow -E_0$, therefore, we must make a transition between the positive and the negative fields when we look for a numerical solution for the space-charge field.

The crystal physical parameters for the AC field case are same as those for the DC field case in Chapter 4. The only difference is that a fixed DC field value E_0 is now replaced by an alternating field value $\pm E_0$. Fig.5-1, 5-2 and 5-3 show the space-charge field time evolution with an AC field for different N_A. Fig.5-4 and 5-5 show the space-charge field with an AC field of different frequency.

AC field $I = 100$ mw/cm^2 $kg = 2.4 \cdot 10^4$ 1/cm $f = 0.5$ Hz
$N_A = 5 \cdot 10^{16}$ cm^{-3} $N_D = 5 \cdot 10^{17}$ cm^{-3} ($\tau \cong 1.7$ s)
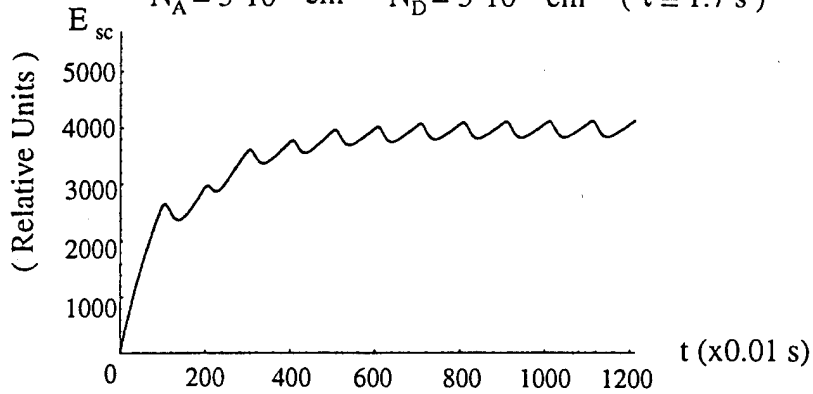
Fig. 5-1

*Note: The response time τ is measured from a curve drawn by connecting
the bottom points on this shown curve.

$N_A = 1.5 \cdot 10^{16}$ cm^{-3} $N_D = 5 \cdot 10^{17}$ cm^{-3} ($\tau \cong 0.5$ s)

Fig. 5-2

$N_A = 5 \cdot 10^{15}$ cm^{-3} $N_D = 5 \cdot 10^{17}$ cm^{-3} ($\tau \cong 0.5$ s)
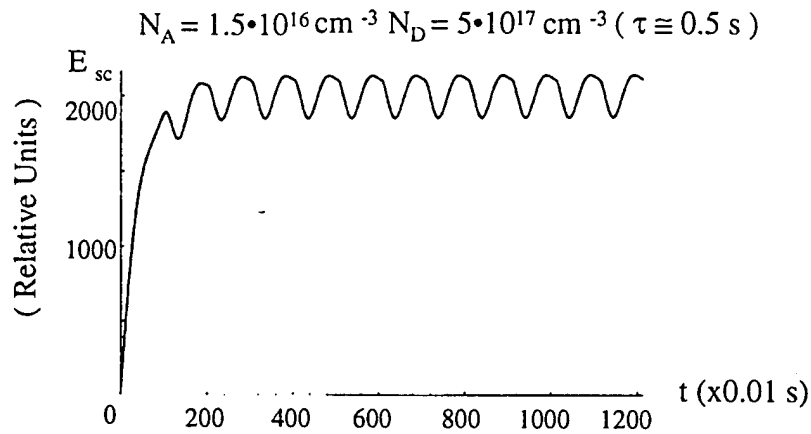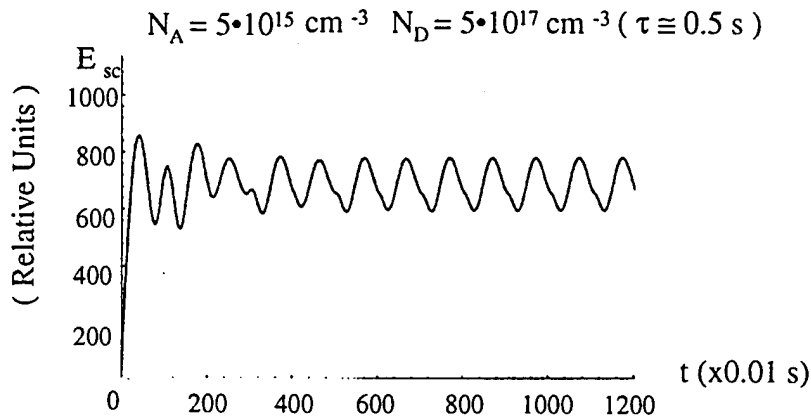
Fig. 5-3

AC field   I = 100 mw/cm^2 kg = 2.4•10^4 1/cm

T = 2 s   f = 0.5 Hz

E$_{sc}$

($\tau \cong 0.5$ s)

Fig. 5-4

E$_{sc}$

T = 0.4 s   f = 2.5 Hz

($\tau \cong 0.4$ s)

Fig. 5-5

68

The numerical solutions for an AC field tell us the following points.

1. <u>General effect of AC field</u>

An applied AC field can give an efficient enhancement on the photorefractive effect in both magnitude and speed. This can be seen by comparing Fig.5-1 (AC field) with Fig.4-1 (no field),or Fig.5-2 (AC field) with Fig.4-3 (no field),or Fig.5-3 (AC field) with Fig.4-5 (no field). Also, by comparing Fig.5-1 (AC field) with Fig.4-2 (DC field), or Fig.5-2 (AC field) with Fig.4-4 (DC field), or Fig.5-3 (AC field) with Fig.4-6 (DC field), we can see that the effect of AC field on enhancing the magnitude and response time of the space-charge field is not as strong as that of DC field, which can be explained physically. From the analytical solution presented in last section, the equilibrium value of the space-charge field with an AC field is given by eq. (5-8), from which we can get
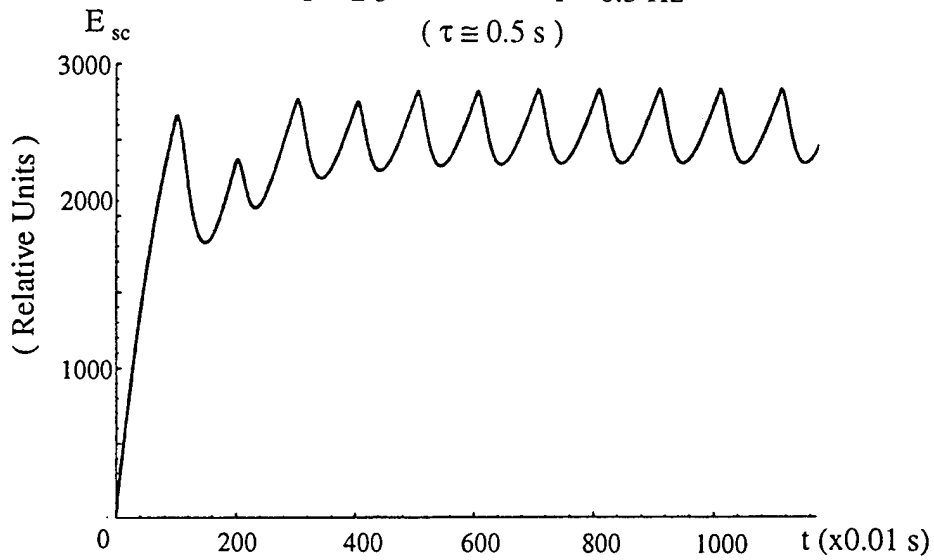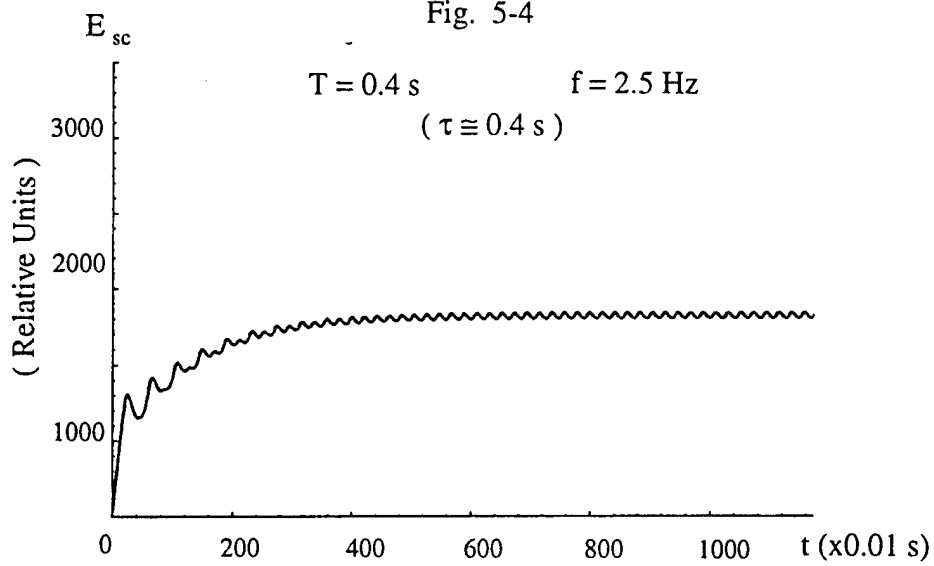
$$\mathrm{Im}E_1^{'eq} = \sin\varphi + 2\cdot[1/(e^{T/2\tau} - e^{-T/2\tau})]\cdot\sin(\omega T/2)\cdot\cos\varphi$$

In this equation, when T increases the equilibrium value of the space-charge field decreases. As stated in last section, when $T\ll\tau$ the space-charge field with an AC field is almost same as that with a DC field. So when T is not very small compared to τ, the space-charge field will be less than the case of $T\ll\tau$. This means that the space-charge field with an AC field having a not very short period is not as strong as that with a DC field. That's why the effect of AC field on enhancing the magnitude of the space-charge field is not as strong as that of DC field. As to the response time, the physical explanations are as follows. During the first half period

69

of an AC field, the temporal behavior of the space-charge field is same as the DC curve. But immediately after the first half period, the space-charge field intends to decrease and an oscillation starts. The oscillation makes the response time with AC field not as fast as that with DC field.

2. Influence of the trap number density

The numerical solutions for different trap number density of the crystal (Fig.5-1, 5-2 and 5-3) tell us that in order to get a stronger enhancement of the photorefractive effect with an applied AC field it is important that a crystal must be doped to have appropriate donor number density and trap number density as in the DC case. In these three figures, the peak performance for the response time is that with N_A value of $1.5 \bullet 10^{16}$ cm^{-3}. The physical reason is same as what we discussed previously in DC field case in Chapter 4.

3. Effect of AC field frequency

All these figures (Fig.5-1 through Fig.5-5) show that the frequency of total space-charger field is twice the frequency of an applied AC field. The numerical results with different frequency of an AC field (Fig.5-4 and 5-5) indicate that an increase of an AC field frequency will cause less modulation in the space-charge field and a faster response time. As stated previously, with an AC field the space-charge field would intend to decrease and start to oscillate immediately after the first half period of the AC field. With a low frequency of AC field the oscillation gets stronger than that with a high frequency. That's why a high AC field frequency causes less

modulation in the space-charge field and a faster response time.

Experimental Setup And Data Analysis For AC Field

The experimental apparatus using an AC field is mostly same as that using a DC field. The AC voltage was produced by using HEWLETT-PACKARD 8002A PULSE GENERATOR, which was then amplified 1000 times using a 610C H.V. SUPPLY AMPLIFIER. The amplified AC high voltage was then connected to the crystal. We investigated the effect of AC field on the photorefractive phenomena through both beam fanning and two beam coupling experiments. The experimental setup is same as in Fig.4-14 (for beam fanning) and Fig.4-15 (for two beam coupling).

Experimental Data

The beam fanning curves are shown in Fig.5-6 through Fig.5-11 for a BSKNN heavily doped crystal, Fig.5-12 through Fig.5-14 for a BSKNN undoped crystal, and Fig.5-15 and Fig.5-16 for a BSKNN undoped crystal using a focused laser beam. The data measured from these figures are listed in table 5-1.

71

Table 5-1 Data of Beam Fanning with AC Field

Sample 1: BSKNN heavily doped

Wavelength: 458 nm (Extraordinary polarization)

Figure No	Magnitude of Field E_0 (kv/cm)	Frequency of Field f (Hz)	Optical Intensity I (mw/cm^2)	Transmission Coefficient* T	Response Time τ (s)
Fig.5-6	0	0	250	3.0%	3.5
Fig.5-7	AC: 3.6	0.33	250	6.4%(top) 3.0%(bottom)	2.7
Fig.5-8	AC: 3.6	25	250	2.6%(top) 1.5%(bottom)	2.6
Fig.5-9	AC: 5.6	0.33	250	5.5%(top) 2.5%(bottom)	2.3
Fig.5-10	AC: 5.6	25	250	2.2%(top) 1.4%(bottom)	2.3
Fig.5-11	AC: 5.6	50	250	2.1%(top) 0.8%(bottom)	2.3

* The transmission coefficient T is defined as a ratio of the

transmitted beam intensity at equilibrium to the initial

intensity of that beam.

Beam Fanning   BSKNN heavily doped   I = 250 mw/cm²

no field   (τ ≅ 3.5 s)

96mv
/div

2s/div
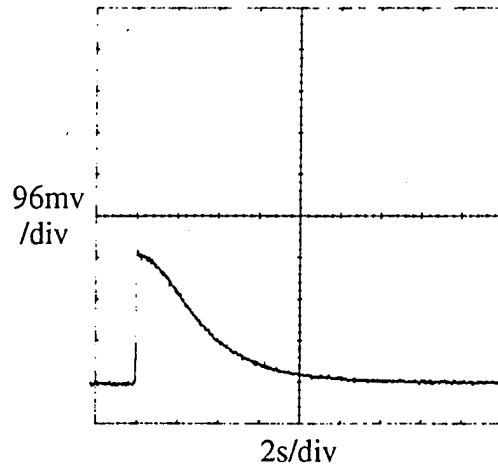
Fig. 5-6

AC field: 3.6 kv/cm   0.33 Hz   (τ ≅ 2.7 s)

100mv
/div

2s/div
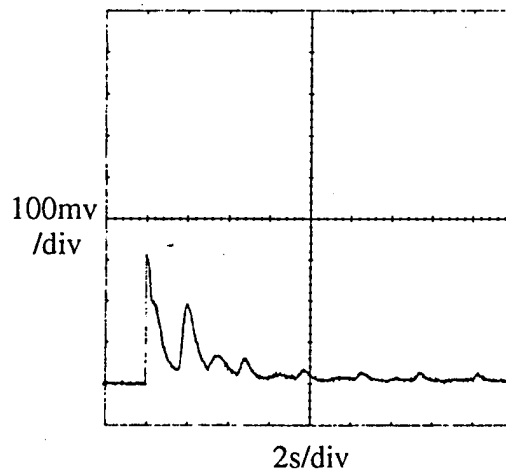
Fig. 5-7

AC field: 3.6 kv/cm   25 Hz   (τ ≅ 2.6 s)

100mv
/div

2s/div

Fig. 5-8

73
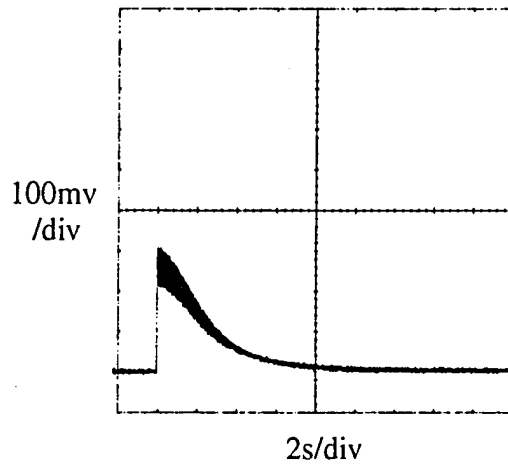
Beam Fanning   BSKNN heavily doped   I = 250 mw/cm²

AC field: 5.6 kv/cm   0.33 Hz   ($\tau \cong 2.3$ s)

100mv
/div

2s/div
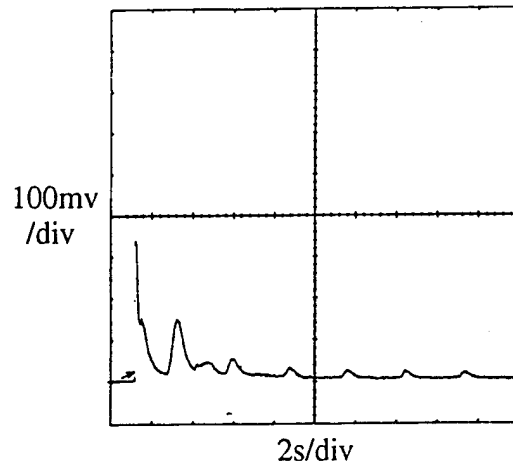
Fig. 5-9

AC field: 5.6 kv/cm   25 Hz   ($\tau \cong 2.3$ s)
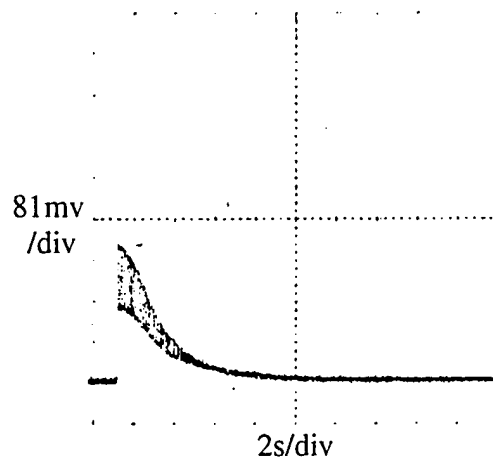
81mv
/div

2s/div

Fig. 5-10

AC field: 5.6 kv/cm   50 Hz   ($\tau \cong 2.3$ s)

100mv
/div

2s/div
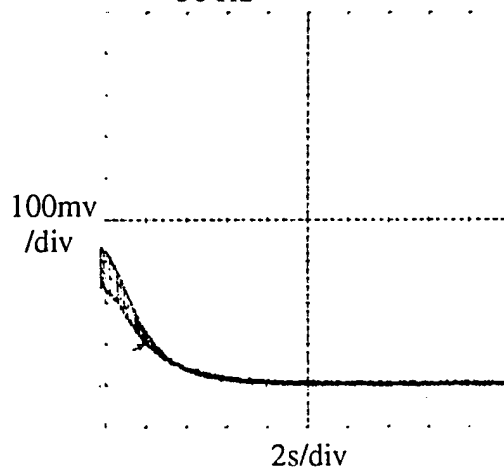
Fig. 5-11

By comparing Fig.5-6 (no field) with Fig.5-7 through Fig.5-11 (AC field) we see that the photorefractive effect in both magnitude and speed is enhanced by applying an AC field. But from comparing Fig.5-7 and Fig.5-8 (AC field) with Fig.4-17 (DC field), or Fig.5-9 through Fig.5-11 (AC field) with Fig.4-18 (DC field), it shows that the effect of AC field on enhancing the magnitude and speed of the photorefractive effect is not as strong as that of DC Field. A detailed comparison of Fig.5-7 (AC field of 3.6 kv/cm) with Fig.4-17 (DC field of 3.6 kv/cm), Fig.5-9 (AC field of 5.6 kv/cm) with Fig.4-18 (DC field of 5.6 kv/cm) showed that the fanning signal in the first half period of AC field was almost same as DC figure, but after that an oscillation happened in the fanning signal with AC field. The oscillation then made the response time longer than that of DC field case.

By comparing Fig.5-7 and Fig.5-8 (AC field of 3.6 kv/cm) with Fig.5-9 through Fig.5-11 (AC field of 5.6 kv/cm), it can be seen that an increase of AC field amplitude will cause a stronger enhancement of the photorefractive effect in both magnitude and speed. Fig.5-9 (or Fig.5-10) with AC field of 5.6 kv/cm showed a stronger beam fanning signal and less response time than Fig.5-7 (or Fig.5-8) with AC field of 3.6 kv/cm.

By comparing Fig.5-7 (AC field of 0.33 Hz) with Fig.5-8 (AC field of 25 Hz), or Fig.5-9 (AC field of 0.33 Hz), Fig.5-10 (AC field of 25 Hz) and Fig.5-11 (AC field of 50 Hz) with each other, it can be found that an increase of AC field frequency will reduce the modulation of oscillation in signal.

All these experimental results are in general agreement with the numerical solutions presented in last section (Section II of this chapter). Another beam fanning

experiment was performed for the undoped BSKNN sample. The measurement results are shown in Fig.5-12 through Fig.5-14 for beam unfocused, and Fig.5-15 and Fig.5-16 for beam focused. The data measured from these figures are listed in table 5-2.

Table 5-2 Data of Beam Fanning with AC Field

Sample 2: BSKNN undoped

Wavelength: 458 nm (Extraordinary polarization)

Figure No	Magnitude of Field E_0 (kv/cm)	Frequency of Field f (Hz)	Optical Intensity I (mw/cm^2)	Transmission Coefficient* T	Response Time τ (s)
Fig.5-12	0	0	160	90.0%	5.6
Fig.5-13	AC: 4.0	0.4	160	39.1%(top) 17.5%(bottom)	4.0
Fig.5-14	AC: 4.0	20	160	83.2%(top) 79.8%(bottom)	3.8

The following figures are for beam fanning with focusing.

Figure No	Magnitude of Field E_0 (kv/cm)	Frequency of Field f (Hz)	Optical Intensity I (mw/cm^2)	Transmission Coefficient* T	Response Time τ (s)
Fig.5-15	0	0	640	90.0%	1.1
Fig.5-16	AC: 4.0	1.2	640	60.7%(top) 41.8%(bottom)	1.0

* The transmission coefficient T is defined as a ratio of the transmitted beam intensity at equilibrium to the initial intensity of that beam.

Beam Fanning   BSKNN undoped $I = 160$ mw/cm^2

no field   ($\tau \cong 5.6$ s)

50mv
/div

2s/div
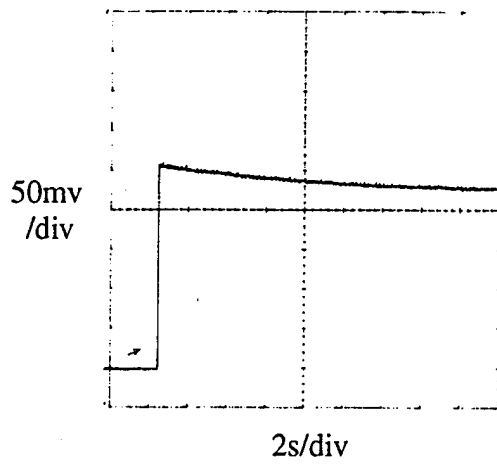
Fig. 5-12

AC field: 4 kv/cm   0.4 Hz   ($\tau \cong 4.0$ s)

50mv
/div

2s/div
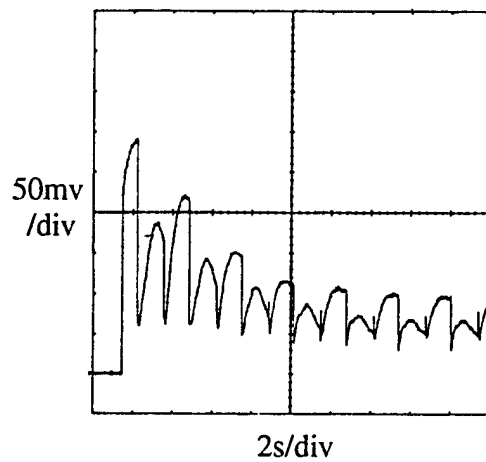
Fig. 5-13

AC field: 4 kv/cm   20 Hz   ($\tau \cong 3.8$ s)

59mv
/div

2s/div
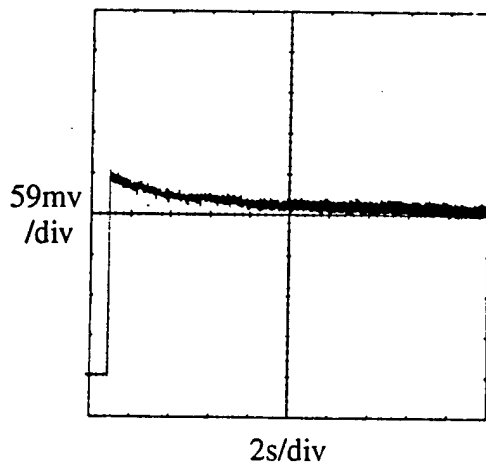
Fig. 5-14

Beam Fanning with Focusing

BSKNN undoped $I = 640$ mw/cm^2

no field   ($\tau \cong 1.1$ s)

50mv
/div

2s/div
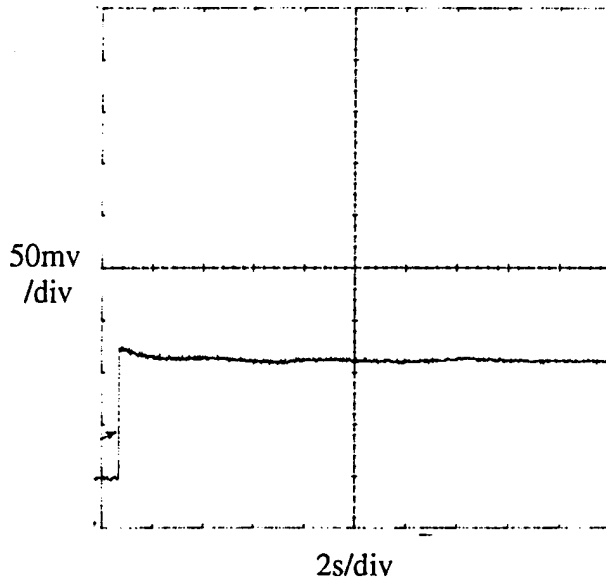
Fig. 5-15

AC field: 4-kv/cm   1.2 Hz   ($\tau \cong 1.0$ s)

50mv
/div

1s/div
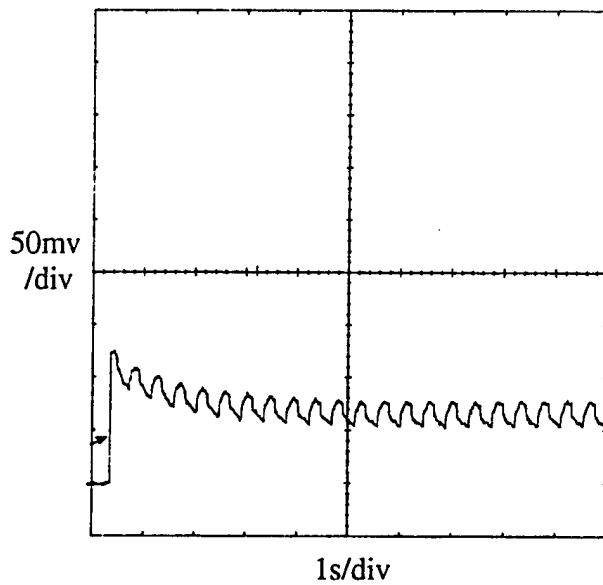
Fig. 5-16

By comparing Fig.5-12 (no field) with Fig.5-13 and Fig.5-14 (AC field), or Fig.5-15 (no field) with Fig.5-16 (AC field), it can be seen that an applied AC field really enhance the photorefractive effect in both magnitude and speed.

By comparing Fig.5-13 and Fig.5-14 (AC field) with Fig.4-20 (DC field), or Fig.5-16 (AC field and focusing) with Fig.4-22 (DC field and focusing), we see that although the effect of AC field on enhancing the photorefractive effect is not as strong as that of DC field, but with an applied AC field the field screening is avoided, which happens in the case of DC field shown in Fig.4-20 and Fig.4-22. Let's compare Fig.5-16 (AC field of 4 kv/cm) with Fig.4-22 (DC field of 4 kv/cm). In Fig.5-16 the beam fanning signal during the first half period of AC field is almost the same as DC figure shown in Fig.4-22. Then, in Fig.4-22 the signal keeps going down, but in Fig.5-16 after the first half period the signal goes up and an oscillation happens. Due to the oscillation the response time gets longer in AC field case than that in DC field case. That's why the effect of AC field on enhancing the photorefractive effect is not as strong as that of DC field.

In Fig.5-13 we see that the frequency of the beam fanning signal is twice the frequency of an applied AC field, which is in agreement with the theoretical prediction in last section.

From comparing Fig.5-13 and Fig.5-14 (beam unfocused) with Fig.5-16 (beam focused), it can be seen that on the use of AC field, if laser beam is focused, the response time can be further decreased.

For the BSKNN undoped crystal, the experimental results of two beam coupling are shown in Fig.5-17 and Fig.5-18 for the case of beam unfocused, and Fig.5-19 through Fig. 5-24 for the case of beam focused. The data measured from Fig.5-17 and Fig.5-18 are listed in table 5-3, and data from Fig.5-19 through Fig.5-24 are in table 5-4.

Table 5-3 Data of Two Beam Coupling with AC Field

Sample 2: BSKNN undoped

Wavelength: 458 nm (Extraordinary polarization)

Full Crossing Angle: $2\theta=10°$

Figure No	Magnitude of Field E_0 (kv/cm)	Frequency of Field f (Hz)	Intensity of Weak Beam I_1 (mw/cm^2)	Intensity of strong Beam I_2 (mw/cm^2)	m	Relative Energy Exchange** $\Delta I_1/I_1$	Response Time τ (s)	Modulation*
Fig.5-17	0	0	0.6	64	0.2	0.1	9.0	
Fig.5-18	AC: 3.6	1.2	0.6	64	0.2	0.9	6.5	0.35

$$m =2(I_1 I_2)^{1/2}/ (I_1+I_2)$$

* The modulation is defined as a ratio of the oscillation amplitude to the signal magnitude.   ** The relative energy exchange is defined as a ratio of the intensity gain to the original intensity.

Two - beam coupling   BSKNN undoped   Full crossing angle: 10°

no field   Total I = 64 mw/cm^2 ($\tau \cong 9.0$ s)

75mv
/div
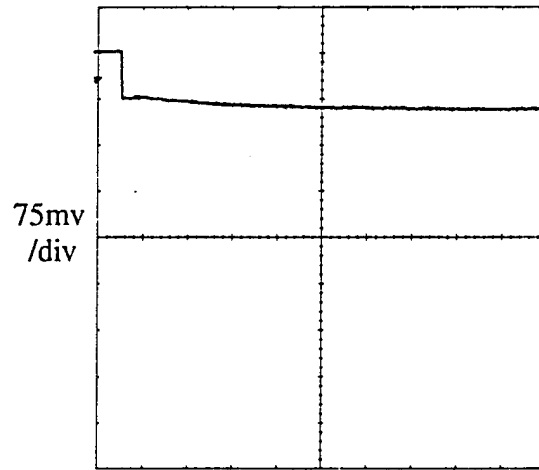
5s/div

Fig. 5-17

Two - beam coupling   BSKNN undoped   Full crossing angle: 10°

AC field: 3.6 kv/cm   1.2 Hz   Total   I = 64 mw/cm^2 ($\tau \cong 6.5$ s)

65.5mv
/div

5s/div

Fig. 5-18

81
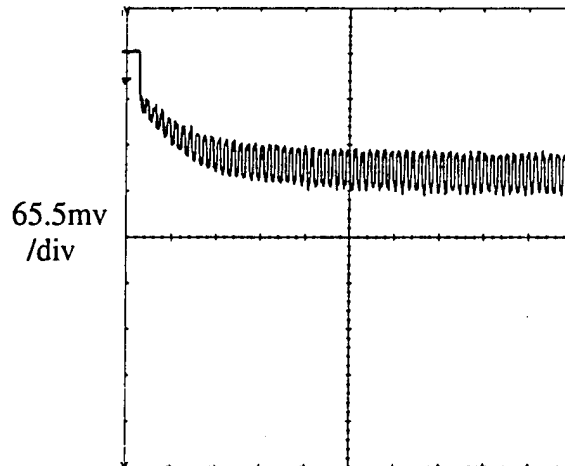
Table 5-4 Data of Two Focused Beam Coupling with AC Field

Sample 2: BSKNN undoped

Wavelength: 458 nm (Extraordinary polarization)

Full Crossing Angle: $2\theta=10°$

(Focal Length of the Lens: 100 cm)

Figure No	Magnitude of Field E_0 (kv/cm)	Frequency of Field f (Hz)	Intensity of Weak Beam I_1 (mw/cm^2)	Intensity of strong Beam I_2 (mw/cm^2)	m	Relative Energy Exchange** $\Delta I_1/I_1$	Response Time τ (s)	Modulation*
Fig.5-19	0	0	2.6	260	0.2	0.1	4.0	
Fig.5-20	AC: 3.6	1.2	2.6	260	0.2	1.3	1.7	0.42
Fig.5-21	AC: 3.6	1.2	2.6	410	0.16	0.9	1.26	1.1
Fig.5-22	AC: 3.6	1.8	2.6	410	0.16	1.2	0.88	0.55
Fig.5-23	0	0	26	2600	0.2	0.3	0.9	
Fig.5-24	AC: 3.6	3.2	26	2600	0.2	1.7	0.3	0.7

$$m =2(I_1 I_2)^{1/2}/ (I_1+I_2)$$

* The modulation is defined as a ratio of the oscillation amplitude to the

signal magnitude.

** The relative energy exchange is defined as a ratio of the intensity gain to

the original intensity.

Two focused beam coupling   BSKNN undoped   Full crossing angle: 10°

Total $I = 260$ mw/cm^2 no field   ($\tau \cong 4.0$ s)

75mv
/div
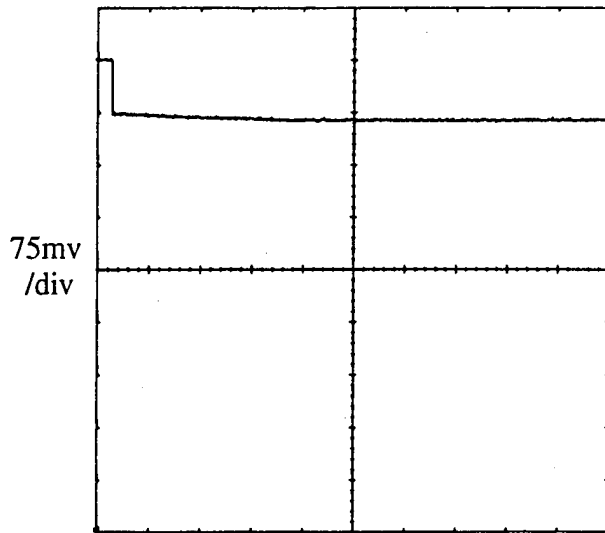
1s/div

Fig. 5-19

Total $I = 260$ mw/cm^2 AC field: 3.6 kv/cm   1.2 Hz   ($\tau \cong 1.7$ s)

75mv
/div
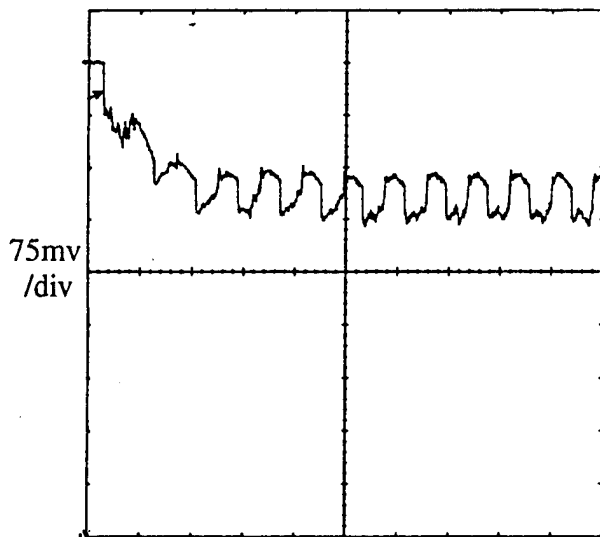
1s/div

Fig. 5-20

Two focused beam coupling   BSKNN undoped   Full crossing angle: $10°$

Total I = 410 mw/cm^2 AC field: 3.6 kv/cm   1.2 Hz   ($\tau \cong 1.26$ s)

75mv
/div

1s/div
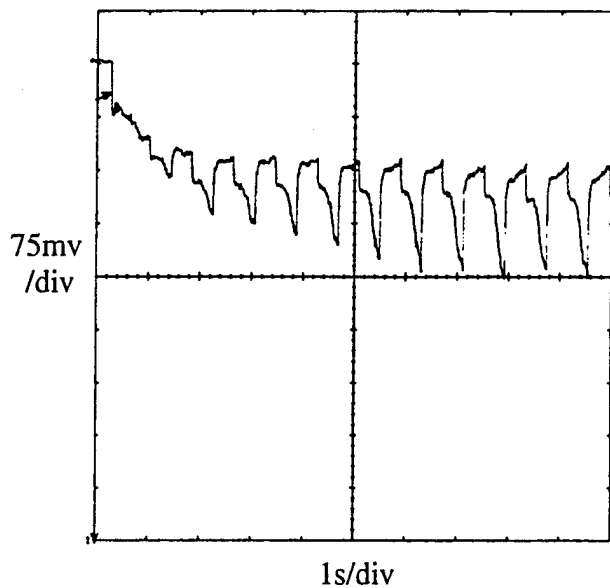
Fig. 5-21

Total I = 410 mw/cm^2 AC field: 3.6 kv/cm   1.8 Hz   ($\tau \cong 0.88$ s)

65mv
/div

1s/div
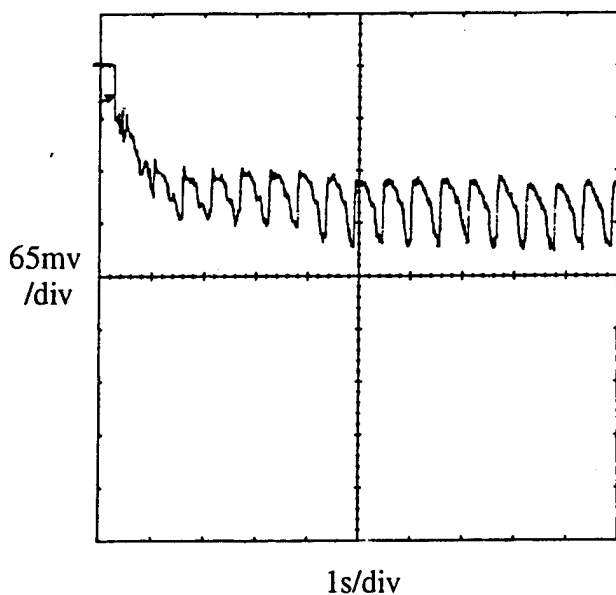
Fig. 5-22

Two focused beam coupling   BSKNN undoped   Full crossing angle: 10°
Total I = 2.6 w/cm^2 no field   ($\tau \cong 0.9$ s)

40mv
/div

500ms/div
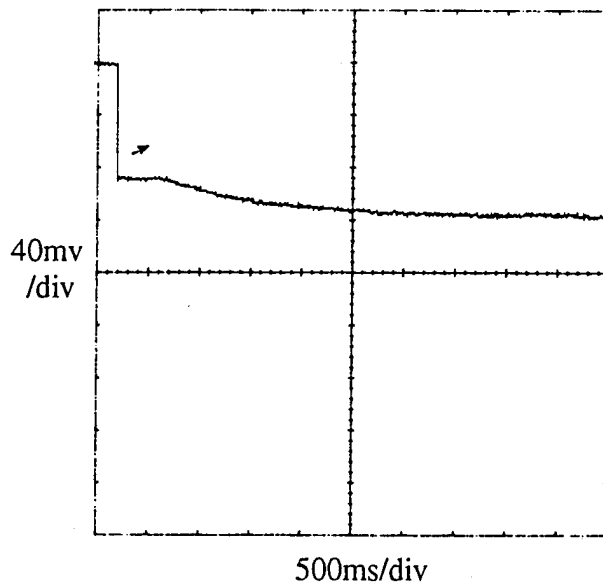
Fig. 5-23

AC field: 3.6 kv/cm   3.2 Hz   ($\tau \cong 0.3$ s)

75mv
/div

500 ms/div

Fig. 5-24

85
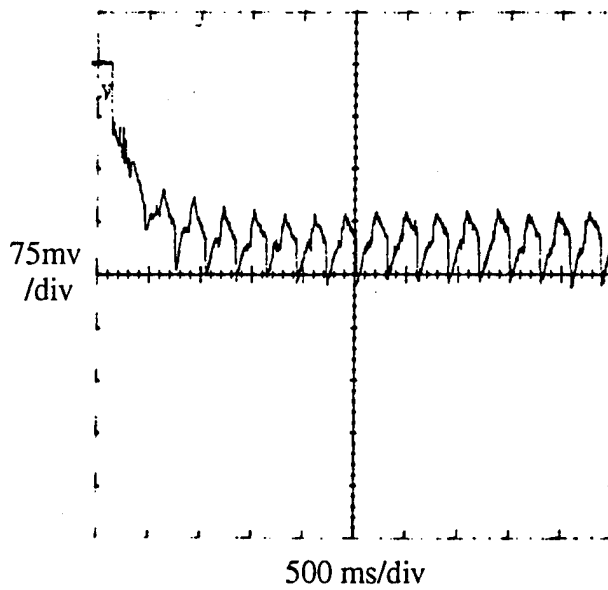
By comparing Fig.5-18 (AC field) with Fig.5-17 (no field), or Fig.5-20 (AC field) with Fig.5-19 (no field), or Fig.5-24 (AC field) with Fig.5-23 (no field), we see that an AC field enhances the photorefractive effect in both the magnitude and speed. Fig.5-17, Fig.5-19 and Fig.5-23 show almost no or very little energy exchange between two beams. But with applying an AC field, Fig.5-18, Fig.5-20 and Fig.5-24 show an obvious energy exchange between two beams and also a decrease of the response time compared with the no field case.

By comparing Fig.5-18 (AC field, τ=6.5 s) with Fig.4-25 (DC field, τ=5.0 s), or Fig.5-20 (AC field, τ=1.7 s) with Fig.4-27 (DC field, τ=1.7 s), or Fig.5-24 (AC field , τ=0.3 s) with Fig.4-29 (DC field, τ=0.2 s), we see that the effect of AC field on enhancing the photorefractive response time is not as strong as that of DC field, but two results are very close. Also, the advantage of using AC field is that with the use of AC field a field screening is avoided, which can be seen from comparing Fig.5-18 (AC field) with Fig.4-25 (DC field).

By comparing Fig.5-21 (AC field of 1.2 Hz) with Fig.5-22 (AC field of 1.8 Hz), we see that an increase of AC field frequency can reduce the response time and enhance the energy exchange between two beams.

By comparing Fig.5-20, Fig.5-21, Fig.5-22 and Fig.5-24 (AC field and beam focused) with Fig.5-18 (AC field and beam unfocused), we find that if the laser beams are focused the response time can be further reduced. The results show that focusing increases the speed of response and that the applied AC field makes possible strong coupling simultaneously.

Direct Comparison Of Experiment With Theory

By using the same way and same parameters as in Section IV of Chapter 4, we can obtain the gain coefficient for AC field case from both the experimental and numerical data. The results are shown in Fig.5-25 and 5-26, which are based on the experimental data of Fig.5-24. Two curves give almost the same energy gain and same response time.

Two focused beam coupling

BSKNN undoped

Full crossing angle: 10°

AC field: 3.6 kv/cm, 3.2 Hz

Total I = 2.6 w/cm^2

($\tau = 0.34$ s)
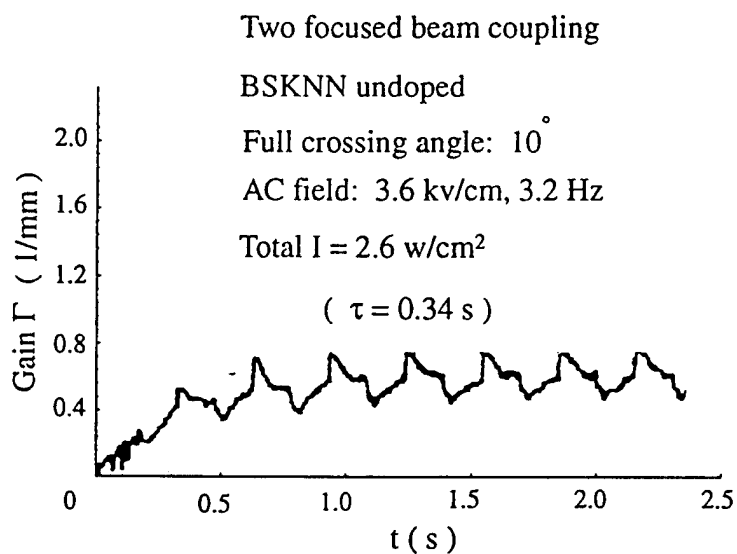
Fig. 5-25 Experimental curve

($\tau = 0.33$ s)
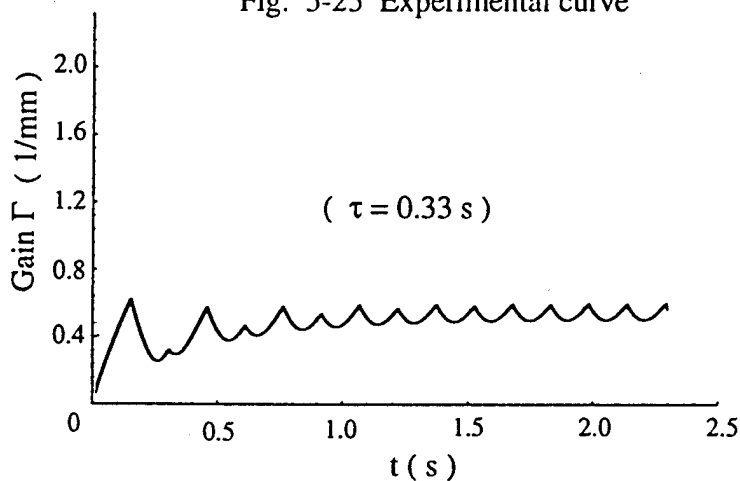
Fig. 5-26 Theoretical curve

Conclusions

Both theory and experiment demonstrate that the application of an A.C. electric field can be used to enhance both the speed and magnitude of the photorefractive effect without the draw back of the screening phenomena observed using a D.C. electric field. Our experiments were carried out using BSIKNN as opposed to SBN or BaTiO$_3$ due to the higher depoling field of BSKNN. Our initial experiments using SBN were not successful after about 1kv/cm. However, for BSKNN it was possible to apply fields up to 6kv/cm without significant depoling. It would be interesting to find additional materials with higher depoling fields since they would allow even higher applied A.C. electric fields and furancement.

The clear result in this investigation is that a focused laser beam into a BSKNN sample enhanced the response time. Our experiments show that for an incident beam 5cm x 5cm in size the use of a spherical focusing lens to focus to a 50 micron beam diameter would increase the intensity by six orders of magnitude in the crystal and reduce the response factor. Since this is much greater than the four orders of magnitude required this technique can act as an effective limiter.

VI. DETERMINATION OF TRAP NUMBER DENSITY

One of the by-products of our investigation using applied D.C. electric fields has been of a new technique to determine the trap number density in photorefractive materials. Our technique is based on the energy exchange between two laser beams in a two-beam coupling experiment.

Two laser beams intersect inside a crystal and write an interference pattern. Then due to the charge migration, a change of the refractive index is caused and an index grating is produced in the crystal, which is shifted in phase with the intensity pattern. The phase shift between the grating and the fringe pattern, thus, causes an energy exchange between two beams.

In a two beam coupling experiment we can measure the energy exchange signal between two beams, I_ε and the diffraction signal due to the grating, I_d (Ref. [1]). The energy exchange signal is the intensity change of the detected beam after two beams are turned on, and the diffraction signal is the intensity measured immediately after the detected beam blocked. If two beams have equal intensity of I_0 and the crossing angle between two beams are small, I_ε and I_d must be much less than I_0. Then the phase shift ϕ between the grating and the fringe pattern can be determined by the following equation . (Se Appendix III).

$$\sin \phi = I_\varepsilon / [2(I_0 I_d)^{1/2}] \qquad (6\text{-}1)$$

Energy Transfer Measurement And Determination Of The Phase Shift Betwen The Grating And The Fringe Pattern

The experimental set up for two beam coupling is shown in Fig. 6-1.
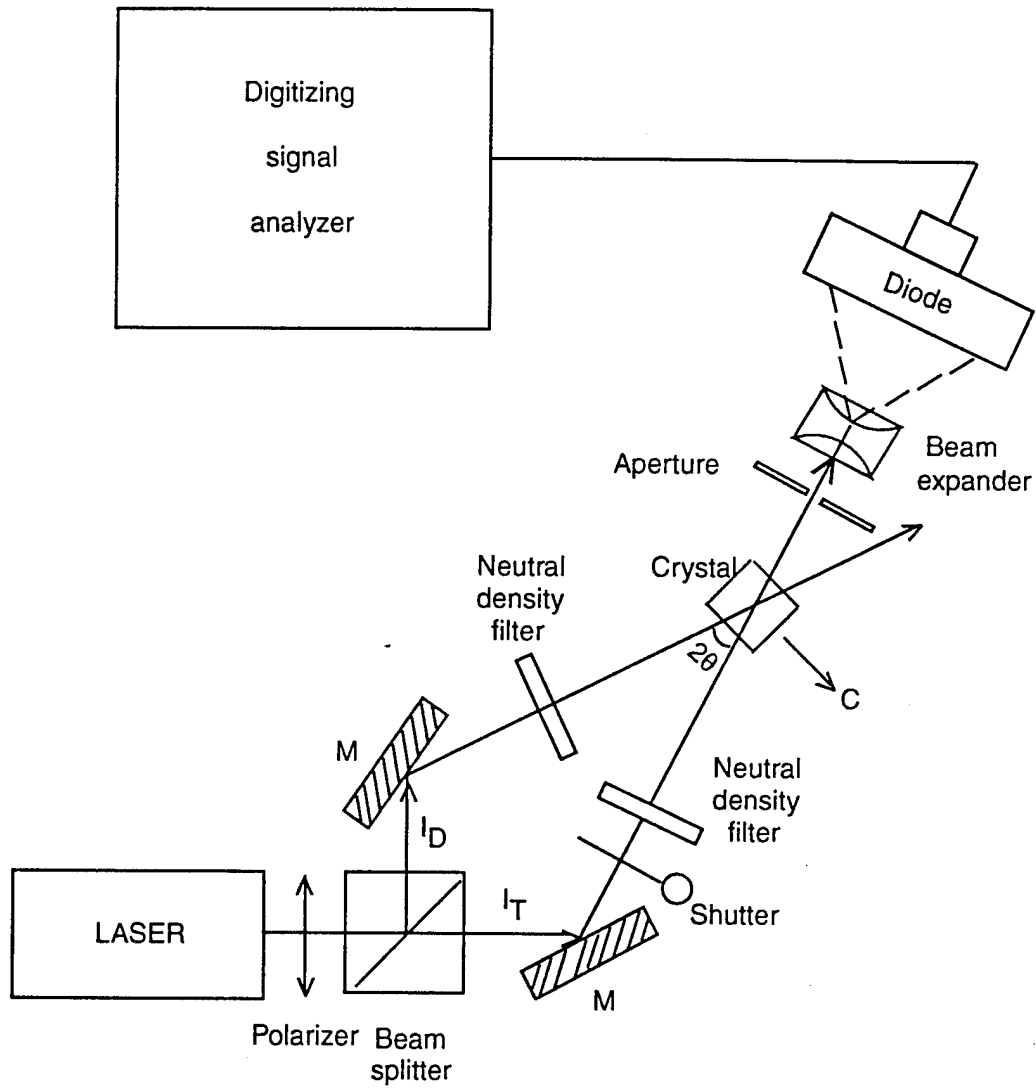
Fig. 6-1 Experimental setup for measuring phase-shift

The He-Ne laser (5 mw of power and $\lambda = 632.8$ nm) was ordinary polarized in order to minimize beam fanning and resulting fluctuations in the two beam coupling signals. After the polarizer the laser beam was split into two beams I_T and I_D that intersect inside a thin sample of SBN 60 with 0.015% Cesium as a dopant (static dielectric constant $\epsilon' = 950$) such that the grating vector is parallel to the c-axis. The beam splitter is 50% to 50% to make the beam I_T having the same intensity as I_D. The angle 2θ between the two beams was 22°. The beam $I_T(d)$ was detected with a photodiode. For all our observed intensity values the photodiode was linear. To avoid the observation of multi-exponential growth and decay times, the detected beam was expanded with a beam expander so that only the uniform portion of the beam was detected by the photodiode. The output of the diode was fed into the 602A Digitizing Signal Analyzer. After turning on both beams a growth curve was recorded and the energy exchange signal I_ϵ was measured. When the grating reached its steady state we blocked the detected beam. The transmitted beam immediately went to zero, and the diffraction signal I_d was detected. Finally, the intensity of the transmitted beam I_0 was measured. By substituting I_0, I_ϵ and I_d into Equation (6-1), we can calculate the phase shift between the grating and the interference pattern in the crystal.

III. Determination Of Trap Number Density By Phase Shift Measurement And Field Dependence Of Dielectric Constant And Electro-Optic Coefficient

As discussed in chapter 4 and 5, a trap number density N_A of a crystal plays a key role in the photorefractive response time. Therefore, measuring N_A accurately becomes an important topic in the research on photorefractive phenomena. In this section we will present a new technique for the measurement of N_A by applying a DC field across a crystal and determining the resulted phase shift between the grating and the fringe pattern.

After applying a DC field across a crystal we carried out the measurement described in the last section yielding values for I_0, I_ϵ and I_d. By substituting them into Eq. (6-1) we calculated both the sin ϕ and the tan ϕ. In order to get accurate results we varied the magnitude of DC field and measured I_0, I_ϵ and I_d for each DC field value E_0. The data for different E_0 and the calculated sin ϕ, tan ϕ are listed in Table 6-1.

From the band transport theory we have

$$\tan \phi = \frac{E_D}{E_0} + (\frac{E_D^2}{E_0} + E_0) \frac{1}{Eq} \qquad (6\text{-}2)$$

$$\frac{1}{Eq} = (\tan \phi - \frac{E_D}{E_0}) \bigg/ (\frac{E_D^2}{E_0} + E_0) \qquad (6\text{-}3)$$

Expression (6-2) gives a value of E_0 for minimum ϕ of $E_0 = [E_D E_q + E_D^2]^{1/2}$. Using eq. (6-3) we are able to calculate a set of data of $1/E_q$ vs E_0. E_q is defined as

$$E_q = 4\pi e N_{eff} \big/ \in K_g$$

where $\quad (N_{eff} = \frac{N_A}{1 + N_A / (N_D^- N_A)})$

92

Table 6-1 Relation Between the Applied DC

Field and the Resulted Phase Shift

E_0 (v/cm)	$\tan\varphi$	$\sin\varphi$
0.0	25.4680	0.9992
277.78	5.48783	0.9838
555.56	3.21020	0.9548
833.33	2.66599	0.9363
1111.11	2.46498	0.9267
1388.89	2.26533	0.9148
1666.67	2.41280	0.9238
1944.44	2.53525	0.9303
2222.22	2.71445	0.9386
2511.11	2.72540	0.9388

If E_q depends on E_0, so the dielectric constant $\in$ must depend on E_0. For the parameters used in our experiment we found

$$K_g = \frac{2\pi}{\lambda}\,(2\sin\theta) = 3.79 \times 10^4\ cm^{-1}$$

$$E_D = \frac{K_B T K_g}{e} = 963.24\ {}^v\!/_{cm}$$

$$E_q = \frac{4\pi e}{K_g}\,(\frac{N_{eff}}{\in}) = (4.776 \times 10^{-11})\,(\frac{N_{eff}}{\in}) \qquad (6\text{-}4)$$

We assume that the dependence of the dielectric constant $\in$ on the magnitude of DC field E_0 has a form of

$$\in (E_0) = \in ' (1 + \alpha E_0 + \beta E_0^2)$$

$$= \in ' [1 + f (E_0)] \qquad\qquad (6\text{-}5)$$

where α and β are constants to be determined.

By combining Eqs (6-3), (6-4) and (6-5) we can calculate $1 / E_q$ and $N_{eff} / \in '$ for each value of DC field E_0. The results are listed in Table 6-2.

Table 6-2

i	$(E_0)_i$	$(1/E_q)_i$	$(1/E_q)_i/(1/E_q)_1 =$	$N_{eff}/\in '$
	(v/cm)	($\times 10^{-4}$cm/v)	$\{1+f[(E_0)_i]\}/\{1+f[(E_0)_1]\}$	($\times 10^{13}$cm^{-3})
1	277.78	5.5838	1.0000	4.71
2	555.56	6.6335	1.1880	4.53
3	833.33	7.7571	1.3892	4.30
4	1111.11	8.2114	1.4706	4.37
5	1388.89	7.6419	1.3685	4.92
6	1666.67	8.2526	1.4779	4.66
7	1944.44	8.4236	1.5086	4.57
8	2222.22	8.6410	1.5475	4.37
9	2511.11	8.1296	1.4559	4.44

Based on the data in Table 6-2 we plotted $\{ 1 + f [(E_0)_i] \} / \{ 1 + f [(E_0)_1] \}$

versus $(E_0)_i$ which is shown in Fig 6-2. By fitting the data we found that

$\alpha = 0.0009515$ and $\beta = -2.51 \times 10^{-7}$.
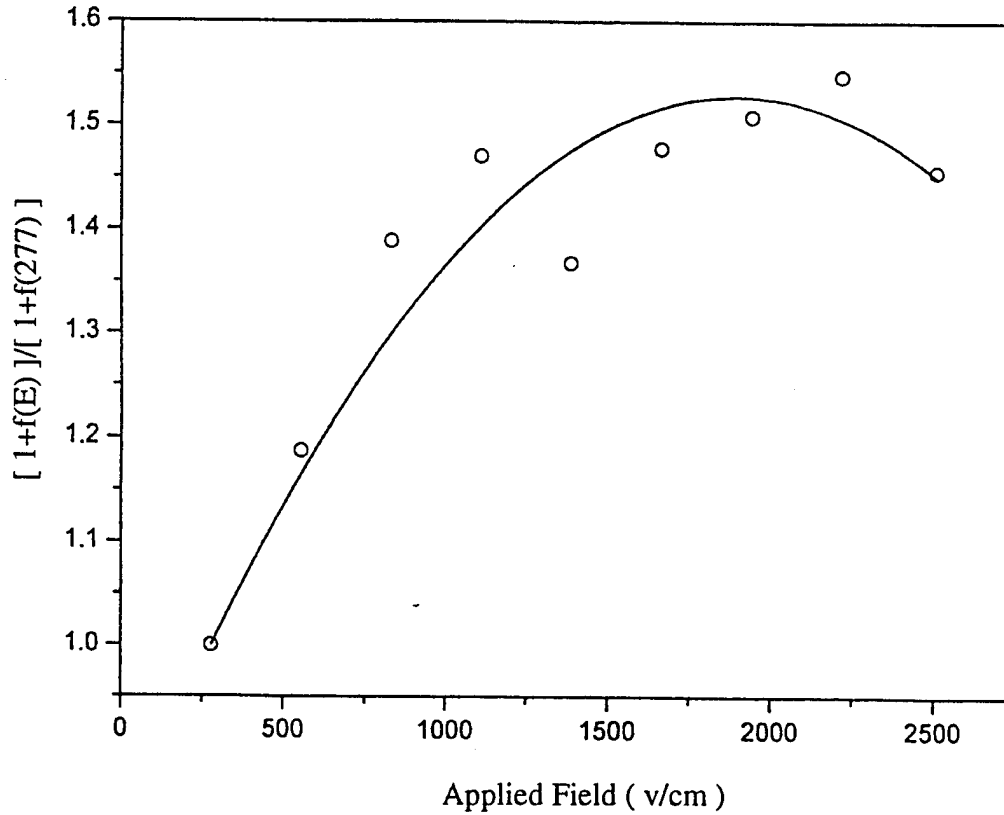
Fig. 6-2

As a function of an applied DC field, the dielectric constant ϵ has a form of

$$\epsilon (E_0) = \epsilon' [1 + 0.0009515 E_0 - 2.51 \times 10^{-7} E_0^2]$$

Then $E_q = \dfrac{4.776 \cdot 10^{-11}}{1 + 0.0009515 E_0 - (2.51 \cdot 10^{-7}) E_0^2} \left(\dfrac{N_{eff}}{\epsilon'} \right)$

For each pair of E_0 and E_q we calculated the value of N_{eff} / ϵ', which is listed in the

middle column of Table 6-3.

95

Table 6-3 Full crossing angle: 22°

Applied DC field E_0 (v/cm)	$N_{eff}/\in'$ ($\times 10^{13}cm^{-3}$)	N_{eff} ($\times 10^{16}cm^{-3}$)
277.78	4.71	4.47
555.56	4.53	4.30
833.33	4.30	4.09
1111.11	4.37	4.15
1388.89	4.92	4.67
1666.67	4.66	4.43
1944.44	4.57	4.34
2222.22	4.37	4.15
2511.11	4.44	4.22

* The above listed results are based on the dielectric constant $\in$ being $\in$ =

$\in'$ ($1 + 9.2 \cdot 10^{-4} E_0 - 2.51 \cdot 10^{-7} E_0^2$), where $\in'$ is 950 for our crystal.

By taking the average, we obtained

$N_{eff}/\in' = (4.54 \pm 0.38) \times 10^{13}$ (cm^{-3}).

For our crystal $\in'$ is 950. Therefore, we get $N_{eff} = (4.31 \pm 0.36) \times 10^{16}$ (cm^{-3}).

N_{eff} is approximately the trap density N_A for our crystal. So we can get

$N_A = (4.31 \pm 0.36) \times 10^{16}$ (cm^{-3}). In Ref.[3] N_A value of (4.2 ± 0.2) $\times 10^{16}$ (cm^{-3}

) was reported for a crystal of SBN:60 with 0.015% Rh. concentration. Our results

are very closer to theirs. We plotted curves of sin φ vs E_0, tan φ vs E_0 and $\in$ vs E_0, respectively. They are shown in Fig 6-3, 6-4 and 6-5.

Fig. 6-3

Fig. 6-4

Fig. 6-5

97
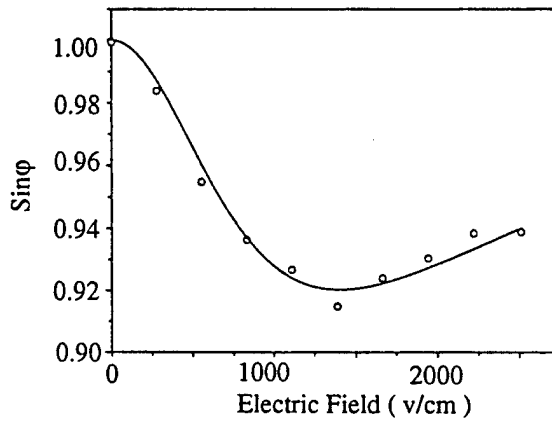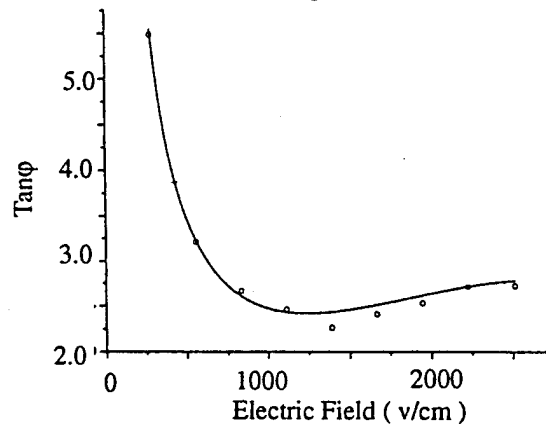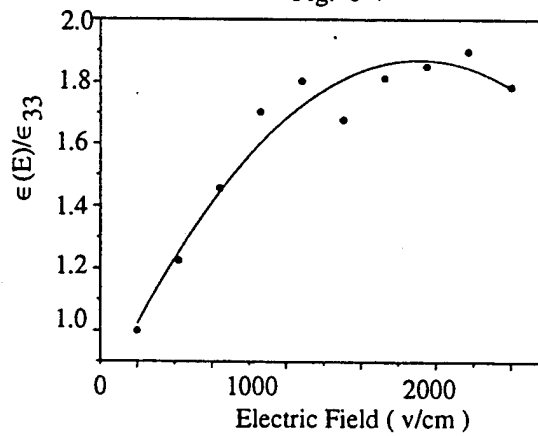
Beside the information of the electric field dependence of the dielectric constant which we obtained from this experiment, from the measurement of diffraction signal we are also able to determine the electric field dependence of the electro-optic coefficient. The diffraction efficiency η is given by (Ref. [1], [2])

$$\eta = \sin^2(\kappa d)$$

where $\kappa = \pi \cdot \Delta n / \lambda \cos\theta$ and $\Delta n = (1/2) n_0^3 r_{eff} E_{sc} \cdot m$.

From the above equation we can get an expression for electro-optic coefficient r_{eff} which is

$$r_{eff} = \left(\frac{\sin^{-1}\sqrt{\eta}}{E_{sc}}\right) \left(\frac{2 \lambda \cos\theta}{\pi n_0^3 dm}\right)$$

As we applied a DC field E_0 across a crystal, the diffraction signal η and the space-charge field E_{sc} will change with E_0 but keep all other parameters unchanged. Therefore, by calculating η and E_{sc} we are able to determine the dependance of electro-optic coefficient r_{eff} on the applied DC field E_0. Since the laser beams are in ordinary polarization, the effective electro-optic coefficient r_{eff} in our measurement is equal to r_{13}. For the parameters of $\lambda = 633$ nm, $\theta = 11°$, $n_0 = 2.3$, $m = 1$ and $d = 1.5$ mm, we got $r_{13} = 48.5$ pm/v with no applied field. Then with an applied field, the diffraction efficiency and related calculation results are listed in Table 6-4. We plotted electro-optic coefficient versus electric field and fitted the data, which is shown in Fig. 6-6.

The fitting results gave us

Table 6-4 Electric Field Dependence of the Electro-Optic Coefficient

E_0 (v/cm)	η ($\times 10^{-3}$)	$Sin^{-1}(\eta^{1/2})$ ($\times 10^{-2}$)	E_{sc}(v/cm)	r_{eff}
0	7.31	8.56	667	r_{13}
278	7.90	8.90	641	1.08 r_{13}
556	8.62	9.29	661	1.10 r_{13}
833	9.61	9.81	684	1.12 r_{13}
1111	9.82	9.92	731	1.06 r_{13}
1389	10.24	10.13	830	0.95 r_{13}
1667	10.32	10.17	851	0.93 r_{13}
1944	10.75	10.38	888	0.91 r_{13}
2222	10.85	10.43	912	0.89 r_{13}
2511	11.68	10.82	933	0.88 r_{13}
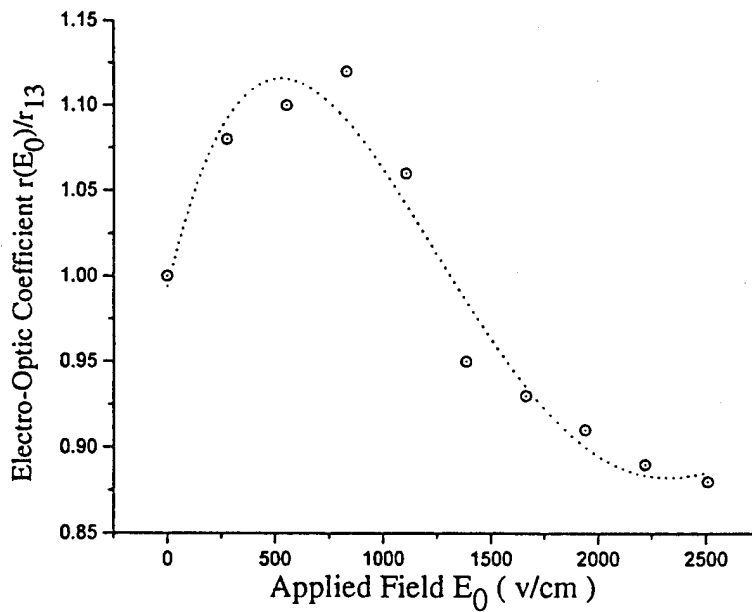
Fig. 6-6

$$r(E_0) / r_{13} = 0.99308 + (5.282 \cdot 10^{-4}) E_0 - (6.935 \cdot 10^{-7}) E_0^2 +$$

$$(2.682 \cdot 10^{-10}) E_0^3 - (3.289 \cdot 10^{-14}) E_0^4$$

For our SBN:60 crystal, the effective electro-optic coefficient R_{eff} is given by

$R_{eff} = n_e^4 r_{33} \cos^2\theta - n_0^4 r_{13} \sin^2\theta$ for extraordinary rays and $R_{eff} = n_o^4 r_{13}$ for ordinary

rays. Experimentally we measured the gain coefficient of the weak beam with an

ordinary polarization and an extraordinary polarization, respectively. Then by

calculating the ratio of two gains, we can get the ratio of r_{33} to r_{13}. From our

measurement the ratio of r_{33} to r_{13} is 3.21 for our crystal.

Experimentally, we also measured the electro-optic coefficient by an optical

interference experiment. The experimental set up is shown in Fig. 6-7.
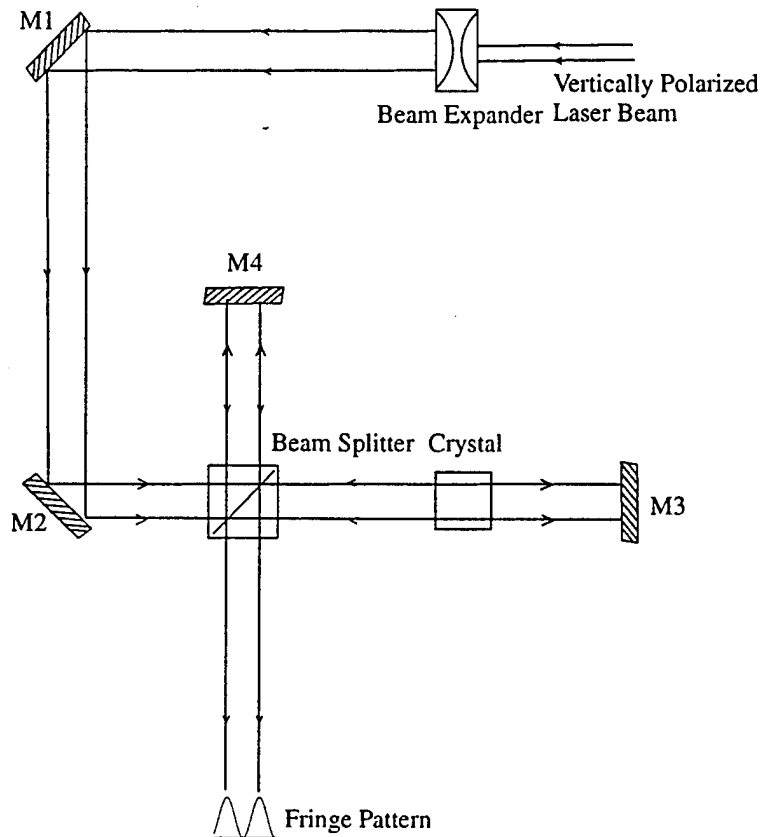
Fig. 6-7 Experimental Setup For Measuring The Interference Pattern

From this experiment, the electro-optic coefficient could be determined by measuring the resultant shift of the interference fringe pattern due to applying an electric field across the crystal. As a voltage V was applied to a crystal, the resultant refractive index change in the crystal would be

$$\Delta n = (r_{33}n_e^3 - r_{13}n_o^3)V/2d$$

where d was the width of the crystal. This refractive index change caused a difference of the optical path between two beams, which was equal to $2 \cdot \Delta n \cdot l$ (l: the length of the crystal). Experimentally, we founded that the fringe pattern moved one space, which indicated that the optical path difference between two beams was equal to λ , when the voltage across the crystal was 625 v. Based on this data we can calculate r_{13} which is equal to 38.1 pm/v for an applied voltage of 625 v. For the same voltage of 625 v , from the data in table 6-4 we got $r_{13}(V_0=625$ v$) = 0.95 \cdot 48.5 =$ 46.1 pm/v.

Comparing these two values of r_{13} obtained by different experiment proved that our results for the electric field dependence of the electro-optic coefficient are dependable.

Finally, in order to exam the accuracy of N_A value which we obtained by using the technique of determination of phase shift. We also did an experiment to measure N_A value by using a traditional method of changing the angle between two beams. The basic theory and measurement steps are as follows (Ref [4]).

Due to two-beam coupling, the weak beam I_1 experiences an increase in intensity

101

along its propagation direction which is (see Appendix I)

$$\frac{I_{1c}}{I_1} = \frac{(1+m)\,e^{\gamma L_{eff}}}{1 + m\,e^{\gamma L_{eff}}} \qquad\qquad (6\text{-}6)$$

where $m = I_{01} / I_{02}$, a ratio of the weak beam intensity to the strong beam intensity.

Experimentally, we measured I_{1c}, I_1 and m, and then calculated γL_{eff}.
In other hand,

$$\gamma = R\,\frac{2\pi R_{eff} K_B T}{\lambda n \cos\theta e}\,\frac{K_g}{1 + (K_g / K_0)^2} \qquad\qquad (6\text{-}7)$$

where $R_{eff} = n_e^4 r_{33} \cos^2\theta - n_0^4 r_{13} \sin^2\theta$ for an extraordinary ray, K_g is grating

constant and $K_0^2 = \dfrac{4\pi e^2}{K_B T}\left(\dfrac{N_{eff}}{\epsilon}\right) = C\left(\dfrac{N_{eff}}{\epsilon}\right)$ provided $C = 4\pi e^2 / K_B T$, and R is the

measure of the electro-hole competition in the formation of the space-charge field.

By defining $f(\theta) = \cos\theta \; / \; (\cos^2\theta - \dfrac{n_0^4 r_{13}}{n_e^4 r_{33}} \sin^2\theta)$ we will have

$$\gamma L_{eff} f(\theta) \propto \frac{K_g}{1 + \dfrac{K_g^2}{C}\Big/\Big(\dfrac{N_{eff}}{\epsilon}\Big)}$$

By plotting the data of $\gamma L_{eff} f(\theta)$ vs K_g and fitting the data, we then obtained a value

of N_{eff}/ϵ. The data we measured and calculated are listed in Table 6-5, and the

fitting curve is shown in Fig.6-8. The fitting results gave us the value of N_{eff}/ϵ

which was

Table 6-5

2θ	$k_g(\times 10^4)$	I_1	I_{1c}	I_{1c}/I_1	$e^{\gamma L_{eff}}$	γL_{eff}	$f(\theta)$	$\gamma L_{eff} \cdot f(\theta)$
5°	0.77899	654	875	1.33792	1.36091	0.30815	1.00144	0.30859
7.8°	1.12148	744	1215	1.63306	1.68645	0.52147	1.00351	0.52330
10.5°	1.63445	804	1560	1.94030	1.03602	0.7110	1.00638	0.71554
12°	2.0740	594	1250	2.10438	2.22737	0.80082	1.00835	0.80751
23°	3.9558	201	605	3.00995	3.34624	1.20784	1.03137	1.24573
29.2°	5.0015	713	2325	3.26087	3.67647	1.30195	1.05156	1.36908
40°	6.13152	522	1485	2.84483	3.13391	1.14228	1.10138	1.25809
51°	7.73695	739	2100	2.64817	2.8860	1.05987	1.17616	1.24658
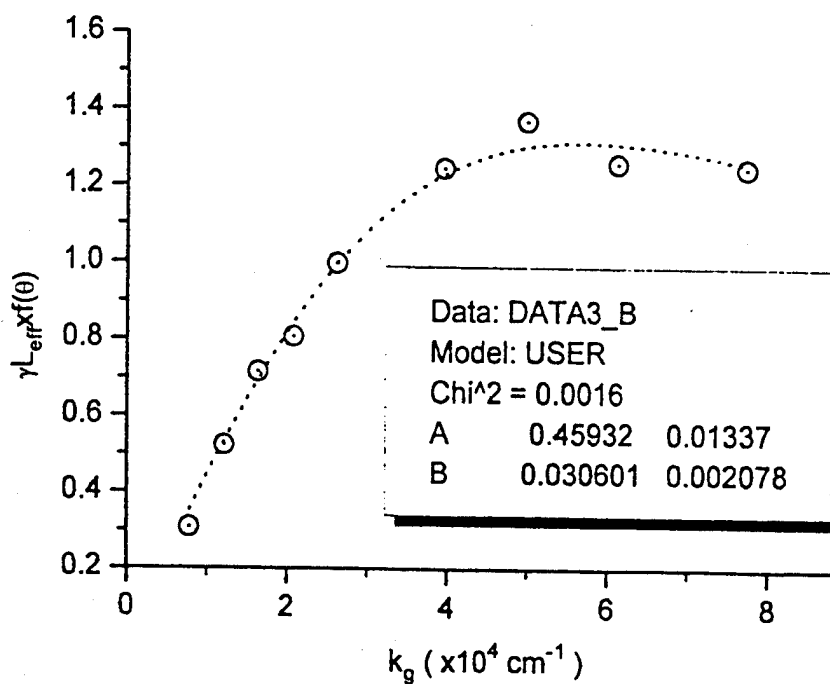
Fig. 6-8

$$N_{eff}/\epsilon = (4.59 \pm 0.31) \times 10^{13} (cm^{-3})$$

Therefore, from the data we have obtained, we can see that

1. We got a very good fitting for the data of sin φ vs E_0 and tan φ vs E_0 from our phase shift measurement. Also, two values of N_{eff}/ϵ obtained in two different experiments are so close. All these provide an evidence that the new technique of measuring N_A developed by us is accurate and dependable.

2. Based on the experimental data, we got fitting curves for the electric field dependance of both the dielectric constant and the electro-optic coefficient which were shown in Fig 6-5 and 6-6. In Ref. [5] the author also plotted these two curves of ϵ vs E_0 and r vs E_0. Ours have the same shape with theirs. This varifies

104

indirectly the validity of our new developed technique.

IV. Calculations Of Electron-Hole Competition

If electrons and holes occur simultaneously in the charge transport process, there will be a electron-hole competition in the formation of the space-charge field which will lead to a reduction in strength of the photorefractive effect. Suppose both electrons and holes can be excited from (and to) a single impurity band, then by employing band-transport model in Ch. 3, a first-order differential equation for the time evolution of the space-charge field can be derived which is (see Ref. [6])

$$-\frac{dE_1(t)}{dt} = E_1(t)\{\frac{n_{e0}e\mu_e[1+k(k-iV)/k_0^2]}{\in[1+k(k-iV)/K_e^2]} + \frac{n_{h0}e\mu_h[1+k(k+iV)/k_0^2]}{\in[1+k(k+iV)/K_h^2]}\}$$

$$+ \frac{imk_BT}{e}\{\frac{n_{e0}e\mu_e(k-iV)}{\in[1+k(k-iV)/K_e^2]} - \frac{n_{h0}e\mu_h(k+iV)}{\in[1+k(k+iV)/K_h^2]}\} \quad (6\text{-}8)$$

where $n_{e0} = s_e I_0(N_D-N_A)/\gamma_e N_A$ and $n_{h0} = s_h I_0 N_A/\gamma_h(N_D-N_A)$ are zeroth-order free-carrier density.

$K_e^{-2} = k_BT\mu_e/e\gamma_e N_A$, $K_h^{-2} = k_BT\mu_h/e\gamma_h(N_D-N_A)$, $k_0^2 = e^2N_A(N_D-N_A)/\in k_BTN_D$ and

$V = eE_0/k_BT$. K_e^{-1} and K_h^{-1} are average distance travelled by electrons and holes between excitation and recombination, E_0 is the externally applied field.

If the charge carrier is only electron, then $\mu_h=0$, $K_h^{-1}=0$, and $K_h\rightarrow\infty$. If the charge carrier is only hole, then $\mu_e=0$, $K_e^{-1}=0$, and $K_e\rightarrow\infty$.

If we write eq. (6-8) as

$$-dE_1(t)/dt = AE_1(t) + B \qquad\qquad (6\text{-}9)$$

The solution for eq. (6-16) is

$$E_1(t) = (\, Be^{-At} - B\,)/A$$

At equilibrium, the steady-state space-charge field is

$$E_{sc} = -B/A$$

As no voltage is applied to a crystal, v is equal to zero in eq. (6-8). Then we have

$$A = (e/\epsilon)\,(1+k^2/k_0^2)\left(\frac{n_{eo}\mu_e}{1+k^2/K_e^2} + \frac{n_{ho}\mu_h}{1+k^2/K_h^2}\right)$$

$$B = \left(\frac{imk_BT}{e}\right)(e/\epsilon)\,k\left(\frac{n_{eo}\mu_e}{1+k^2/K_e^2} - \frac{n_{ho}\mu_h}{1+k^2/K_h^2}\right)$$

Thus, the steady-state space-charge field is

$$E_{sc} = -\frac{imk_BT}{e}\left(\frac{k}{1+k^2/K_0^2}\right)\left(\frac{n_{eo}\mu_e}{1+k^2/K_e^2} - \frac{n_{ho}\mu_h}{1+k^2/K_h^2}\right)$$

$$/\left(\frac{n_{eo}\mu_e}{1+k^2/K_e^2} + \frac{n_{ho}\mu_h}{1+k^2/K_h^2}\right)$$

or $\qquad E_{sc} = -\dfrac{imk_BT}{e}\,\dfrac{k}{1+k^2/k_0^2}\,R$

where $\quad R = (\,1-C\,)/(\,1+C\,)$

with $\quad C = s_h N_A (k_g^2 + K_e^2)/[s_e(N_D - N_A)(k_g^2 + K_h^2)]$

If the charge carrier is only electron $C=0$, $R=1$, and if the charge carrier is only hole $C \to \infty$, $R=-1$. Therefore, $R=1$ or -1 indicates no electron-hole competition. From our data in table 6-5 we plotted K_g/γ vs K_g^2 and fitted the points. The results gave us a straight line which is shown in Fig. 6-9. The slope and the y-intercept of the line enable us to determine the electro-hole competition R, which is found to be
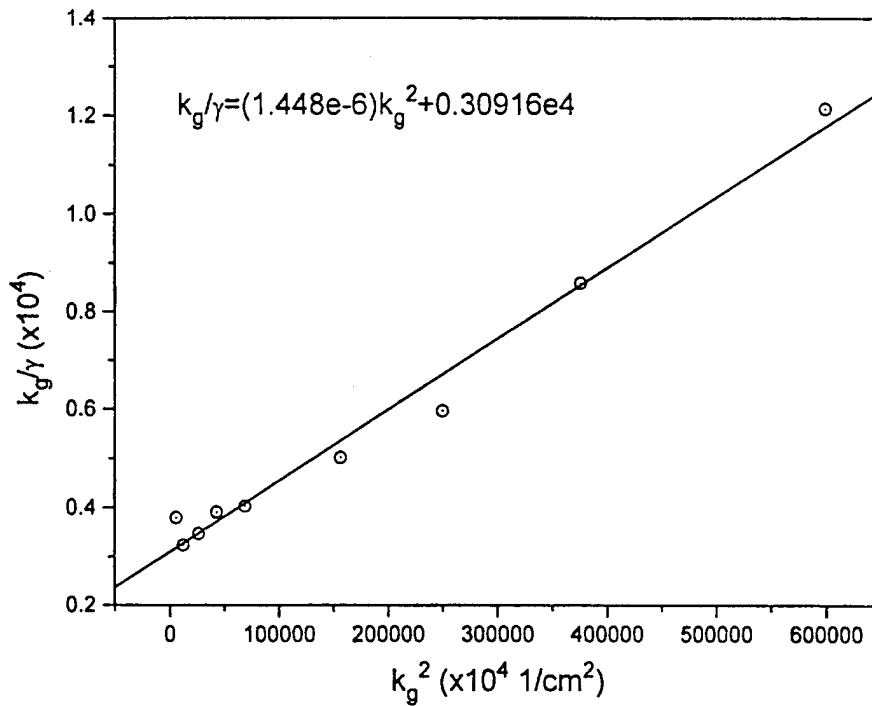
Fig. 6-9 Determination of Electron-Hole Competition Factor

0.98. This indicates that there is no electron-hole competition in the formation of the space-charge field.

V. Conclusion

We have demonstrated a new technique for the measurement of the trap density in photorefractive materials. This technique has been shown to give the same result for the trap density as the conventional two-beam coupling technique but is more convenient to carry out in practice. The technique presented here also yields

the electric field dependence of both the dielectric constant and the electro-optic coefficient. In addition, an electro-hole competition was determined based on our data of gain versus grating constant. The result indicates that there is no electron-hole competition for our crystal.

VII. GRATING WRITING AND ERASURE TIMES

In developing an effective photorefractive optical limiter it is important to have in hand a good understanding of the physics of the response time of the material. Therefore, part of our research effort has been focused on developing a clear picture of the writing and erasing photorefractive response times. Our results are in strictly excellent agreement with our photorefractive model although some are intuitively surprising. For example, we have found the I^{-1} dependence to be vigorously followed for our SBN samples while we have found that, contrary to suggestions in the literature, the writing and erasing times are not equal for equal incident intensities.

Investigation On Grating Formation Time And Erasure Time

Analytical Solution For Grating Erasure Time

When a grating is being written the total current due to the electrons in the conduction band can be expressed as $j = j_0 + j_1 e^{ikx}$, where $j_0 = e\mu n_0 E_0$ depends on the applied field and j_1 has two parts j_D and j_E. The j_D part is a current due to the diffusion and the j_E is a current due to the formation of the space-charge field. In this physical picture, the direction of net electron flow is the same as the electric field direction. But

Electron Distribution

$\partial n/\partial x > 0$ $\partial n/\partial x < 0$

$j_{\text{diffusion}}$ $j_{\text{diffusion}}$
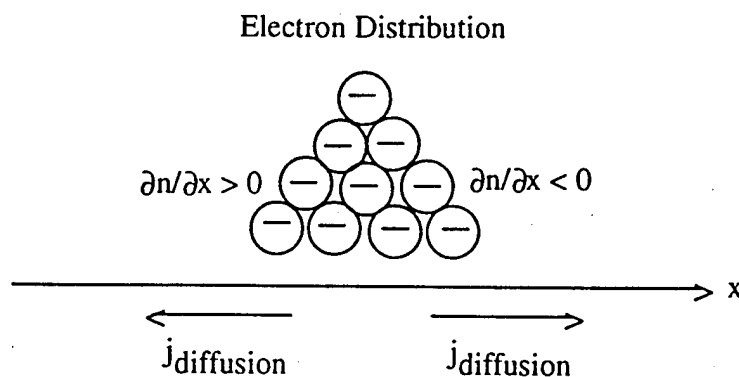
when a grating is erasing the situation is different from the writing case.

1. The current still has two parts j_0 and j_1, however, the direction of net electron flow is now opposite to the direction of the space-charge field. Therefore, we have to write the current as $j = j_0 - j_1 e^{ikx}$ where the minus sign can be explained as a 180° phase shift.

2. In the grating erasing case the electron are driven by the space-charge field. The part of j_1 due to diffusion can often be neglected.

3. During the period of erasing a grating the optical intensity is uniform, and can be written as $I = I_0$.

Based on the above consideration the four basic equations describing the photorefractive effect in a grating erasing case should be written as

$$\frac{\partial n}{\partial t} - \frac{\partial N_D^+}{\partial t} = -\frac{1}{e}\frac{\partial j^-}{\partial x} \qquad (7\text{-}1)$$

$$\frac{\partial N_D^+}{\partial t} = SI(N_D^- - N_D^+) - \gamma_R n N_D^+ \qquad (7\text{-}2)$$

$$j = e\mu nE \qquad (7\text{-}3)$$

$$\frac{\partial E}{\partial x} = \frac{4\pi e}{\epsilon}(n + N_A - N_D^+) \qquad (7\text{-}4)$$

Then the assumptions are

$$I = I_0 \qquad (7\text{-}5)$$

$$n = n_0 + n_1(t)\, e^{ikx} \qquad\qquad (7\text{-}6)$$

$$N_D^+ = N_{D0}^+ + N_{D1}^+(t)e^{ikx} \qquad\qquad (7\text{-}7)$$

$$E = E_0 + E_1(t)\, e^{ikx} \qquad\qquad (7\text{-}8)$$

$$j = j_0 - j_1(t)\, e^{ikx} \qquad\qquad (7\text{-}9)$$

By substituting (7-5) - (7-9) into (7-1) - (7-4) we can obtained a second-order diffrential equation which is

$$\frac{\partial^2 E_1}{\partial t^2} + \left(\frac{1}{\tau_R} - \frac{1}{\tau_{di}} - \frac{i}{\tau_E}\right)\frac{\partial E_1}{\partial t} + \left(-\frac{1}{\tau_{di}\tau_R} - \frac{i}{\tau_I\tau_E}\right)E_1 = 0 \qquad (7\text{-}10)$$

The solution for (7-10) is

$$E_1(t) = E_{sc}^{(eq)} e^{-t/\tau_e} \cdot e^{i\omega t} \quad \text{where}$$

$$\tau_e = \tau_{di}\,\frac{1 + \left(\dfrac{\tau_R}{\tau_E}\right)^2}{1 - \left(\dfrac{\tau_R}{\tau_E}\right)^2 \left(\dfrac{\tau_{di}}{\tau_I}\right)} \qquad\qquad (7\text{-}11)$$

is the grating erasure time.

111

In the writing case, the grating writing time (or say " grating growing time") is given by eq. (4-5), which is

$$\tau = \tau_{di} \frac{(1 + \frac{\tau_R}{\tau_D})^2 + (\frac{\tau_R}{\tau_E})^2}{[1 + (\frac{\tau_R}{\tau_D})(\frac{\tau_{di}}{\tau_I})] (1 + \frac{\tau_R}{\tau_D}) + (\frac{\tau_R}{\tau_E})^2 (\frac{\tau_{di}}{\tau_I})}$$

In the case that $\tau_R \ll \tau_D$, eq. (4-5) can be written as

$$\tau_g = \tau_{di} \frac{1 + (\frac{\tau_R}{\tau_E})^2}{1 + (\frac{\tau_R}{\tau_D})(\frac{\tau_{di}}{\tau_I}) + (\frac{\tau_R}{\tau_E})^2 (\frac{\tau_{di}}{\tau_I})} \qquad (7\text{-}12)$$

If we now compare (7-11) with (7-12), it is clear that the grating erasure time is longer than the writing time. This is true even in the case of zero field but is particularly important for the applied field case since τ_E can be on the order of τ_R and τ_{di} can be 10 times longer than τ_I.

Experimental Measurement For Grating Writing Time And Erasing Time

Experimentally, we measured the writing time and the erasing time of photorefractve index gratings for SBN:60 with Cerium as a dopant. The

experimental set up is shown in Fig. 7-1.
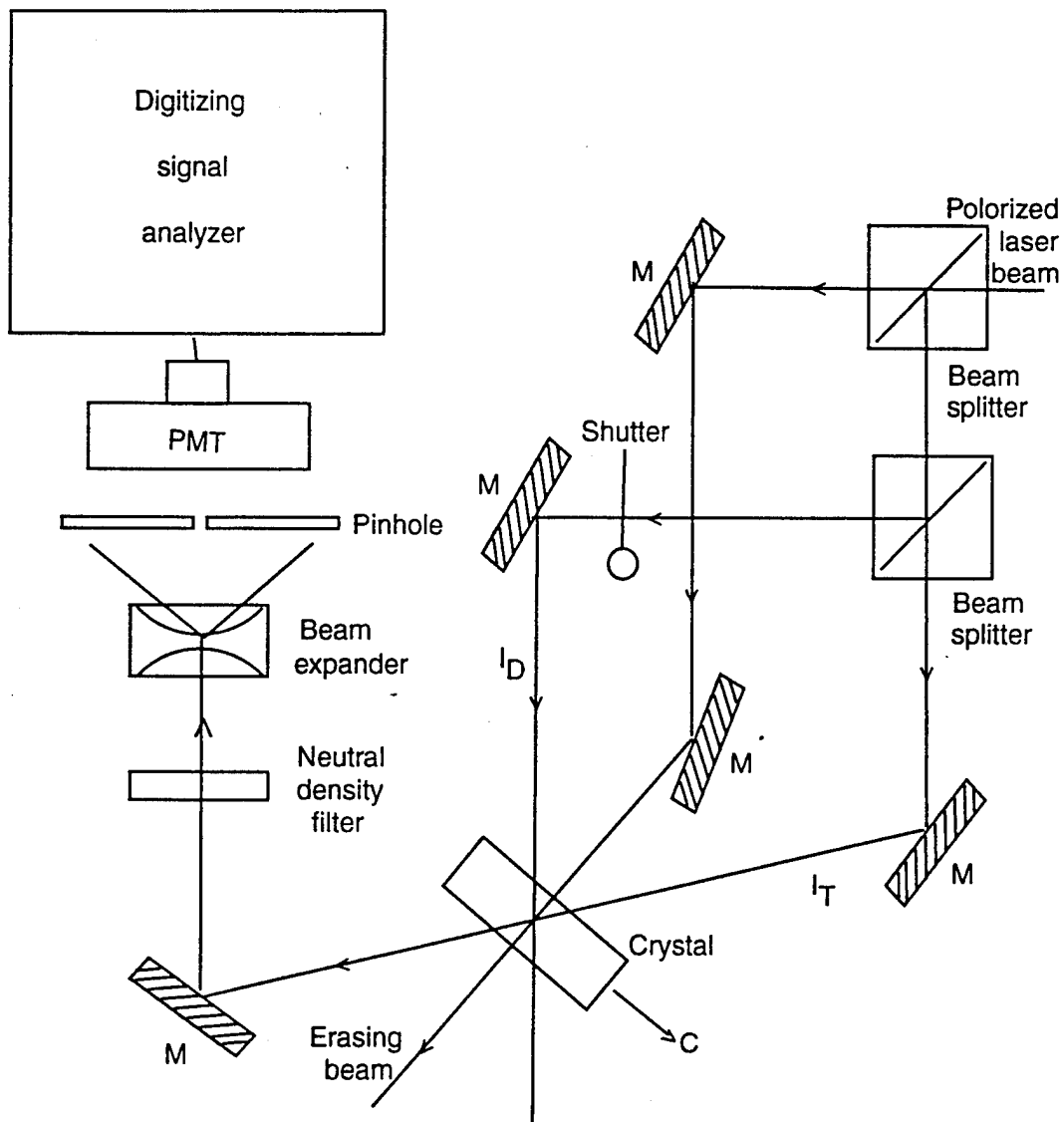
Fig. 7-1 Experimental setup for measuring the linear response

Determination for the varying function of the grating erase with time -

asingle exponential decay function

In order to measure the grating erasing time we must first know the function of how the grating erasure varying with time. We measured a diffraction signal for a SBN sample as a function of time. The results are shown in Fig. 7-2, which indicated that the grating erase is a single exponential time decay function.

$$\eta = 0.19916 + 1.98785 \cdot e^{-\frac{t}{28.11747}}$$

Data: DATA1_B
Model: ExpDecay
Chi^2 = 0.0001392

y0	0.19916	0.00602
x0	0	••••
A1	1.98785	0.00986
t1	28.11747	0.41125
A2	0	••••
t2	582.38482	••••
A3	0	••••
t3	0	••••
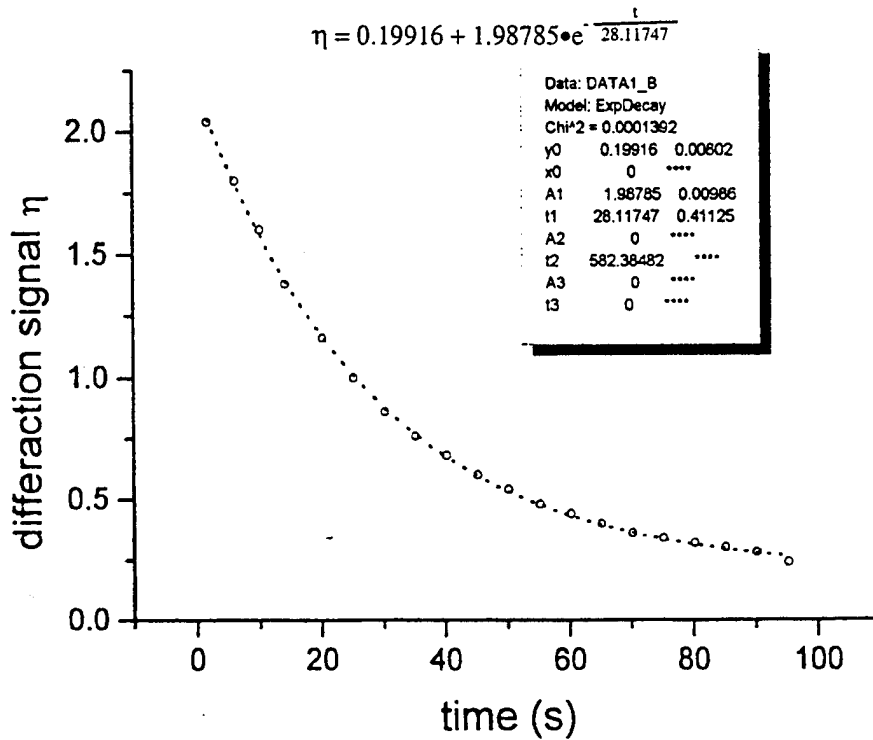
Fig. 7-2   Single Exponential Decay Function

Measurement for grating growing time and erasing time

Our experimental parameters were: wavelength = 458 nm, total laser power = 25 mw, the full crossing angle between two beams = 10°, and the intensity ratio of two beams = 1:100. Experimentally, the weak beam was detected. At first the energy exchange signal was traced by DSA oscilloscope, from which a grating growing time

114

τ_g can be measured. After the refractive index grating being formed inside the crystal we blocked the detected beam and then the diffraction signal due to the strong beam was traced by DSA oscilloscope, from which a grating erasure time τ_e can be measured.

The curve of grating formation is shown in Fig. 7-3, and that of grating erase is in Fig. 7-4. The measurement results for the grating growing time and the erasing time are τ_g=2.66 s and τ_e=4.22 s, respectively, which showed that the grating erasure time is longer than the grating formation time. Quantitatively, in this measurement the
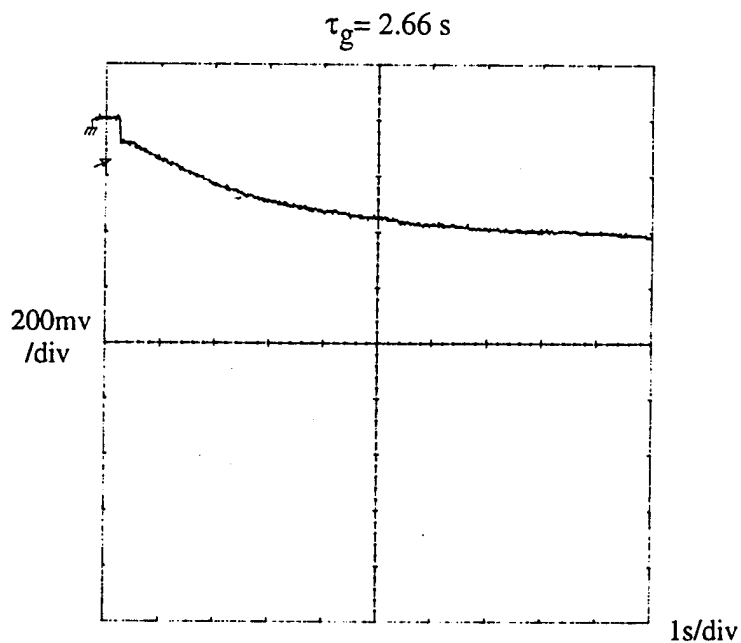
Fig. 7-3 Grating Formation Time

$$\tau_e = 4.22 \text{ s}$$

200mv /div

1s/div
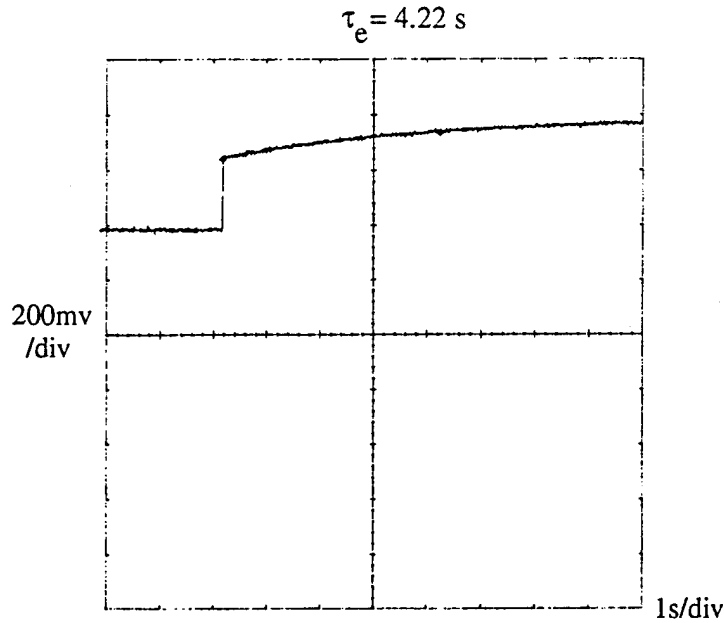
Fig. 7-4   Grating Erasure Time

grating erasure time is about 1.6 times of the grating formation time.

Another measurement of the grating writing time τ_g and the erasing time τ_e was performed for BaTiO$_3$ crystal with different k_g values. The measurement results are (1) $\tau_e/\tau_g = 1.5$ for crossing angle of 14°; (2) $\tau_e/\tau_g = 1.9$ for crossing angle of 40°. These results agree with the theoretical predictions that (1) the grating erasure time is longer than the grating growth time and (2) the ratio of the grating erasure time to the grating growth time is increased with k_g increased.

Comparison Of Experimental Data With Theoretical Calculation

In the case of no applied field, eq. (7-11) gave an erasing time of $\tau_e = \tau_{di}$ and eq.

116

(7-12) gave a growth time of

$$\tau_g = \frac{\tau_{di}}{1 + (\frac{\tau_R}{\tau_D})(\frac{\tau_{di}}{\tau_I})}$$

For the parameters of $\lambda=458$ nm, $2\theta=10°$, $N_A=1\bullet 10^{16}$ cm^{-3} and $N_D=10N_A$, we can

calculate the ratio of grating erasure time to formation time which is 1.8. This

theoretical value is close to the experimental result for the ratio of 1.6 which we

measured. Therefore, the experimental results conform the theoretical analysis for

the photorefractive grating erasure time which we derived in the beginning of this

chapter. Both theoretical and experimental results do indicate that the grating

erasure time is longer than the growth time.

From eq. (7-11) and (7-12) we can obtain

$$\frac{\tau_e}{\tau_g} = \frac{1 + (\frac{\tau_R}{\tau_D})(\frac{\tau_{di}}{\tau_I}) + (\frac{\tau_R}{\tau_E})^2(\frac{\tau_{di}}{\tau_I})}{1 - (\frac{\tau_R}{\tau_E})^2(\frac{\tau_{di}}{\tau_I})}$$

$$= (1 + Ak_g + Bk_g^2) / (1 - Bk_g^2) \qquad (7-13)$$

where $A = \mu E_D \tau_R \tau_{di} / \tau_I$ and $B = \mu^2 E_0^2 \tau_R^2 \tau_{di} / \tau_I$.

From eq. (7-13), we can see that the ratio of the grating erasure time to the

growth time is increased with k_g increased.

Dependence Of Grating Erasure Time On Applied DC Filed

In the last section we have seen that in the case of no applied field the grating

erasure time is longer than the formation time, both theoretically and experimentally. We have measured the grating erasure time without field, which was 4.22 s (see Fig.4-7). But what happens when a DC field is applied? According to our theoretical analysis given by eq.(7-11), the grating erasing time should get longer with a DC field than that with no field. In order to verify the theoretical prediction, experimentally, we measured a grating erasure time with a DC field applied to the crystal. The experimental parameters were same as those described in last section. When a DC field of 6 kv/cm was applied to the crystal, a grating erasure time of 6.4 s was measured. This erasing time of 6.4 s is obviously longer than the erasing time of 4.22 s with no field obtained in last section (Fig.4-7).

Then with eq.(7-11), we calculated the theoretical value of grating erasing time with a DC field of 6 kv/cm. The calculated result for grating erasure time with a DC field of 6 kv/cm was 7.0 s. This is close to the experimental result of 6.4 s. Therefore, the theoretical prediction for the grating erasure time given by eq.(7-11) is dependable. Both theoretical and experimental results indicates that the grating erasure time depends on the applied field. In the case of a DC field applied to a crystal the grating erasure time is getting longer than that in the case of no field.

Dependence Of Grating Erasure Rate On Optical Intensity

Photorefractive crystals have been used to demonstrate several novel operations

in real-time optical data processing. Understanding the time dependent behavior in these materials is important both for predicting the response of the photorefractive crystals and for determining how to modify them to improve response (Ref. [2]-[5]).

In this chapter we will present the data which show the dependance of light-induced erasure rate of a refractive index grating on optical intensity. Our measurement was performed for SBN crystals and BaTiO$_3$ crystals, respectively. Different behavior of the dependance were obtained for these two types of crystals. The curve fitting results showed that in SBN the speed of erasure of a photorefractive index change is linearly dependent on the intensity of the erasing beam with and without an applied field. However, in BaTiO$_3$ this erasure rate of a photorefractive grating scaled sublinearly with optical intensity, with and without a field.

Experimental Setup And Data Collection

The experimental setup is shown in Fig. 7-1. Two writing beams wrote a photorefractive grating inside a crystal. The third beam which bisected two writing beams was used to erase the grating. It is called erasing beam. Experimentally, we detected the weak beam. After the grating being formed inside the crystal we blocked the detected beam, and at the same time turned on the erasing beam. Then a diffraction signal from another beam was sent to PMT and measured by DSA. By

changing the intensity of erasing beam we are able to measure the dependance of the grating erasure rate on the optical intensity. Our measurement were performed for two SBN thin samples, two $BaTiO_3$ thin samples and one $BaTiO_3$ thick sample. The experimental data of grating erasure time versus erasing beam intensity are listed in Table 7-1 to Table 7-3. The fitting results are shown in Fig. 7-5 to Fig. 7-11. From the fitting curves we found that there is a very good linear dependance of the grating erasure time on optical intensity for SBN samples. But for $BaTiO_3$ samples the behavior shown are apparently sublinear. The fitting results gave an $I^{-0.67}$ dependence for one $BaTiO_3$ thin sample, $I^{0.72}$ dependence for another $BaTiO_3$ thin sample and $I^{(0.8-0.84)}$ dependence for the $BaTiO_3$ thick sample.

Table 7-1   Data of Measuring the Linear Behavior for SBN Crystals
Thin Sample #1

Neutral density filter I_{erase}(mw) τ'(s) τ_{dark}(s) $1/\tau=1/\tau'-1/\tau_{dark}$ (1/s)
in erasing beam

0	75	0.052	790	19.23
1	5.5	0.67	790	1.491
2	0.55	6.7	790	0.148
3	0.055	70	790	0.013
4	0.0055	376	790	0.00139

Thin Sample #2

Neutral density filter I_{erase}(mw) τ'(s) τ_{dark}(s) $1/\tau=1/\tau'-1/\tau_{dark}$ (1/s)

in erasing beam

0	20	0.1503	75.633	6.6419
1	2	1.52	75.633	0.6447
2	0.2	13.47	75.633	0.061
3	0.02	50.706	75.633	0.0065
4	0.002	71.369	75.633	0.00079

SBN Sample 1 $\quad \dfrac{1}{\tau_{decay}} \sim (I_{erase})^{1.008}$

Fig. 7-5

$$\frac{1}{\tau_{decay}} \sim (I_{erase})^{0.9836}$$

SBN Sample 2
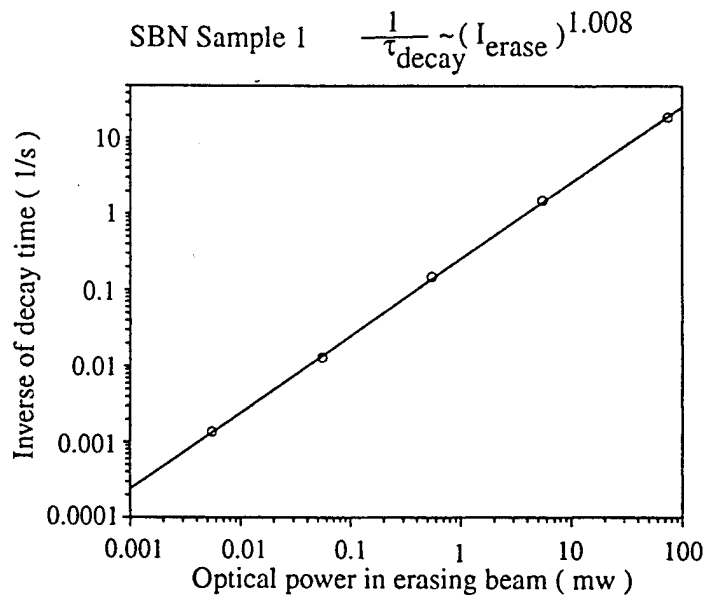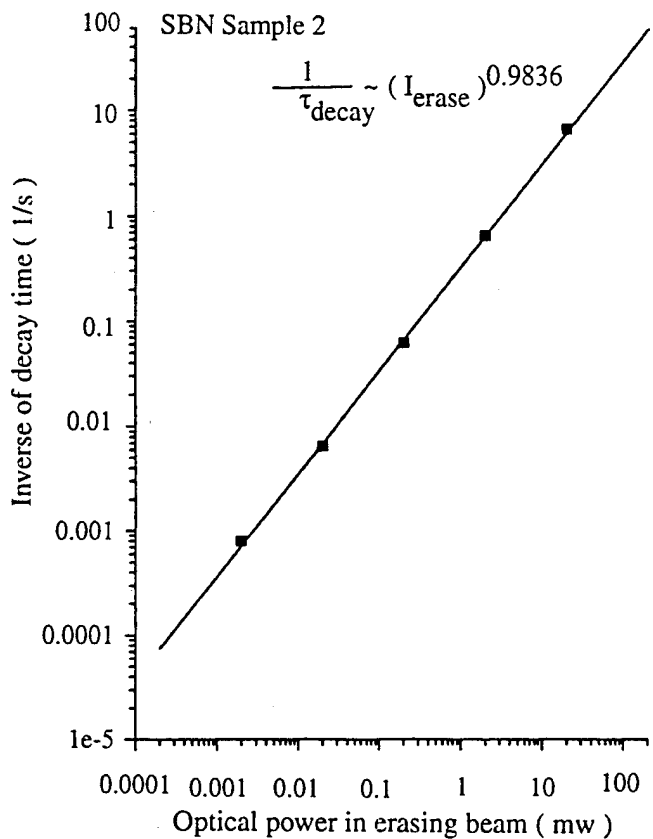
Fig. 7-6

Table 7-2   Data of Measuring the Linear Behavior for BaTiO$_3$ Crystals

Thin Sample #1

I_{erase}(mw)	τ' (s)	τ_{dark} (s)	τ [$1/\tau = 1/\tau' - 1/\tau_{dark}$ (1/s)]
0.8	19.0	40	36.2
2	13.4	40	20.2
3.2	10.8	40	14.8
8	6.50	40	7.76
32	2.92	40	3.15
80	1.62	40	1.69

122

Thin Sample #2

I_{erase}(mw)	τ' (s)	τ_{dark} (s)	τ [$1/\tau = 1/\tau' - 1/\tau_{dark}$ (1/s)]
0.8	11.4	31	18.0
2	7.28	31	9.51
3.2	5.60	31	6.83
8	3.12	31	3.47
32	1.24	31	1.29
80	0.63	31	0.64
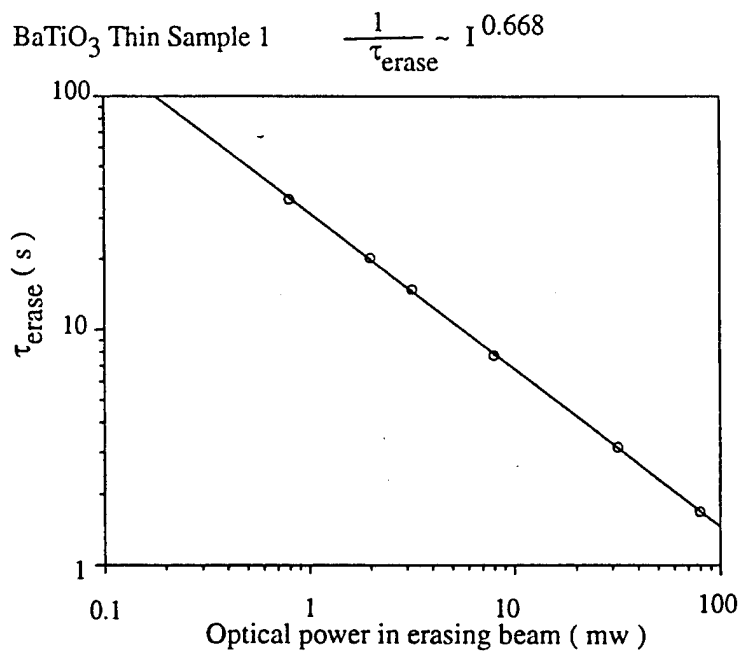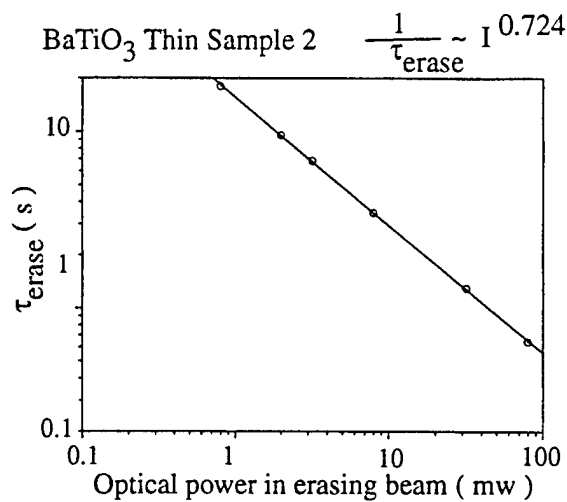
$BaTiO_3$ Thin Sample 1 $\dfrac{1}{\tau_{erase}} \sim I^{0.668}$

Fig. 7-7

$$\text{BaTiO}_3 \text{ Thin Sample 2} \qquad \frac{1}{\tau_{erase}} \sim I^{0.724}$$

Fig. 7-8

Table 7-3   Data of Measuring the Linear Behavior for BaTiO$_3$ Thick Sample

BaTiO$_3$ Thick Sample (#3)

Table A: Full crossing angle $2\theta=14°$ Table B: Full crossing angle $2\theta=40°$

Intensity (mw)	$1/\tau_{erase}$ (1/s)	Intensity (mw)	$1/\tau_{erase}$ (1/s)
217	0.6235	200	0.5665
138.23	0.3715	100	0.254
84.41	0.221	78	0.194
42.75	0.113	39.4	0.1125
33.2	0.092	30.6	0.073
13.67	0.0615	19.8	0.048
8.46	0.0355	7.8	0.021
4.25	0.0205	3.92	0.016
3.28	0.018	3.02	0.014
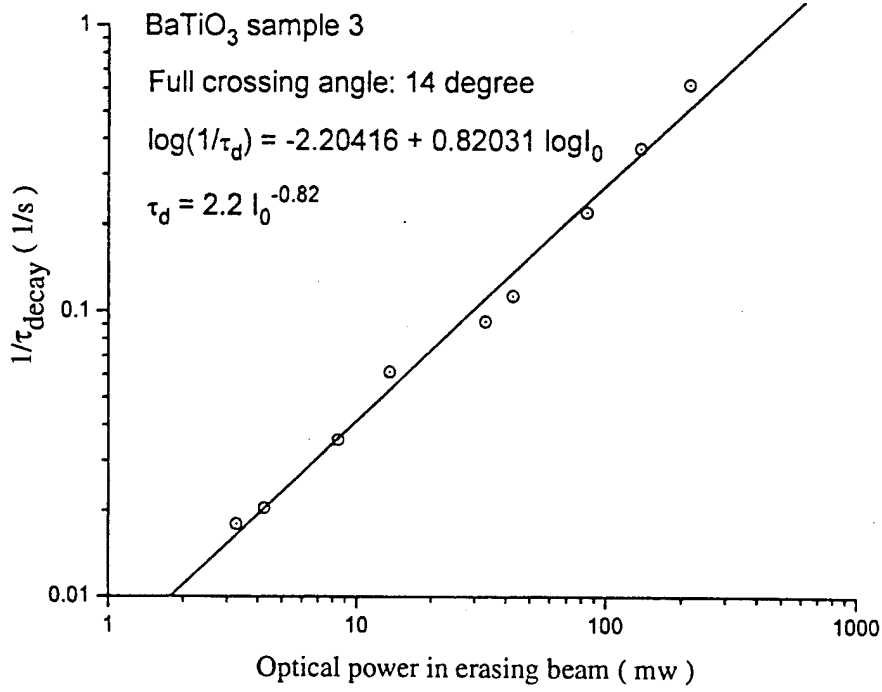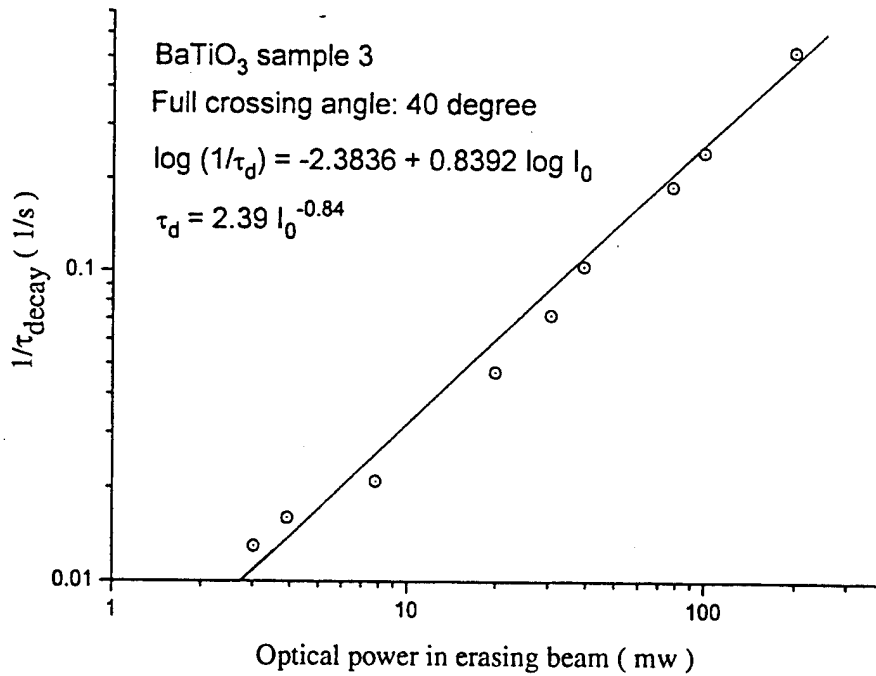
BaTiO$_3$ sample 3

Full crossing angle: 14 degree

$\log(1/\tau_d) = -2.20416 + 0.82031 \log I_0$

$\tau_d = 2.2 \, I_0^{-0.82}$

Optical power in erasing beam (mw)

Fig. 7-9

BaTiO$_3$ sample 3

Full crossing angle: 40 degree

$\log(1/\tau_d) = -2.3836 + 0.8392 \log I_0$

$\tau_d = 2.39 \, I_0^{-0.84}$

Optical power in erasing beam (mw)

Fig. 7-10

125

Table 7-3 Data of Measuring the Linear Behavior for $BaTiO_3$ Thick Sample

$BaTiO_3$ Thick Sample (#3)   Table C: Full crossing angle $2\theta=80°$

Optical Intensity (mw)	$1/\tau_{erase}$ (1/s)
208	0.5995
132.5	0.438
80.91	0.311
40.98	0.1915
31.82	0.155
20.59	0.09
13.1	0.067
8.11	0.043
4.08	0.028
3.14	0.024

BaTiO$_3$ sample 3
Full crossing angle: 80 degree
$\log (1/\tau_d) = -2.0448 + 0.79603 \log I_0$
$\tau_d = 2.05 \, I_0^{-0.8}$
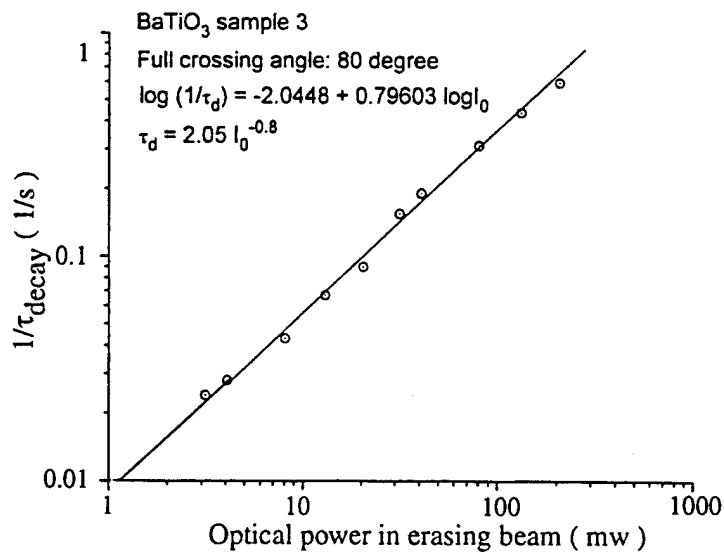
Fig. 7-11

Explanation For Sublinear Photorefractive Response Time in BaTiO$_3$

From the band transport model the photorefractive response time τ is governed by eq. (4-5), which gives τ is proportional to τ_{di}, the dielectric relaxation time. This τ_{di} is inversely proportional to n_0, the zeroth-order electron number density. In the single-donor-trap model n_0 is the only intensity-dependent parameter that affects eq. (4-5). It is simply proportional to the laser intensity, and consequently the response time τ is expected to vary inversely with intensity. The results of our measurement for the dependance of the grating erasure rate on optical intensity showed a good agreement with the theoretical prediction. But this linear behavior only happened to crystals the donor number density of which greatly exceeds that of accepters ($N_D \gg N_A$). For this type of crystals which were defined as type-A crystals (Ref. [2]-[5]), the previous models of the photorefractive effect assumed that either the donors or the accepters (but not both) took part in charge transport, and neglected thermal excitations.

However, for another type of crystals which have $N_D \leq N_A$ and are defined as type-B crystals (Ref. [2]-[5]), the band transport model should be extended to include secondary photorefractive centers. These are trapping centers that are highly ionized at room temperature but become populated by acquiring free charge carriers generated by the interaction of the laser light with the deep-level impurities. The important feature of this model is the finite thermal ionization rate of the secondary

centers, which influences the free-carrier and occupied trap concentrations. Theoretically, one more rate equation for accepters should be added to the original four basic equations (3-1) to (3-4), then the nonlinear behavior between the grating erasure rate tne the optical intensity for BaTiO3 could be explained (Ref. [6]).

Conclusionsn

Our results, both theory and experiment, show that the writing and erasure time for photorefractive materials are not the same. However, they are in practice sufficiently close considered to be on the same order. At the same time an examination of response time versus intensity dramatically supports a I^{-1} dependence for SBN. As a result our assumption for a photorefractive limiter based on SBN is validated. However, this assumption is not true for all materials.

VIII. SELF-FOCUSING AND DEFOCUSING

One of the most dramatic photorefractive phenomena observed in the laboratory has been self-focusing and self-defocusing. Either phenomena can be used together with an imaging lens and aperture as a limiter.

Fig. 8-1 shows a top view of a crystal with a 10 micron diameter beam passing through it. Without an applied voltage the beam is clearly seen to diverge due to normal diffraction. With a small applied voltage, however, the beam is seen to defy diffraction. This effect is due to the self-focusing photorefractive phenomena.

As in the case of Kerr focusing and defocusing, photorefractive focusing and defocusing can also be physically understood. To illustrate the photorefractive effect, we can first consider two plane waves of light overlapping in a crystal producing an optical interference pattern as shown in Figure 8-2. In the bright regions of the interference pattern carriers are excited into the conduction band. The excited carriers then diffuse or drift and are finally trapped in the dark regions of t interference pattern. The resulting charge separation in turn generates a space charge electric field. The drift and diffusion process continues until equilibrium is reached where the diffusion or drift current is exactly balanced by the current generated by the induced space charge field. In this way the magnitude of the field is simply determined by the value necessary to balance the diffusion or drift current. The space charge field can then distort the lattice and produce via the electro-optic an index change given by

$$\Delta n = \frac{n^3}{2} r_{eff} E_{sc} \qquad (8-1)$$

ere r_{eff} is the effective electro-optic coefficient of the material, E_{sc} is the induced space charge field, and n is the unperturbed index of refraction of the material.

The resulting induced index change can then be used in Maxwell's equation to predict the propagation behavior of the two overlapping laser beams. The result is that the induced index causes a coupling between the two beams which can be written as

Diffraction

Diffraction Compensation

WRITING A PHASE GRATING

PHOTOREFRACTIVE CRYSTAL

TRANSMITTED BEAMS

INTENSITY PATTERN

INPUT WRITING BEAMS
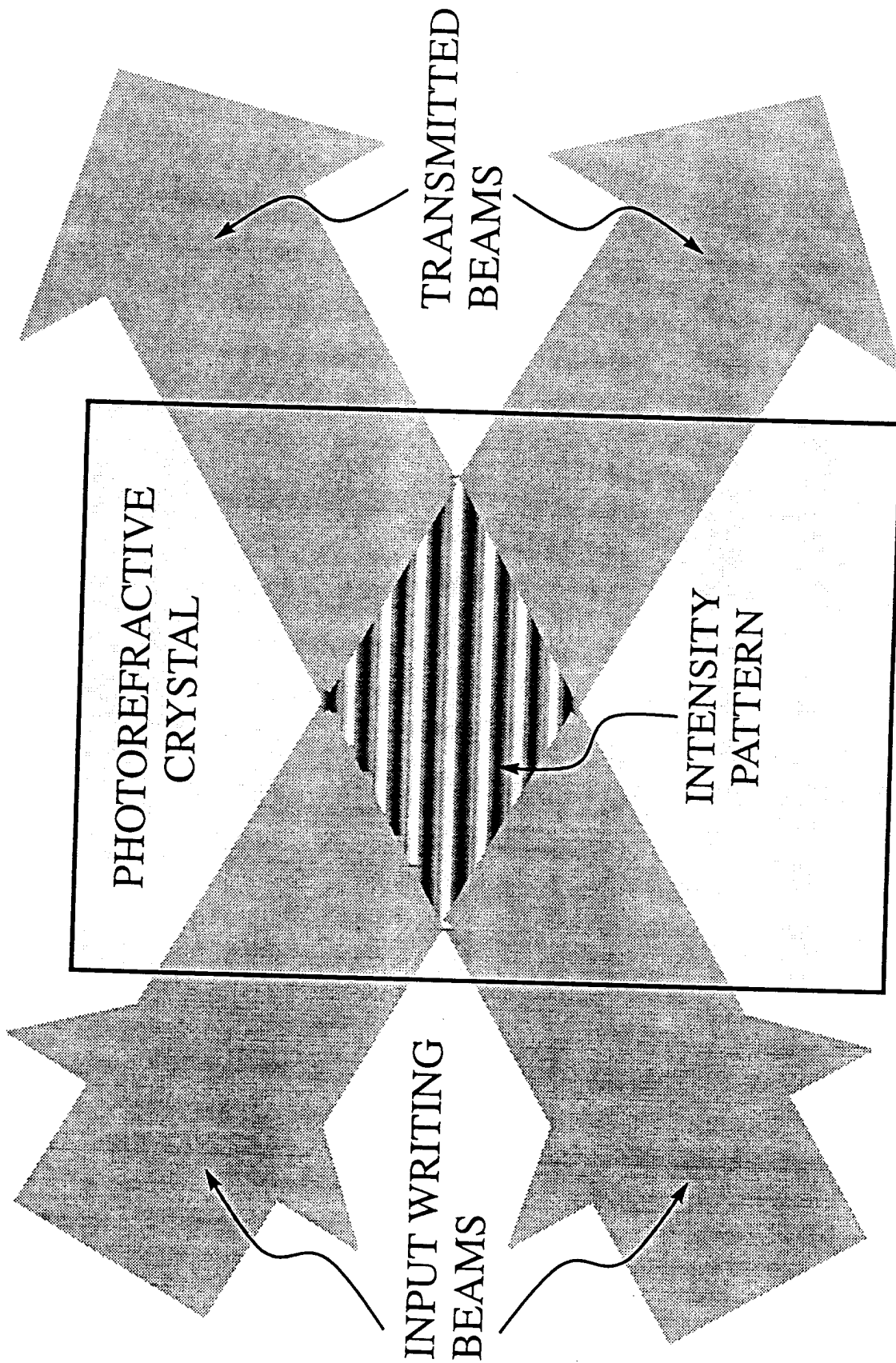
$$\frac{dE_1}{dr_1} = i(\gamma_R + i\gamma_I)\frac{E_1|E_2|^2}{I_0} \tag{8-2}$$

$$\frac{dE_2}{dr_2} = i(\gamma_R - i\gamma_I)\frac{E_2|E_1|^2}{I_0} \tag{8-3}$$

where γ is the coupling coefficient and is determined by the material effective electro-optic coefficient and the magnitude of the laser-induced space charge field. The fact that γ has real and imaginary parts points out that the coupling between the two waves causes energy exchange between them and causes each of them to see a modified index of refraction.

In the physical picture we present here, we consider a propagating finite beam to be made up of Fourier plane-wave components. As shown in Figure 8-3(a) we can form a physical picture of diffraction that is based on "watching" each Fourier component propagating through the material. Since each component has a different k-vector projection direction, the relative phase between Fourier components changes as a function of propagation distance z. Consequently, the sum of the Fourier components produces a different wave form at each z or propagation position. In the photorefractive picture each Fourier component produces an interference pattern with each and every other Fourier component. The result is that each component, therefore, "sees" a modified index of refraction which is determined by summing the index modification produced between a given Fourier component and every other component. When the low frequency Fourier components "see" a lower index than the higher frequency components due to the coupling, focusing is induced. Figure 8-3(b) Likewise, when the low frequency components "see"" a higher index than the higher frequency components, defocusing is induced (Figure 8-3(c). In practice, the sign of the index change depends on the sign of an applied external field so that focusing is induced with an applied field along the c-axis direction while defocused field opposite the c-axis direction. On interesting possibility not discussed here occurs when

132
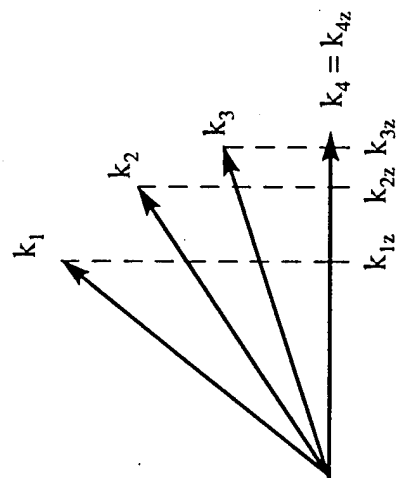
NORMAL
DIFFRACTION
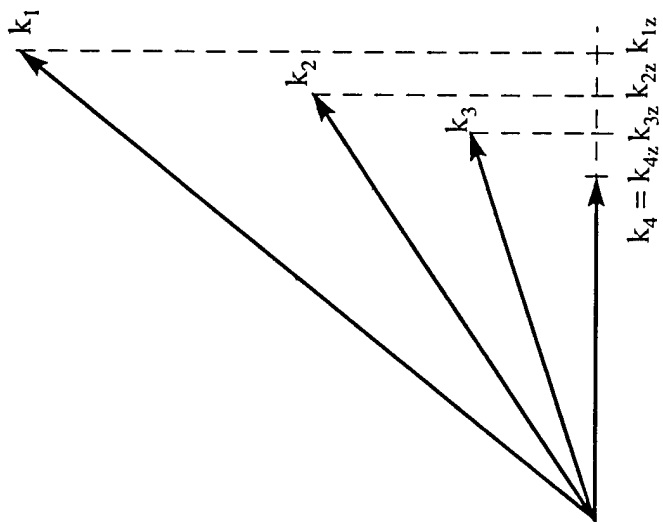
FOCUSING
BEAM
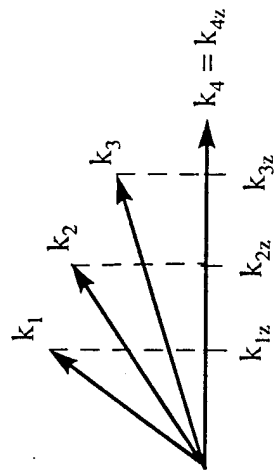
DEFOCUSING
BEAM

diffraction is exactly compensated by photorefractive focusing. In this case, shape pursuing propagation or soliton formation is observed. This picture neglects energy coupling which would result in an amplitude change of the Fourier components and would be important for a more complete analysis. In our work the effect of energy coupling was minimized by the choice of input beam diameter, the value of applied field, and the time at which the measurement was made.

The basic apparatus consisted of a cw argon-ion laser and a 5 mm x 5 mm x 6 mm strontium barium niobate (SBN) crystal with 0.01% by weight rhodium dopant. The cw argon-ion laser wavelength was 457 nm and its output beam diameter was 1.5 mm. A schematic diagram of the apparatus is shown in Figure 8-4. The output beam was directed onto a 10 cm focal length lens and the SBN crystal was placed 2.6 mm beyond the beam waist with $2 w_0 = 33 \mu m$. The beam diameter at the SBN crystal entrance face was 75 μm. The crystal was oriented with its c-axis in the horizontal plane and perpendicular to the propagation direction of the incoming laser light. The polarization of the incoming light could be varied using a polarization rotator but was initially chosen to be along the c-axis (extraordinary polarization). The beam diameter throughout the crystal was measured using an imaging system consisting of an imaging lens and a two-dimensional detector array. The input face of the 6 mm long SBN crystal was well beyond the Rayleigh range of 1.5 mm from the beam waist formed by the focusing lens. The imaging system, therefore, imaged the beam spot at the SBN entrance face with some magnification onto the detector array. As the imaging lens and the detector array are moved away from the SBN crystal, different cross sections of the Gaussian beam are then imaged onto the array. In this manner, the beam diameter at different locations throughout the SBN crystal was monitored. The magnification of the imaging system was determined by placing a thin aperture on the crystal exit (and entrance) face and imaging the aperture onto the detector array. Using the known value of the reference aperture, the magnification was determined to be about 15.6 and the
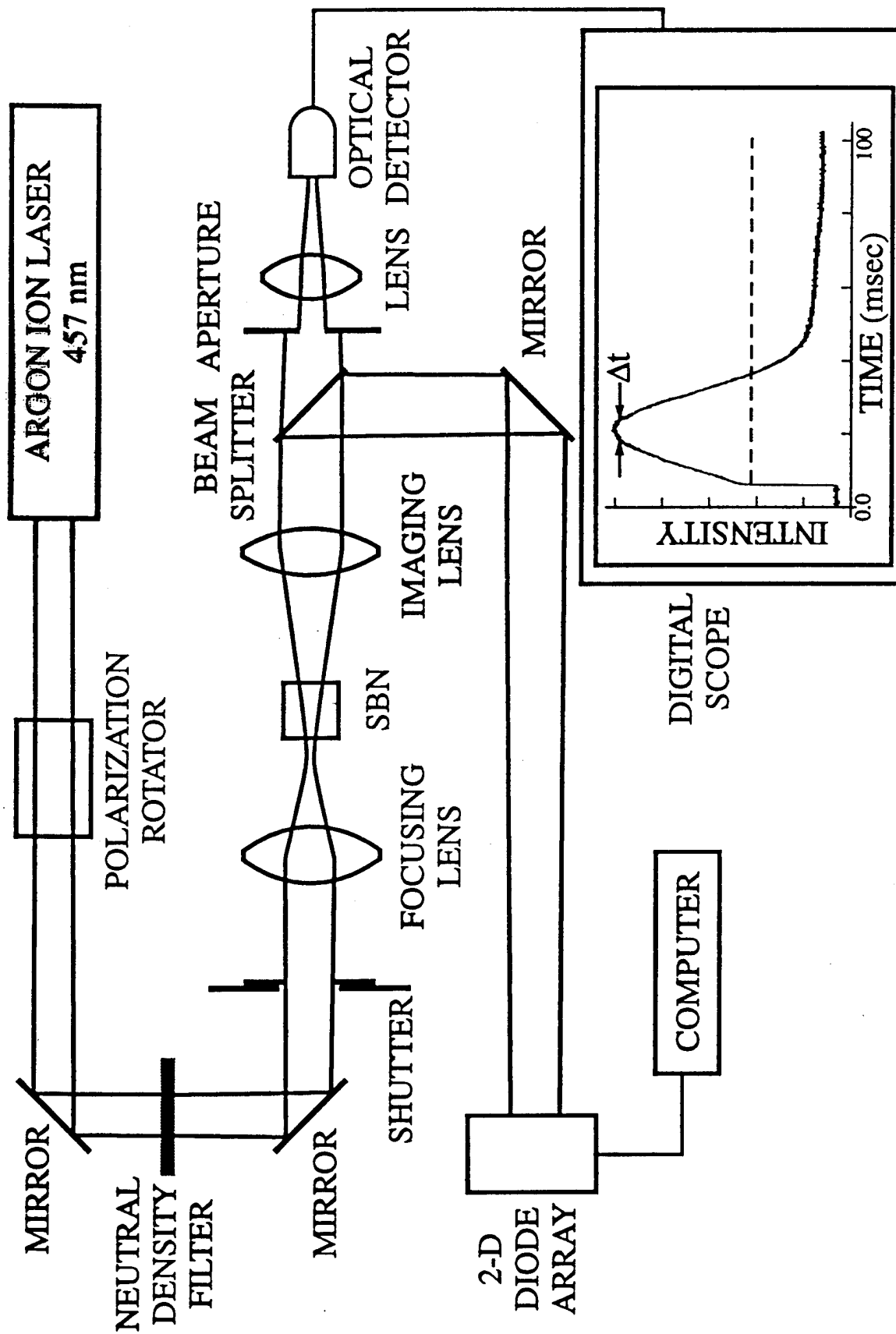
positions of the exit and entrance faces of the SBN crystal were located. Using this information the horizontal cross section of the incident beam on the entrance and exit faces of the crystal was determined. Beam diameter and viergence data were taken at a time when these quantities reached a maximum value.

Figure 8-5 shows the effect of applied voltage on the exiting beam diameter while Figure 8-6 shows its effect on the divergence of the incident beam. As shown in these two figures the photorefractive defocusing is a dramatic effect. Similar results have been observed for focusing. Only the sign of the applied d.c. electric field was reversed when producing focusing or defocusing effects. Defocusing effects are seen when the field is opposite the c-axis direction.

Conclusions

Our results clearly demonstrate the potential of photorefractive self-focusing and defocusing as an optical limiter. Both are seen to be large and dramatic effects to occur with little or low laser power. Although we have not had the opportunity to study this effect e have determined the magnitude and speed of the effect and its independence on intensity. That is, with the same applied voltage the degree of focusing and defocusing is observed to be independent of intensity over four orders of magnitude, as expected.

APPLIED VOLTAGE (VOLTS)

HALF ANGLE DIVERGENCE (MILLIRADIANS)

EXIT FACE SPOT SIZE (MICRONS)

APPLIED VOLTAGE (VOLTS)
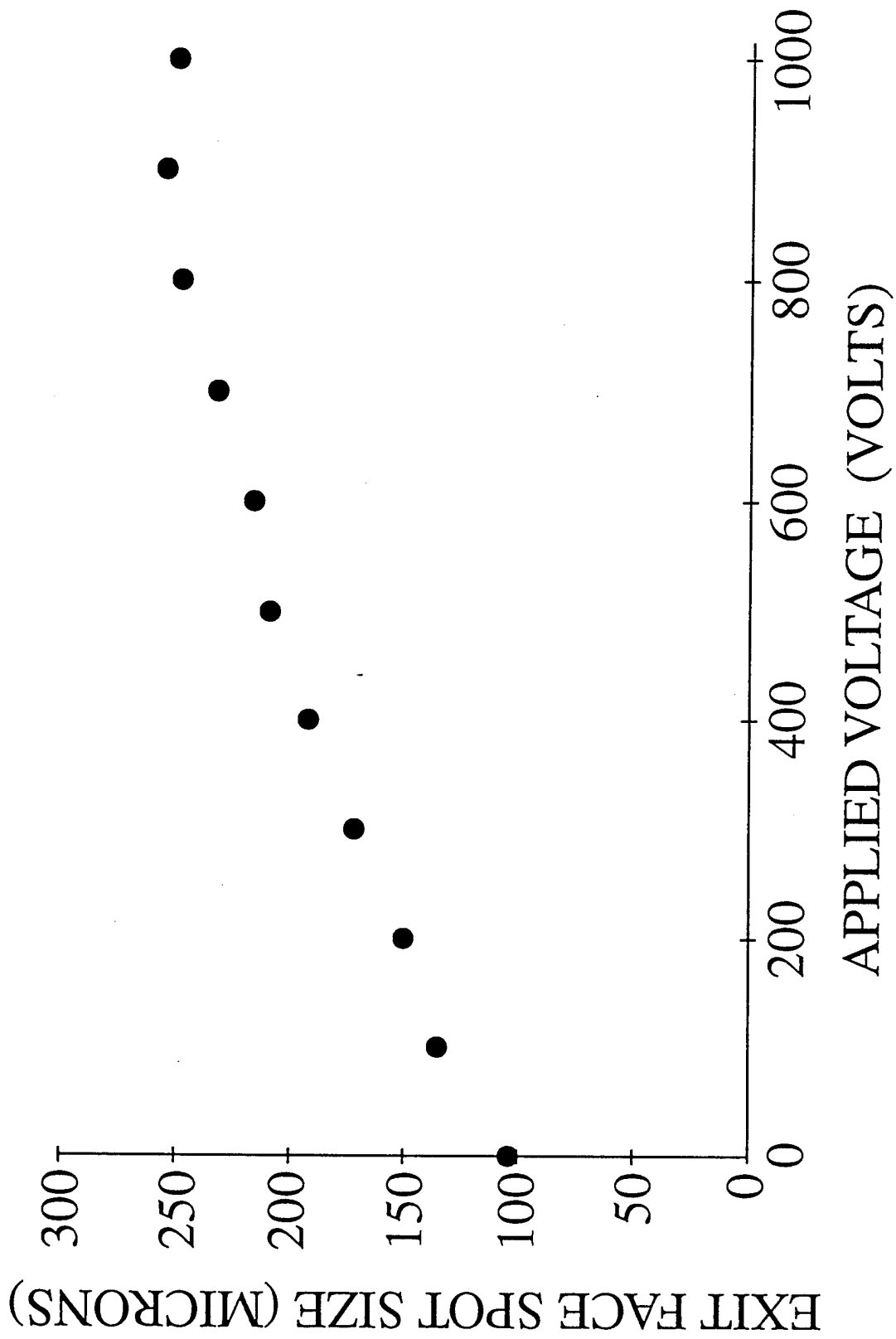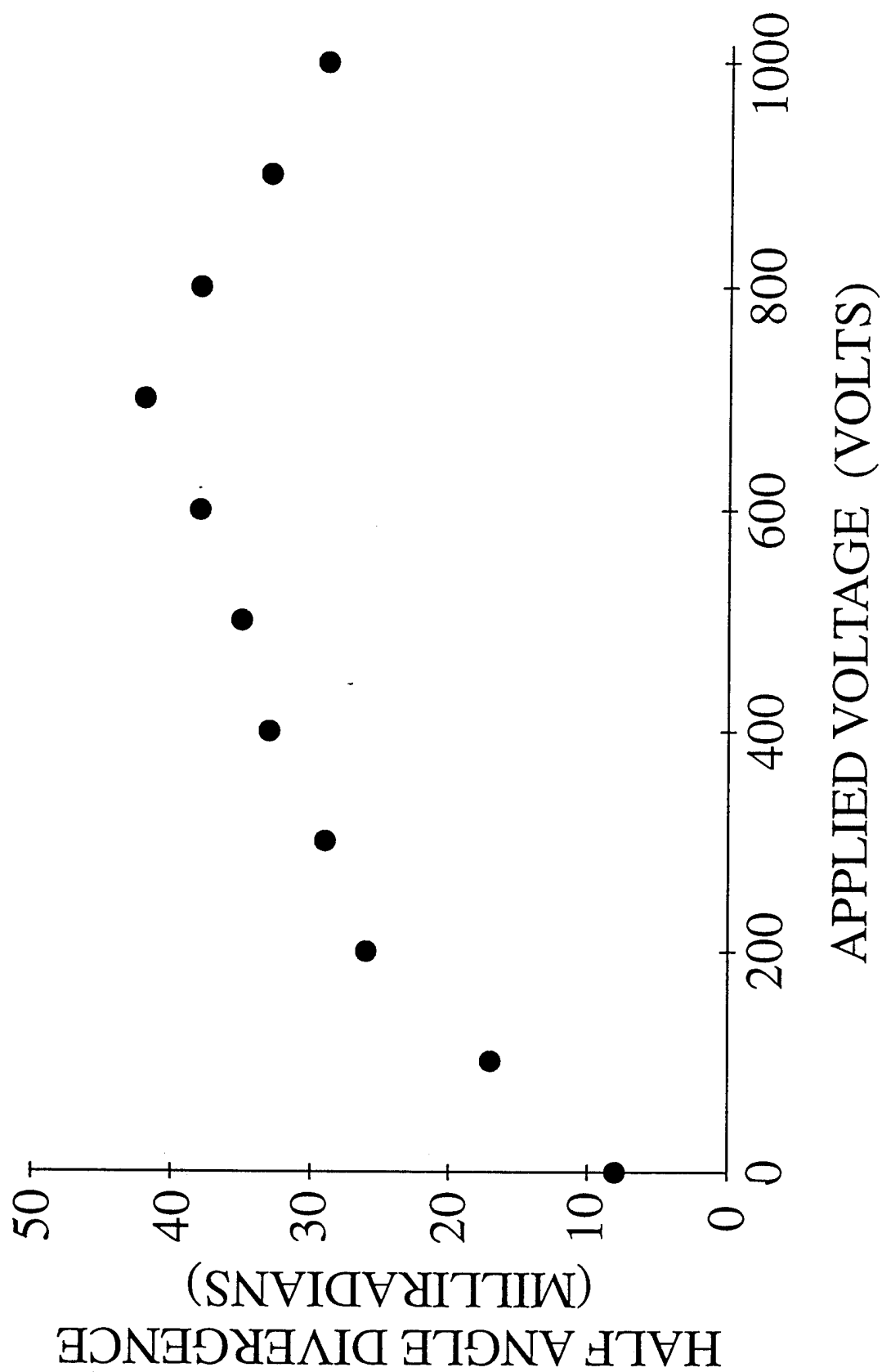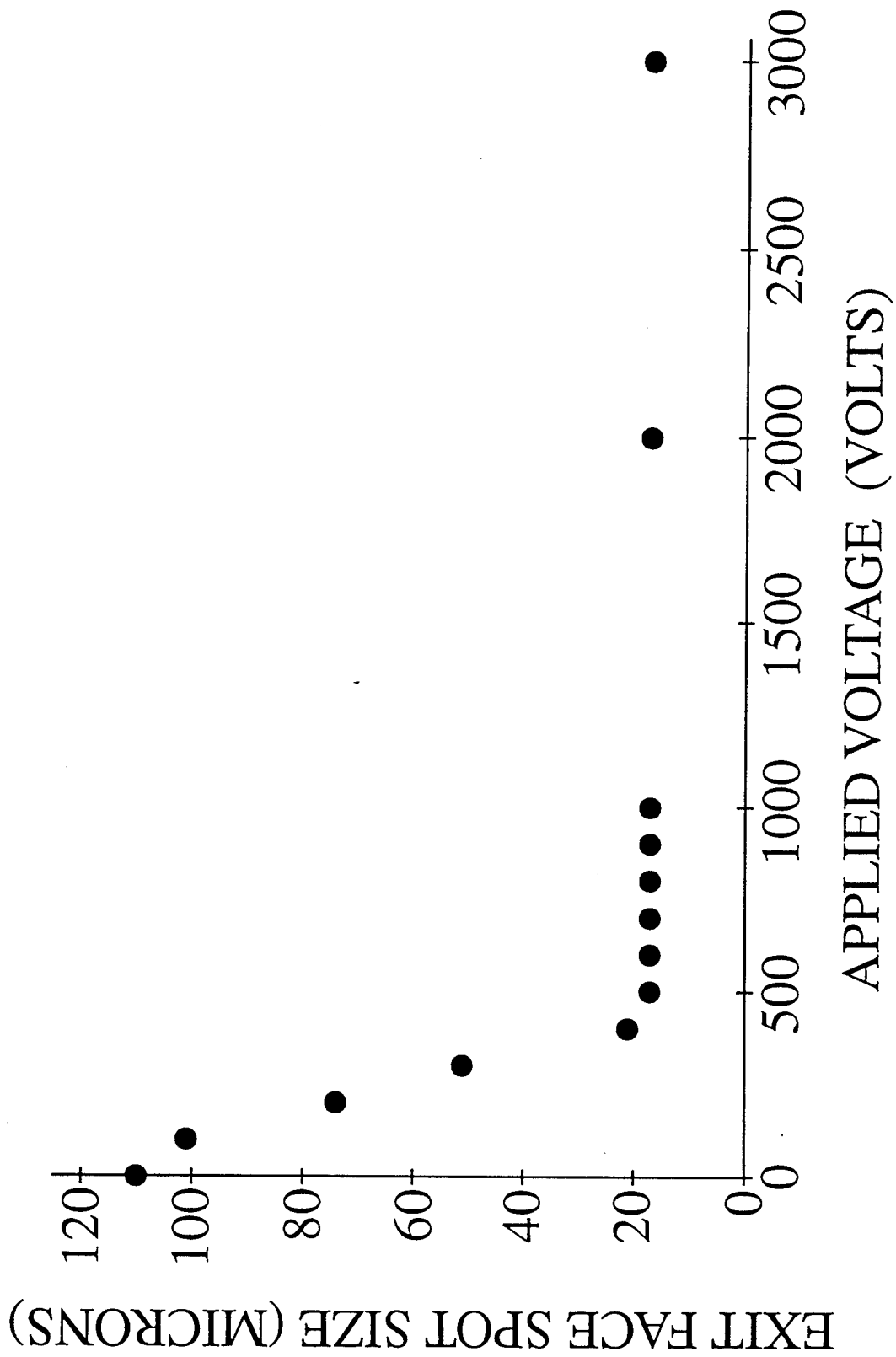
CONTROL OF N_A AND N_D

As has been pointed on numerous occasions in this report, control of N_A and N_D is important to the design of a photorefractive optical limiter. Variations in the response time and the O.D. and NA and ND are large. One potential technique for control of both of these variables is to use separate dopants in an attempt to control them independently. For this reason we have investigated the behavior of double-doped crystals. In particular, we have focused on the Cr-Mo combination. Four crystals were studied and the results are shown below.

Cr, Mo DATA

(a)   .01 Cr and .005 Mo

         $\alpha L \sim .66$

         $\tau \sim 1.68$ sec

         OD ~ 1.6

         all data at $1 W/CM^2$ at 4880A

(b)   .005 Cr and .01 Mo

         $\alpha L \sim .33$

         $\tau \sim 1.68$ sec

         OD ~ 1.3

         all data at $1 W/CM^2$ at 4880A

(c)   .005 Cr and .005 Mo

         $\alpha L \sim .33$

         $\tau \sim .8$ sec.

         OD ~ 1.2

         all data at $1 W/CM^2$ at 4880A

(d)   .01 Cr and .01 Mo

α L ~.55 (.65 for second cube)

τ ~ 1.7 sec.

OD ~ .3

all data at 1W/CM^2 at 4880A

The data from crystals (a), (b), and (c) supports the idea that only Cr controls the crystal absorption. That is Cr plays the role of N_D. For crystals (a) and (b) the Cr concentration changed by a factor of 2. Meanwhile the total dopant concentration remained constant. This indicates that Cr alone plays the role of the optical absorber. Likewise crystal (c) has the same Cr concentration as crystal (b). For these two crystals αL or the absorption was determined to be the same. These three crystals therefore offer strong support that Cr alone plays the role of N_D. Crystal (d) behaves more like a Cr concentration of .0075 and a Mo concentration of .0075. Perhaps this was tcut from a different boule location.

The same crystals also indicate that both Cr and Mo are playing the role of N_A. That is, the response time for both crystals (a) and (b) measure to be the same. This would be the case if the trap density were also the same in both crystals. Meanwhile crystal (c) has a clear faster response time. The total dopant concentration is less in this case than for crystal (a) or (b). Likewise the OD for crystal (c) is less than that for crystals (a) and (b) supporting a smaller N_A for crystal (c). The fourth crystal looks like a Cr, Mo concentration of .0075 each or a total again of .015.

The data from crystal (a), (b), (c), and (d) therefore support the idea that

-    Cr plays the role of N_D

-    Cr and Mo play the role of N_A

In addition to the double-doped samples we also examined the two types of dopants separately. For Mo alone we found for four samples:

(a)   .005 Mo

        $\alpha l \sim 3.2$

        $\tau \sim 1.2$ sec

        OD ~ 1.0

        All data at $1W/cm^2$ at 4880A

(b)   .01 Mo

        $\alpha l \sim 1.7$

        $\tau \sim 4$ sec

        OD ~ 1.6

        All data at $1W/cm^2$ at 4880A

(c)   .015

        $\alpha l \sim 2.9$

        $\tau \sim .228$ sec

        OD ~ 2.6

        All data at $1W/cm^2$

(d)   .015

        $\alpha l \sim 2.3$

        $\tau \sim 1.26$ sec

        OD ~ 2.3

        All data at $1W/cm^2$ at 4880A

(e)   .025

$\alpha l \sim 1.7$

$\tau \sim 1.98$ sec.

OD ~ 3

All data at $1W/cm^2$ at 4880A

(f)   .025

$\alpha l \sim 1.4$

$\tau \sim 2.35$ sec.

OD ~ 3

All data at $1W/cm^2$ at 4880A

While for Cr alone we found

(a)   .005 Cr

$\alpha L \sim .35$

$\tau \sim 2.6$ sec

OD ~ 1

all data at $1W/cm^2$ at 4880A

(b)   .01 Cr

$\alpha L \sim .69$

$\tau \sim 2.6$ sec

OD ~ 1.3

all data at $1W/cm^2$ at 4880A

(c)   .015 Cr

$\alpha L \sim .73$

$\tau \sim .390$ sec

$OD \sim 1$

all data at $1W/cm^2$ at 4880A

(d)   .025 Cr

$\alpha L \sim 1.2$

$\tau \sim .515$ sec

$OD \sim 1$

all data at $1W/cm^2$ at 4880A

(e)   .015 Cr

$\alpha L \sim .8$

$\tau \sim .375$ sec.

$OD \sim 1.3$

(f)   .025 Cr

$\alpha L \sim 2$

$\tau \sim .455$ sec.

$OD \sim 1$

That is, for Mo we have

Data from crystal (a), (b), (c), and (d) suggest that Mo plays the role of N_A. By increasing the concentration of Mo we increase the response time indicating that N_A is increasing. Meanwhile the αL is decreasing!. This would suggest that the higher concentration of Mo is lowering the N_D allowed in the crystal. The higher N_A value is also supported by a higher OD value for crystals with higher Mo concentration. It is also interesting that the ratio of αL for the two .015 crystals is 2.3/2.9 or .80 while the ratio of

144

the .025 crystals is 1.4/1.7 or .82. This suggest that the section from each boule is the same.

And for Cr we have

(a)   The ratio of dopants for the two samples is .015/.025 or .6

(b)   The ratio of response times for the two crystals is .39/.515 or .75

(c)   The ratio of absorption, αL, for the two crystals is .73/1.2 or .6

It would appear that both N_A and N_D change in proportion to the Cr concentration. This is consistent with our previous conclusion that the Cr concentration alone determined N_D while both Cr and Mo concentrations determine N_A. There is, however, a lower absorption the .015 Cr and .025 Cr crystals than the previous data for the double doped .005 and .01 Cr crystals suggested. This could easily be due to the difference in absorption through the boule. It would be good to always look at crystals taken from nearly the same location in the boule if this is not already the case.

Conclusion

There is substantial evidence that in the double doped Cr-Mo crystals that Cr plays the role of N_D the donor, while both Cr and Mo play the role of N_A, the acceptor. While the data is not 100% in support of this conclusion the evidence would warrant a additional measurements. This is the first time, to our knowledge, that control on N_A and N_D seems eminent.

The comparison of our data on the new crystals 18, 19, 20, &21 gives the following bottom line.

1.   Cr plays the role of N_D. Only Cr determines the absorption in the samples I have looked at.

2.   Both Cr and Mo play the role of N_A. both Cr and Mo determine the response time.

3.   The data supports the conclusion that when you compare the double dopant to the single dopant, the absorption is given directly by the absorption of Cr, i.e.

144a

$$\alpha_{Cr, Mo} = \alpha_{Cr}$$

4. The response time for the double dopant can be determined from the single dopant using the empirical relation

$$\frac{1}{\tau_{Cr,Mo}} = \frac{1}{\tau_{Cr}} + \frac{1}{\tau_{Mo}}$$

This last result works extremely well for the two cases I have looked at. That is, for

(Cr .005, Mo .005), (Cr .01, Mo .01) and (Cr .005), Mo (.005), and for (Cr .01), Mo (.01).

X. SEEDING THE BEAM FAN

In order to test the idea that the initial scattered light is weak and the cause of a slow start for the beam fanning phenomenon, we investigated the possibility of seeding the fanning with a more intense beam. Figure 10-1 depicts the seeding concept. A grating is placed in front of the photorefractive crystal. The incident laser beam now passes through the grating before entering the crystal. The incident beam on the grating is diffracted into several beams which propagate through the crystal while overlapping each other. Because of the overlap, gratings are written and energy is exchanged. If the grating chosen diffracts more light than normally found scattered in the non-grating case, the crystal can be said to be seeded. The data shown in Figure 10-2a,b is for a series of gratings of 1% diffraction efficiency. The observed enhancement in speed is a modest factor of 3. On the other hand, with a diffraction efficiency of 5%, Figure 2c, d, the enhancement in speed is more like 8 or 9. that is, it appears that by providing the crystal with a seed beam of greater intensity than that normally found via scattering by crystal imperfections, the response time for the optical limiting behavior of the crystal is dramatically shortened and brought more in line with that observed for two-beam coupling experiments.

In order to investigate the seeding effect more thoroughly the apparatus of Figure 10-3 was employed. In particular, instead of using a series of gratings to provide the seed beam, a weak seed beam is intentionally crossed in the crystal with the incident beam. The intensity of the seed beam was then controlled using simple neutral density filters. The crossing angle was controlled by changing the arrangement slightly. As seen in Figure 10-4a, for an input seed intensity of 1% no significant enhancement was observed. On the other hand, for seed intensities of 5, 10, and 20% an increasing enhancement was noted as seen in Figure 10-4a, b, c. In addition to an enhancement in speed it is also interesting to note that the transmission was nearly always more limited with the seed beam than without (Figure 10-50.

145

DISCUSSION

Energy depletion from one beam into the other beam in two-beam coupling experiments is described for $I_{01} \gg I_{02}$ by th expression

$$I_1(z) = \frac{I_1(0)(1+m)}{[1+m\exp(\Gamma z)]}$$

$$I_2(z) = \frac{I_2(0)(1+m)\exp(\Gamma z)}{[1+m\exp(\Gamma z)]}$$

10-1

where $I(0)$ is the incident intenstiy for beam 1 or 2, $I(z)$ is the intensity of beam 1 or 2 after propagation of a distance z in the crystal, Γ is the two-beam coupling gain coefficient, and m is the ratio

$$m = \frac{I_{02}}{I_{01}}$$

10-2

The gain coefficient for zero applied field is given by

$$\Gamma = \Gamma_o[1-\exp(-t/\tau)]$$

10-3

where

$$\Gamma_0 = \frac{2\pi r_{eff}k_B T k_g \cos(2\Theta)}{q\lambda n \cos\Theta\left[1+\frac{k_g^2}{k_0^2}\right]}$$

10-4

In this expression for Γ_0, q is the charge of thecarrier, r_{eff} is the effective electro-optic coefficient, k_g is the grating wave vector, λ is the laser light wavelength, Θ is the half-angle between the two crossing laser beams, and k_0 is the Debye screening wave vector given by

$$k_0^2 = \frac{q^2 N_{eff}}{k_B T \varepsilon}$$

10-5

In the expression for k_0^2, N_{eff} is the effective charge density, ε is the d.c. dielectric constant, and $k_B T$ is the thermal energy.

146

The response time for he formation of the two-beam coupling grating is given by the expression

$$\tau = \frac{1}{I_T} \left[\left(\frac{\varepsilon \hbar \omega}{\alpha q} \right) \left[\frac{1 + k_g^2}{k_0^2} \right]^{-1} \left(\frac{\gamma N_A}{\mu} + \frac{k_g^2 k_B T}{q} \right) \right] \qquad 10\text{-}6$$

where γ is the recombination rate coefficient, μ is thhe carrier mobility, N_A is the acceptor charge density, α is the absorption coefficient, and I_T is the total initial intensity.

As can be seen from expression (1) the change in intensity is dependent on the modulan index m. Since seeding can result in a higher modulation index than is normally present for beam fanning it can therefore produce a greater change in intensity via two beam coupling. This may explain the improved or higher depletion shown in Figure 10-5 when the beam fan is seeded.

Expression 10-3 describes the time behavior of two-beam energy coupling. The characteristic response time-is τ. As can be seen from expression 10-6, the response time has an intensity dependence which is inverse to the total intensity. Since seeding does not change the total intensity significantly a dramatic change in the beam fan time is not expected. For example, a 10% or 20% seed would not be expected to alter the response time by factors of 3 to 8. For this reason, the explanation for the improved response time most likely lies in the fact that the formation of the fan is through to evolve from gratings current. The addition of a seed beam of superior intensity perhaps encourages the energy exchange to take place more by the rules of two-beam coupling than by the more complex rules associated with beam fanning.

Conclusions

We have demonstrated that the speed of response for a beam fanning optical limiter can be enhanced by using a grating in front of the photorefractive crystal in order to seed the fanning effect. One possible extension of the work is to investigate the possibility of fabricating a grating right on the crystal entrance face.

INPUT LASER

GRATING

CRYSTAL

LASER LIGHT
THROUGH-PUT

1ST ORDER
INTENSITY
ENHANCEMENT

148

PUMP
BEAM

SEED
BEAM

VARIABLE θ

BEAM
SPLITTER

SBN
CRYSTAL

LENS

APERTURE DETECTOR

DIGITAL
OSCILLOSCOPE

150

(a)

$P_0 = 11.0$ mW
$\omega_0 = 1.15$ mm
$I_s = .01\, I_0$

$.0000494\, x^2 - .00198\, x + 1.06$

(b)

$P_0 = 11.0$ mW
$\omega_0 = 1.15$ mm
$I_s = .05\, I_0$

$-.00224\, x^2 + .117\, x + .192$

(c)

$P_0 = 11.0$ mW
$\omega_0 = 1.15$ mm
$I_s = .10\, I_0$

$-.00601\, x^2 + .325\, x - 1.836$

(d)

$P_0 = 10.0$ mW
$\omega_0 = 1.15$ mm
$I_s = .20\, I_0$

$-.0162\, x^2 + .871\, x - 4.56$

SEEDING ANGLE (degrees)

$\langle \tau_0 \rangle / \langle \tau_1 \text{ enhanced} \rangle$

TIME (sec)

TRANSMITTED INTENSITY (relative units)

152

XI. SUMMARY

Our investigations under this contract have proved to be very productive. We have:

1. Developed a limiter, using a cylindrical lens, with a 10^3 enhancement in speed. Using a 5 cm x 5 cm crystal this means that if the incident intensity is $1W/cm^2$ which normally produces a 0.1 second response time, the cylindrical technique gives a 100 microsecond response time. This can <u>now</u> be accomplished with an O.D. of 2 to 3.

2. We have investigated the effect of a D.C. electronic field on a photorefractive crystal. Using an applied field of about 6KV/cm we find an enhancement of a factor of 10 can be achieved. When coupled with the result of using a cylindrical lens the combination would give a 10 microsecond response time with an O.D. of 2 to 3.

3. We discovered that A.C. applied fields can cause speed enhancements on photorefractive SBN and BSKNN. We have, in fact, developed a physical understanding of the effect of A.C. fields in these crystals. The advantage of A.C. fields is that the screening effect accompanying D.C. fields is eliminated. We have both computer simulations and experimental data to support our understanding. The A.C. field can be used in combination with a spherical focusing lens system. The two together can yield an enhanced speed of 10^6. This means that for our incident intensity of $1W/cm^2$, on the 5 cm x 5 cm crystal, the 0.1 second response time can be reduced to 0.1 microseconds.

4. We developed a new technique to measure N_A. In this technique, two-beam coupling is used while we measure the phase angle between the intensity pattern and the space change field as a function of applied field. Our results were compared with the traditional two-beam coupling

153

technique of measuring coupling versus crossing angle. The comparison showed that both techniques give the same answer for N_A. However, our new technique is simpler and more accurate.

5. We examined writing versus reading times in photorefractive crystals. We found in our experiments that these times can be different. We also demonstrated that they are expected to be different using our photorefractive model. Papers which state that these two times are the same are simply wrong. Similar results were found for ordinary and extra ordinary polarization.

6. We examined the response time of our crystals versus intensity Interestingly, we found a strict 1/I dependence on the response time when the data was properly taken. This was true for several SBN crystals. BaT_iO_3 crystals will soon be tried as we showed a less than 1/I dependence indicating the presence of shallow traps.

7. We discovered and have characterized self defocusing and focusing by photorefractives. The defocusing effect in SBN is very strong, raising the divergence of the incident beam by 3-fold for a 1KV applied potential. This could be the basis of a "new limiter".

8. We have developed a limiting concept based on the quadradic electro-optic effect. In this case our results demonstrate a fast limiter without the D.C. screening effect. More data should be taken before these results are reported. Here again, a new limiting idea was discovered.

9. We have established that double dopant crystals do provide control over N_A and N_D. Our evidence is strong that for Cr, Mo doped crystals, Cr alone plays the role of N_D while both Cr and Mo play the role of N_A. Although the result is not the ideal case of one dopant acting as N_A and one as N_D, it is true that our results suggest that N_A can be varied

154

independently of N_D and that by changing only the Mo concentration, N_A can be forced to change while holding N_D fixed.

10. We have examined the role of temperature on the photorefractive response time. It is clear that both the O.D. and the reponse time are enhanced with higher temperature. More data must be taken using a combination of focusing, field, and temperature before a report is made.

11. We have developed a seeding method to increase the photorefractive response time by a factor of 5 to10 without loss of O.D.

We believe that the evidence is **strong** that an effective photorefractive limiter is **NOW**. The next step is to try a device for each "concept" investigated or demonstrated, and to compare with the needed response time and O.D. I would be happy to support any effort by the ARMY to construct a photorefractive optical limiter based on the results of our work.

Finally, we have three strong suggestions for device fabrication based on our studies. The first is to use a cylindrical lens, spherical lens combination. Consider an input beam 5 cm x 5 cm. A spherical lens system reduces the beam to .5 cm x .5 cm, while a cylindrical lens system takes the beam to .5 cm x 50 microns. The total reduction in area is 10^4. As a result the response time is 10^4 times faster! If we now apply a D.C. electric field, we can produce a 10^5 enhancement in speed. This device would not suffer from screening and would have a 2 to 3 O.D. This works TODAY, limiting at 6 uj/cm^2 with an O.D. of 3 to 4. In addition, seeding the beam fan could, in principle, bring improvement higher.

The second device is based on using a spherical lens system coupled with an A.C. electric field. Using the same parameters outlined above and a BSKNN crystal and 10^6 enhancement in speed is possible with an O.D. of 2 to 3. While this system is simpler than the cylindrical lens, the laboratory results were never as clean cut. However, it is promising and should be tried.

DEVICE CONCEPTS
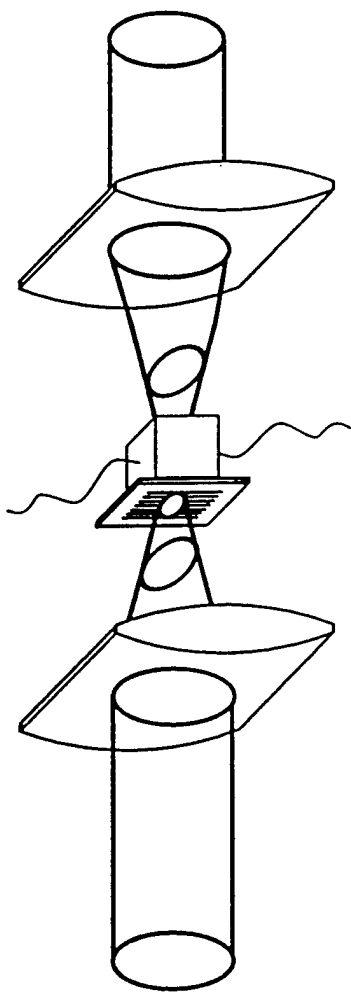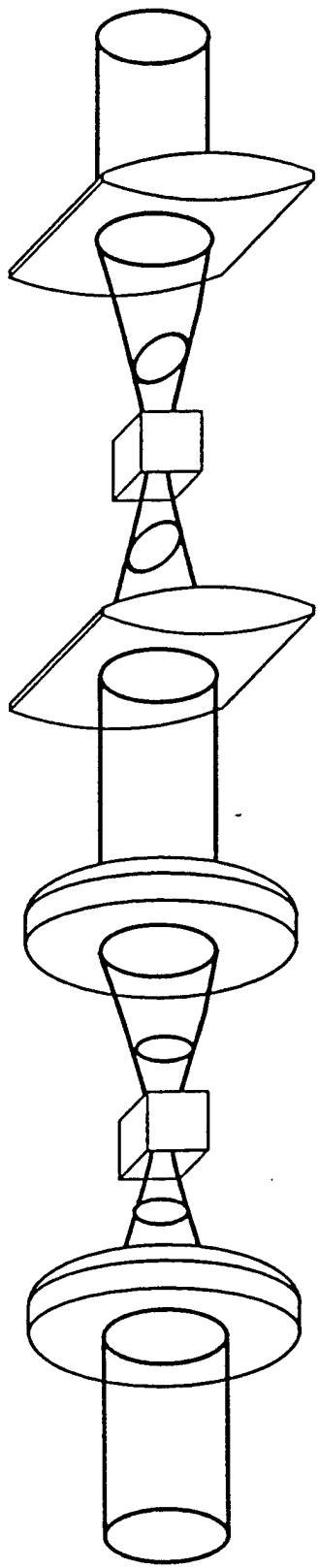
The third device is based on the quadradic electro-optics effect. We found exciting results using an A.C. square wave on a SBN sample with La doping. At room temperature, this sample was above but near the Curie temperature. The experimental results showed a modulated scattering or fanning phenomena that followed the temporal behavior of the driving field. This system protected effectively with spherical lens, except during the zero applied field periods of the cycle. However, a combination of two crystals, each at a different driving frequency, would illuminate this problem. Here, again we found a limiter with promise for today.

In addition to the 11 major results of our work it should be noted that at least 22 publications in major journals, 20 publications in proceedings, and about 40 talks at conferences were also among the achievements of the grant. Moreover, additional papers will be submitted over the next six months.

It should be noted that nearly all my work was carried out with the help of many of the scientists at the Night Vision Electro-optics Center part of which is now the Army Research Laboratory. I am grateful for the support, collaboration, and friendship of Ed Sharp, Gary Wood, Bill Clark, Mary Miller, and Byong Ahn. Of course none of my work would have been possible without the crystals, scientific expertise, and collaboration of R^2 Neurgaonkar. Also, I would like to add a special note of thanks to Wolfgang Elser and L. N. Durasula, who supported this work from beginning to end without hesitation.

XII. PUBLICATIONS (1990 - TO DATE)

Dark Photorefractive Solitons," G. Duree, G. Salamo, M. Segev and A. Yariv, accepted to **Physical Review Letters.**

"Optically Induced Ferroelectric Domain Gratings in the Galssy Polarizaiton Phase," A. Kewitsch, M. Segev, A. Yariv, T. Towe, and G. Salamo, **Physical Review Letters, 73**, 1174 (1994)

"Single Beam Photorefractive Rings in BSKNN," S. Montgomery, E. Sharp, G. Wood, and G. Salamo, **JOSA B, 11**, 1694 (1994).

"Tunable Quasi-Phase Matching Using Optically Induced Dynamic Polarization Gratings," A. Kewitsch, M. Segeve, A. Yariv, G.J. Salamo, T. Towe, E.J. Sharp, andR.R. Neurgaonkar, **Applied Physics Letters, 64**, 3068 (19940.

"Dimensionality and Size of Photorefractive Solitons," G. Duree, G.J. Salamo, M. Segev, A. Yariv, B. Crosignani, P.D. Porto, and E. Sharp, **Optics Letters,19**, 1195 (1994).

"Stability of Photorefractive Solitons," M. Segev, A. Yariv, G. Duree, G.J. Salamo, B. Crosignani, P.D. Porto, and E. Sharp, **Optics Letters,19**, 1196 (1994).

"Single Beam Polarization Holographic Grating Recording Using Photogalvanic-Photorefractive Crystals," N. Kukhtarev, G. Dovgalenko, G.C. Duree, Jr. and G. Salamo, **Physical Review Letters, 71**, 4330 (1993).

"The Observation of Self-Trapping of an Optical Beam due to the Photorefractive Effect," G. Duree, Jr., J. Shultz, G. Salamo, M. Segev, A. Yariv, B. Crosignani, P. Di Porto, E. Sharp and R.R. Neurgaonkar, **Physical Review Letters, 71**, 533 (1993).

"Manifestation of circular photogalvanic current by dynamic holography in $BaTiO_3$," N. Kukhtarev, G. Dovgalenko, and G. Salamo, **Applied Physics A, 56**, 303, (1993)

"Moving Object Correlator" R. Anderson, G. Wood, E. Sharp, R.R. Neurgaonkar and G. Salamo, **Optics Letters, 18**, 986 (1993).

"Reflection Holographic Gratings in [111] Cut, $Bi_{12}TiO_{20}$ Crystal for Real Time Interferometry," N. Kukhtarev, BoSu Chen, P. Venkateswarlu, M. Klein, and G. Salamo, **Optics Communications, 104**, 23 (1993).

"Self-Trapping of Optical Beams," Crosignani, Segev, Yariv, and G. Salamo, **JOSA B, 10**, 446, (1993).

"Enhancing the Photorefractive Effect," G. Duree, N. Bei, J. Shultz, G. Salamo, E. Sharp, and R.R. Neurgaonkar, **Optics Communications, 101**, 397 (1993).

"Growth and Optical Properties of Ferroelectric Tungsten Bronze Crystals", R.R. Neurgaonkar, W.K. Cory, J.R. Oliver, E.J. Sharp, G.L. Wood, G.J. Salamo, **Ferroelectrics, 142**, 167 (1993).

"Photorefractive Spatial Solitons", M. Segev, A. Yariv, G. Salamo, G. Duree, J. Shultz, B. Crosignani, P. Di Porto, and E. Sharp, **Optics and Photonics News**, December 1993, p. 9.

"Fluence Limiting Via Photorefractive Two-Beam Coupling," G. Wood, W.W. Clark, G. Salamo, A.G. Mott, and E. Sharp, **J. Appl. Phys.**, **71**, 37 (1992).

"Incoherent to Coherent Conversion Using a Photorefractive Self-Pumped Phase Conjugator," G. Salamo, B. Monson, W.W. Clark, E. Sharp and R. Neurgaonkar, **Opt. Lett.**, **17**, 207 (1992).

"Color Imaging in Photorefractive Crystals," S. Rabbani, J. Shultz, G. Salamo, E. Sharp, W. Clark III, M. Miller, G. Wood, and R. Neurgaonkar, **Applied Phys. B, 53**, (1991)

"Improved Photorefractive Time Response Using a Cylindrical Lens," G.J. Salamo, B. Monson, W.W. Clark III, G.L. Wood, E.J. Sharp, and R.R. Neurgaonkar, **Appl. Opt.**, **30**, 1847 (1991)

"Double Phase Conjugation in Tungsten Bronze Crystals", E. J. Sharp, W. W. Clark III, M. J. Miller, G. L. Wood, B. Monson, and G. J. Salamo, **Appl. Opt.** **29**, 743 (1990)

"Enhanced Photorefractive Effects Due to Static Electric Fields," W. Clark III, G. Wood, M. Miller, E. Sharp, and G. Salamo, **Appl. Opt. 29**, p. 1249 (1990).

"Self-Pumped Phase Conjugation with Nanosecond Pulses in Strantum Barium Niobate", B. Monson, G. J. Salamo, A. G. Mott, M. J. Miller, E. J. Sharp, W. W. Clark III, G. L. Wood, and R. R. Neurgaonkar, **Opt. Lett. 15**, 12 (1990).

XIII. PARTICIPATING SCIENTIFIC PERSONNEL

1. Mr. Galen Duree
    Ph.D., May 1995

2. Mr. Brian Monson
    Ph.D., May 1991

3. Mr. Nianyu Bei
    Ph.D., May 1995
    M.S., May 1993

4. Mr. Matt Morin
    M.S., May 1995

XIV. REPORT OF INVENTIONS

1.   Broard band, Multi-line, Optical Power Limiting Scheme
      Patent Number: 5,073,705
      Date of Patent: Dec. 17, 1991

2.   Mutually Pumped Phase Conjugator
      For Remote Identification
      Patent Number: 5,317,442
      Date of Patent: May 31, 1994

X V BIBLIOGRAPHY

Section 2

1. D. Pepper, et al, Sci. American, Oct, 62 (1990)

2. A. Ashkin, et al, Appl. Phys. Lett. 9, 72 (1966)

3. F. S. Chen, J. Appl. Phys. 38, 3418 (1967)

4. F. S. Chen, J. Appl. Phys. 40, 3389 (1969)

5. J. J. Amodei, Appl. Phys. Lett. 18, 22 (1971)

6. D. L. Staebler, et al, J. Appl. Phys. 43, 1042 (1972)

7. N. V. Kukhtarev, V. B. Markov.and S. G. Odolov, Opt. Comm. 23, 338 (1977)

8. N. V. Kukhtarev, V. B. Markov, S. G. Odolov, M. S. Soskin and V. L. Vinetskii,

    Ferroelectrics, 22, 949 and 961 (1979)

9. J. Feinberg, J. Opt. Soc. Am. 72, 46 (1982)

10. D. Pepper, et al, Sci. American, Oct, 62 (1990)

11. A. Marrakchi, et al, Opt. Comm. 34, 15 (1980)

12. George C. Valley and Marvin B. Klein, Opt. Eng. 22, 704 (1983)

13. George C. Valley, IEEE J. Quan. Elec. QE-19, 1637 (1983)

14. George C. Valley, J. Opt. Soc. Am. B 1, 868 (1984)

15. D. T. H. Liu, et al, Opt. Comm. 72, 384 (1989)

16. W. Clark III et al, Appl. Opt. 29, 1249 (1990)

17. K. Sayano, et al, Opt. Lett. 15, 9 (1990)

18. Galen C. Duree ., et al, Opt. Comm. 101, 397 (1993)

19. S. Stepanov, et al, Opt. Comm. 53, 292 (1985)

20. J. Kumar, et al, Opt. Lett. 12, 120 (1987)

21. X. Gan, et al, Opt. Comm. 66, 155 (1988)

22. M. Ziari, et al, J. Opt. Soc. Am. B 9, 1461 (1992)

23. J. Kumar, et al, J. Opt. Soc. Am. B 4, 1079 (1987)

24. A. G. Jepsen, et al, J. Opt. Soc. Am. B 11, 124 (1994)

Section 3

1. A. Yariv, in Quantum Electronics, Third Edition (John Wiley and Sons, New York, NY, 1989) Chap. 19, pp 516-527

2. N. V. Kukhtarev, et al, Ferroelectrics, 22, 1949 (1979)

3. George C. Valley and Marvin B. Klein, Opt. Eng. 22, 704 (1983)

4. George C. Valley, IEEE J. Quan. Elec. QE-19, 1637 (1983)

5. George C. Valley, J. Opt. Soc. Am. B 1, 868 (1984)

Section 4

1. D. L. Staebler, et al, J. Appl. Phys. 43, 1042 (1972)

2. N. V. Kukhtarev, et al, Ferroelectrics 22, 1949 (1979)

3. N. V. Kukhtarev, Sov. Tech. Phys. Lett. 2, 438 (1977)

4. George C. Valley, Appl. Opt. 22, 3160 (1983)

5. George C. Valley and Marvin B. Klein, Opt. Eng. 22, 704 (1983)

6. George C. Valley, IEEE J. Quan. Elec. QE-19, 1637 (1983)

7. J. P. Huignard and A. Marrakchi, Opt. Comm. 38, 249 (1981)

8. Galen C. Duree ., et al, Opt. Comm. 101, 397 (1993)

Section 5

1. S. Stepanov, et al, Opt. Comm. 53, 292 (1985)

2. A. P. Ghosh, et al, Opt. Comm. 72, 109 (1989)

3. K. Walsh, et al, J. Opt. Soc. Am. B 7, 288 (1990)

4. T. J. Hall, et al, at the Conference of Photorefractive Materials, Effects and Devices, Jan. 1990, Aussois, France

5. L. M. Bernardo, et al, in Nonlinear Optical Materials, p. 223 - 260

6. A. G. Jepsen, et al, J. Opt. Soc. Am. B 11, 124 (1994)

Section 6

1. R. Kapoor et al, Opt. Lett. Vol 8, No 9, May 1, (1993)

2. H. Kogelnik, Bell Syst. Tech. J. Vol 48, 6929 (1969)

3. R. A. Vazquez et al, JOSA B, Vol 9, 1416 (1992)

4. G. L. Wood et al, IEEE J Quan. Electro. Vol QE-23, 2126 (1987)

5. J. P. Wilde et al, Opt. Lett. Vol 17, 853 (1992)

6. F. P. Strohkendl et al, Opt. Lett. Vol 11, No 5, 312 (1986)

7. R. A. Fisher, in Optical Phase Conjugation, p. 433, Academic Press, New York, (1983)

Section 7

1. George C. Valley and Marvin B. Klein, Optical Engineering 22, 704 (1983)

2. S. Ducharme and J. Feinberg, J. Appl. Phys. $\underline{56}$, 839 (1984)

3. M. Ewbank et al, J. Appl. Phys. $\underline{62}$, 374 (1987)

4. D. Mahgerefteh and J. Feinberg, Opt. Lett. $\underline{13}$, 1111 (1988)

5. D. Mahgerefteh and J. Feinberg, Phys. Rev. Lett. $\underline{64}$, 2195 (1990)

6. G. Brost and R. Motes, Opt. Lett. $\underline{15}$, 1194 (1990)

Appendix I : Derivation of the Space-Charge Field

In this section, the steady-state and time-dependent solutions for the space-charge field will be derived from the linearized set of equations given by (2.6.a)-(2.6.h):

$$\frac{dN_0^+}{dt} = sI_0 (N_D - N_0^+) - \gamma_R n_{e0} N_0^+ \quad , \tag{I.1.a}$$

$$\frac{dN_1^+}{dt} = smI_0 (N_D - N_0^+) - sI_0 N_1^+ - \gamma_R (n_{e0} N_1^+ + n_{e1} N_0^+) \quad , \tag{I.1.b}$$

$$j_0 = q_e \mu_e n_{e0} E_0 \quad , \tag{I.1.c}$$

$$j_1 = q_e \mu_e (n_{e0} E_1 + n_{e1} E_0) + i\mu_e k_B T k_g n_{e1} \quad , \tag{I.1.d}$$

$$0 = \frac{dN_0^+}{dt} - \frac{dn_{e0}}{dt} \quad , \tag{I.1.e}$$

$$ik_g j_1 = -q_e \left(\frac{dN_1^+}{dt} - \frac{dn_{e1}}{dt} \right) , \tag{I.1.f}$$

$$0 = N_0^+ - n_{e0} - N_A \quad , \tag{I.1.g}$$

$$ik_g E_1 = \frac{q_e}{\varepsilon} (N_1^+ - n_{e1}) \quad . \tag{I.1.h}$$

First, an expression for n_{e1} must be obtained which eliminates N_1^+. Combining the time derivative of (I.1.h),

$$ik_g \frac{dE_1}{dt} = \frac{q_e}{\varepsilon} \left(\frac{dN_1^+}{dt} - \frac{dn_{e1}}{dt} \right) , \tag{I.2}$$

with (I.1.d) and (I.1.f), one obtains

166

$$\frac{dE_1}{dt} = -\frac{q_e \mu_e}{\varepsilon} (n_{e0} E_1 + n_{e1} E_0) - \frac{i\mu_e k_B T k_g n_{e1}}{\varepsilon} . \qquad (I.3)$$

Solving this for n_{e1} yields

$$n_{e1} = \frac{\dfrac{ik_g \varepsilon}{q_e}\dfrac{dE_1}{dt} + i\mu_e k_g n_{e0} E_1}{\dfrac{1}{\tau_D} - \dfrac{i}{\tau_E}} , \qquad (I.4)$$

where the time constants in (I.4) are defined as

$$\tau_D \equiv \text{mean diffusion time} = \frac{q_e}{\mu_e k_B T k_g^2} , \qquad (I.5.a)$$

$$\tau_E \equiv \text{mean drift time} = \frac{1}{\mu_e k_g E_0} . \qquad (I.5.b)$$

Assuming n_{e0} to be constant, the time derivative of (I.4) is given by

$$\frac{dn_{e1}}{dt} = \frac{\dfrac{ik_g \varepsilon}{q_e}\dfrac{d^2 E_1}{dt^2} + i\mu_e k_g n_{e0}\dfrac{dE_1}{dt}}{\dfrac{1}{\tau_D} - \dfrac{i}{\tau_E}} . \qquad (I.6)$$

At this point, (I.1.b) and (I.6) can be substituted into (I.2) to obtain an expression involving N_1^+ and n_{e1} and time derivatives of E_1:

$$smI_0(N_D - N_0^+) - sI_0 N_1^+ - \gamma_R(n_{e0} N_1^+ + n_{e1} N_0^+) = \frac{\dfrac{ik_g \varepsilon}{q_e}\dfrac{d^2 E_1}{dt^2} + i\mu_e k_g n_{e0}\dfrac{dE_1}{dt}}{\dfrac{1}{\tau_D} - \dfrac{i}{\tau_E}} + \frac{ik_g \varepsilon}{q_e}\frac{dE_1}{dt} . \qquad (I.7)$$

Using (I.1.h) and (I.4) to eliminate N_1^+ and n_{e1} from (I.7) results in the following second-order differential equation for E_1:

167

$$\frac{d^2E_1}{dt^2} + \left(\frac{1}{\tau_+} + \frac{1}{\tau_{di}} + \frac{1}{\tau_D} - \frac{i}{\tau_E}\right)\frac{dE_1}{dt} + \left(\frac{1}{\tau_+\tau_{di}} + \frac{1}{\tau_I\tau_D} - \frac{i}{\tau_I\tau_E}\right)E_1 = \frac{q_e}{ik_g\varepsilon}\left(\frac{1}{\tau_D} - \frac{i}{\tau_E}\right)smI_0(N_D - n_{e0} - N_A) \qquad (I.8)$$

where the time constants in (I.8) are

$$\tau_{di} \equiv \text{dielectric relaxation time } = \frac{\varepsilon}{q_e\mu_e n_{e0}} \ , \qquad (I.8.a)$$

$$\tau_I \equiv \text{excitation time } = \frac{1}{sI_0 + \gamma_R n_{e0}} \ , \qquad (I.8.b)$$

$$\tau_+ \equiv \frac{1}{sI_0 + 2\gamma_R n_{e0} + \gamma_R N_A} \ . \qquad (I.8.c)$$

Since n_{e0} is constant, (I.1.a) and (I.1.e) can be used to obtain the following:

$$sI_0(N_D - N_0^+) - \gamma_R n_{e0}N_0^+ = \frac{dN_0^+}{dt} = \frac{dn_{e0}}{dt} = 0 \ . \qquad (I.9)$$

Assuming $N_A \gg n_{e0}$ for low irradiances, the resulting expression for n_{e0} is

$$n_{e0} = \frac{sI_0(N_D - N_A)}{\gamma_R N_A} \ . \qquad (I.10)$$

At equilibrium, the time derivatives in (I.8) vanish. Hence, the steady-state expression for E_1 is given by

$$E_1^{ss} = \frac{\dfrac{q_e}{ik_g\varepsilon}\left(\dfrac{1}{\tau_D} - \dfrac{i}{\tau_E}\right)smI_0(N_D - n_{e0} - N_A)}{\left(\dfrac{1}{\tau_+\tau_{di}} + \dfrac{1}{\tau_I\tau_D} - \dfrac{i}{\tau_I\tau_E}\right)} \ . \qquad (I.11)$$

For low irradiances ($N_A \gg n_{e0}$ and $\gamma_R N_A \gg sI_0$), (I.11) can be simplified to

$$E_1^{ss} = mE_N\left[\frac{E_D + iE_0}{E_0 + i(E_D + E_N)}\right] \ , \qquad (I.12)$$

168

where E_D and E_N are defined as

$$E_D = \frac{k_B T k_g}{q_e} ,$$

(I.13.a)

$$E_N = \frac{q_e N_{eff}}{k_g \varepsilon} = \frac{q_e N_A}{k_g \varepsilon} \left(1 + \frac{N_A}{N_D - N_A} \right)^{-1} .$$

(I.13.b)

Note that (I.12) can be written in the form

$$E_1^{ss} = m E_{sc} e^{i\phi} ,$$

(I.14)

where the amplitude, E_{sc}, and the phase shift, ϕ, are given by

$$E_{sc} = E_N \sqrt{\frac{E_D^2 + E_0^2}{(E_N + E_D)^2 + E_0^2}} ,$$

(I.15.a)

$$\tan\phi = \frac{E_D}{E_0} \left(1 + \frac{E_D}{E_N} + \frac{E_0^2}{E_D E_N} \right) .$$

(I.15.b)

The transient character of E_1 is found by solving the homogeneous form of (I.8). This can be written as

$$\frac{d^2 E_1}{dt^2} + \frac{1}{T_1} \frac{dE_1}{dt} + \frac{1}{T_2^2} E_1 = 0 ,$$

(I.16)

where T_1 and T_2 are defined by

$$\frac{1}{T_1} = \frac{1}{\tau_+} + \frac{1}{\tau_{di}} + \frac{1}{\tau_D} - \frac{i}{\tau_E} ,$$

(I.17.a)

$$\frac{1}{T_2^2} = \frac{1}{\tau_+ \tau_{di}} + \frac{1}{\tau_I \tau_D} - \frac{i}{\tau_I \tau_E} .$$

(I.17.b)

The complex quantities τ_a and τ_b can be defined such that

$$\frac{1}{T_1} = \frac{1}{\tau_a} + \frac{1}{\tau_b} , \qquad\qquad\qquad\text{(I.18.a)}$$

$$\frac{1}{T_2^2} = \frac{1}{\tau_a} \cdot \frac{1}{\tau_b} . \qquad\qquad\qquad\text{(I.18.b)}$$

The solution to (I.16) then takes the form

$$E_1(t) = E_1^{ss} + A e^{-t/\tau_a} + B e^{-t/\tau_b} , \qquad\qquad\text{(I.19)}$$

where A and B are constants to be determined by initial conditions. By assuming $\tau_+ \ll \tau_{di}$, $\tau_+ \ll \tau_D$ and $\tau_+ \ll \tau_I$, (I.18.a)-(I.18.b) can be solved for τ_a and τ_b in terms of T_1 and T_2:

$$\frac{1}{\tau_a} \approx \frac{T_1}{T_2^2} , \qquad\qquad\qquad\text{(I.20.a)}$$

$$\frac{1}{\tau_b} \approx \frac{1}{T_1} . \qquad\qquad\qquad\text{(I.20.b)}$$

Since $Re(1/\tau_a) \ll Re(1/\tau_b)$. the term in (I.19) involving τ_b can then be neglected since it decays much faster than the term involving τ_a. Thus, (I.19) becomes

$$E_1(t) = E_1^{ss} + A e^{-t/\tau_a} . \qquad\qquad\text{(I.21)}$$

The real quantities τ and ω can now be defined such that

$$\frac{1}{\tau_a} = \frac{1}{\tau} + i\omega . \qquad\qquad\qquad\text{(I.22)}$$

Using (I.17.a)-(I.17.b), the following expressions for τ and ω are obtained:

$$\frac{1}{\tau} = Re\left(\frac{T_1}{T_2^2}\right) = \frac{1}{\tau_{di}} \cdot \frac{\left(1 + \frac{\tau_+ \tau_{di}}{\tau_I \tau_D}\right)\left(1 + \frac{\tau_+}{\tau_D} + \frac{\tau_+}{\tau_{di}}\right) + \frac{\tau_{di}}{\tau_I}\left(\frac{\tau_+}{\tau_E}\right)^2}{\left(1 + \frac{\tau_+}{\tau_D} + \frac{\tau_+}{\tau_{di}}\right)^2 + \left(\frac{\tau_+}{\tau_E}\right)^2} , \qquad \text{(I.23.a)}$$

$$\omega = Im\left(\frac{T_1}{T_2^2}\right) = \frac{1}{\tau_{di}} \cdot \frac{-\left(\frac{\tau_+}{\tau_E}\right)\left(\frac{\tau_{di}}{\tau_I} - 1\right)}{\left(1 + \frac{\tau_+}{\tau_D} + \frac{\tau_+}{\tau_{di}}\right)^2 + \left(\frac{\tau_+}{\tau_E}\right)^2} . \qquad \text{(I.23.b)}$$

This initial value problem is completed by determining the constant A in (I.21). If no gratings exist in the photorefractive material at time $t = 0$, then the initial condition is $E_1(0) = 0$, so the time-dependent form of the space-charge field is given by

$$E_1(t) = E_1^{ss}[1 - e^{-t/\tau}e^{-i\omega t}] , \qquad \text{(I.24)}$$

where τ and ω are given by (I.23.a)-(I.23.b), respectively.

APPENDIX I-B

DERIVATION OF EQUATION (4-8)

The two waves R and S (reference and signal waves respectively) intersect in the volume of the real time holographic medium. The amplitudes of two waves are deduced as

$$dR/dz = -\chi_0 S \qquad\qquad (I\text{-}1)$$

$$dS/dz = \chi_0 R \qquad\qquad (I\text{-}2)$$

where $\chi_0 = m\pi\Delta n\sin\varphi/(\lambda\cos\theta)$ with $m = 2RS/(R^2 + S^2)$ is the corresponding beam coupling constant. $R(0) = R_0$, $S(0) = S_0$ are the boundary conditions.

By introducing $\Gamma = 4\pi\Delta n\sin\varphi/(\lambda\cos\theta)$ and substituting the expression of m into eq. (I-1) and (I-2) we obtain

$$dR/dz = -(1/2)\Gamma RS^2/(R^2 + S^2) \qquad\qquad (I\text{--}3)$$

$$dS/dz = (1/2)\Gamma R^2 S/(R^2 + S^2) \qquad\qquad (I\text{--}4)$$

We have $I_R = R^2$, $I_S = S^2$ and $R^2 + S^2 = R_0^2 + S_0^2$.

Therefore, the R and S amplitudes satisfy to the equations:

$$dR/dz = -(1/2)\Gamma R + (\Gamma/2)R^3/(R_0^2 + S_0^2) \qquad (I\text{--}5)$$

$$dS/dz = (1/2)\Gamma S - (\Gamma/2)S^3/(R_0^2 + S_0^2) \qquad (I\text{--}6)$$

The waves intensities emerging from the material ($z=L_{eff}$) and solutions of eq. (I-5) and (I-6) are given by

$$I_S = I_{S0}(R_0^2 + S_0^2)/[R_0^2 + S_0^2\exp(\Gamma L_{eff})] \qquad (I\text{-}7)$$

172

$$I_R = I_{R0}(R_0^2 + S_0^2)/[R_0^2 + S_0^2 \exp(\Gamma L_{eff})] \qquad (I\text{-}8)$$

If I_{1c} and I_1 are transmitted intensities of the signal beam with and without coupling, respectively, then signal beam (suppose it is a weak beam), I_1 will experience an increase in intensity given by

$$I_{1c}/I_1 = (I_S \text{ with reference beam })/(I_S \text{ without reference beam })$$

$$= (R_0^2 + S_0^2)\exp(\Gamma L_{eff})/[R_0^2 + S_0^2 \exp(\Gamma L_{eff})]$$

$$= (1 + c)\exp(\Gamma L_{eff})/[1 + c\exp(\Gamma L_{eff})]$$

with $c = S_0^2/R_0^2$. This is eq. (4-8) used in Chapter 4.

APPENDIX II

ANALYTICAL SOLUTION FOR SPACE-CHARGE FIELD WITH

AN APPLIED SQUARE WAVE AC FIELD

Using

$$\frac{\partial^2 E_1}{\partial t^2} + \frac{1}{T_1}\frac{\partial E_1}{\partial t} + \frac{1}{T_2^2} E_1 = c$$

$$1/T_1 = A_1 + iA_2 E_0$$

$$1/T_2^2 = B_1 + iB_2 E_0$$

$$c = i(C_1 + iC_2 E_0) = -C_2 E_0 + iC_1$$

where A_1, A_2, B_1, B_2, C_1, and C_2 are real numbers.

Then

$$-T_1/(T_2^2) = -(B_1 + iB_2 E_0)/(A_1 + iA_2 E_0)$$

$$= -[(A_1 B_1 + A_2 B_2 E_0^2) + iE_0(-A_2 B_1 + A_1 B_2)]/(A_1^2 + A_2^2 E_0^2)$$

$$= -1/\tau - i\omega$$

$$T_2^2 c = (-C_2 E_0 + iC_1)/(B_1 + iB_2 E_0)$$

$$= [(-B_1 C_2 + C_1 B_2) E_0 + i(B_1 C_1 + B_2 C_2 E_0^2)]/(B_1^2 + B_2^2 E_0^2)$$

$$= E_{sc}(\cos\varphi + i\sin\varphi)$$

$$= E_{sc} e^{i\varphi} \qquad\qquad (\text{II-1})$$

$$\varphi = \tan^{-1}\{(B_1 C_1 + B_2 C_2 E_0^2)/[(-B_1 C_2 + C_1 B_2) E_0]\} \qquad (\text{II-2})$$

174

Introduce a non-dimension physical quantity $E_1'(t)$ as

$$E_1(t) = E_{sc}E_1'(t)$$

If we apply a square-wave AC field across the crystal the amplitude and period of which are E_0 and T, respectively, the E_1' in the end of the first half period would be

$$E_1'(t = T/2) = -e^{i\varphi}e^{-T/(2\tau)}e^{-i\omega T/2} + e^{i\varphi} \qquad (\text{II-3})$$

During 2nd half period ($T/2 < t \leq T$), the applied field is $-E_0$. So now

$$T_2^2 c = [(-B_1C_2 + C_1B_2)(-E_0) + i(B_1C_1 + B_2C_2E_0^2)] / (B_1^2 + B_2^2E_0^2)$$

$$= E_{sc}(-\cos\varphi + i\sin\varphi)$$

$$= -E_{sc} \cdot e^{-i\varphi}$$

$$-T_1 / (T_2^2) = -(B_1 - iB_2E_0) / (A_1 - iA_2E_0)$$

$$= -[(A_1B_1 + A_2B_2E_0^2) - iE_0(-A_2B_1 + A_1B_2)] / (A_1^2 + A_2^2E_0^2)$$

$$= -1/\tau + i\omega$$

Then the solution is

$$E_1'(t) = [E_1'(t = T/2) + e^{-i\varphi}] \cdot e^{-(t-T/2)/\tau} \cdot e^{i\omega(t-T/2)} - e^{-i\varphi}$$

$$= [-e^{i\varphi}e^{-T/(2\tau)}e^{-i\omega T/2} + e^{i\varphi} + e^{-i\varphi}] \cdot e^{-(t-T/2)/\tau} \cdot e^{i\omega(t-T/2)} - e^{-i\varphi} \qquad (T/2 < t \leq T)$$

Thus

$$E_1'(t = T) = -e^{i\varphi}e^{-T/\tau} + e^{i\varphi} \cdot e^{-T/(2\tau)} \cdot e^{i\omega T/2} + e^{-i\varphi} \cdot e^{-T/2\tau} \cdot e^{i\omega T/2} - e^{-i\varphi}$$

By using the same procedure as above, we can get

$$E_1'(t = 3T/2) = -e^{i\varphi}e^{-3T/(2\tau)}e^{-i\omega T/2} + e^{i\varphi}e^{-T/\tau} + e^{-i\varphi}e^{-T/\tau} - e^{-i\varphi}e^{-T/(2\tau)}e^{-i\omega T/2}$$

$$- e^{i\varphi}e^{-T/2\tau}e^{-i\omega T/2} + e^{i\varphi}$$

175

$$E_1' (t = 2T) = -e^{i\varphi} e^{-2T/\tau} + e^{i\varphi} e^{-3T/2\tau} e^{i\omega T/2} + e^{-i\varphi} e^{-3T/2\tau} e^{i\omega T/2} - e^{-i\varphi} e^{-T/\tau} - e^{i\varphi} e^{-T/\tau}$$

$$+ e^{i\varphi} e^{-T/2\tau} e^{i\omega T/2} + e^{-i\varphi} e^{-T/2\tau} e^{i\omega T/2} - e^{-i\varphi}$$

$$E_1' (t = 5T/2) = -e^{i\varphi} e^{-5T/2\tau} e^{-i\omega T/2} + e^{i\varphi} e^{-4T/2\tau} + e^{-i\varphi} e^{-4T/2\tau} - e^{-i\varphi} e^{-3T/2\tau} e^{-i\omega T/2}$$

$$- e^{i\varphi} e^{-3T/2\tau} e^{-i\omega T/2} + e^{i\varphi} e^{-2T/2\tau} + e^{-i\varphi} e^{-2T/2\tau} - e^{-i\varphi} e^{-T/2\tau} e^{-i\omega T/2}$$

$$- e^{i\varphi} e^{-T/2\tau} e^{-i\omega T/2} + e^{i\varphi}$$

. . . .

Now we want to find the recurrence in the expression of E_1' (nT) (n is a positive

integer). Look at E_1' (2T) and rewrite the expression as

$$E_1' (t = 2T) = -e^{i\varphi} e^{-T/\tau} (1 + e^{-T/\tau}) + e^{i\varphi} e^{i\omega T/2} e^{-T/2\tau} (1 + e^{-T/\tau}) - e^{-i\varphi} (1 + e^{-T/\tau})$$

$$+ e^{-i\varphi} \cdot e^{i\omega T/2} \cdot e^{-T/2\tau} (1 + e^{-T/\tau})$$

From this, we can derive an expression for E_1' as t = nT, which is

$$E_1' (t = nT) = [1 + e^{-T/\tau} + e^{-2T/\tau} + \cdots\cdots\cdots + e^{-(n-1)T/\tau}] \cdot (-e^{i\varphi} e^{-T/\tau} + e^{i\varphi} \cdot e^{i\omega T/2}$$

$$\cdot e^{-T/2\tau} - e^{-i\varphi} + e^{-i\varphi} \cdot e^{i\omega T/2} \cdot e^{-T/2\tau})$$

$$= (1 - e^{-nT/\tau}) / (1 - e^{-T/\tau}) \cdot (-e^{i\varphi} e^{-T/\tau} + e^{i\varphi} \cdot e^{i\omega T/2} \cdot e^{-T/2\tau} - e^{-i\varphi}$$

$$+ e^{-i\varphi} \cdot e^{i\omega T/2} \cdot e^{-T/2\tau})$$

$$(n = 0, 1, 2, \ldots\ldots) \qquad\qquad\qquad (\text{II-4})$$

Next let's look at E_1' (t = 5/2T) and rewrite it as

$$E_1' (t = 5T/2) = e^{i\varphi} (1 + e^{-T/\tau} + e^{-2T/\tau}) - e^{i\varphi} e^{i\omega T/2} e^{-T/2\tau} (1 + e^{-T/\tau} + e^{-2T/\tau}) +$$

$$e^{-i\varphi} e^{-T/\tau} \cdot (1 + e^{-T/\tau}) - e^{-i\varphi} e^{-i\omega T/2} e^{-T/2\tau} (1 + e^{-T/\tau})$$

$$= (1 + e^{-T/\tau} + e^{-2T/\tau}) (e^{i\varphi} - e^{i\varphi} e^{-i\omega T/2} e^{-T/2\tau}) + (1 + e^{-T/\tau})$$

$$(e^{-i\varphi} e^{-T/\tau} - e^{-i\varphi} e^{-i\omega T/2} e^{-T/2\tau})$$

176

Also, from this, we can predict the expression for $E_1{}'$ as $t = (n + 1/2) T$,

which is

$$E_1{}' (t = (n + 1/2) T) = [1 + e^{-T/\tau} + e^{-2T/\tau} + \cdots\cdots\cdots + e^{-nT/\tau}] \cdot (e^{i\varphi} -$$

$$e^{i\varphi} e^{-i\omega T/2} \cdot e^{-T/2\tau}) + [1 + e^{-T/\tau} + e^{-2T/\tau} + \cdots\cdots\cdots +$$

$$e^{-(n-1)T/\tau}] \cdot (e^{-i\varphi} e^{-T/\tau} - e^{-i\varphi} e^{-i\omega T/2} e^{-T/2\tau})$$

$$= (1 - e^{-(n+1)T/\tau}) / (1 - e^{-T/\tau}) \cdot (e^{i\varphi} - e^{i\varphi} e^{-i\omega T/2} e^{-T/2\tau})$$

$$+ (1 - e^{-nT/\tau}) / (1 - e^{-T/\tau}) \cdot (e^{-i\varphi} e^{-T/\tau} - e^{-i\varphi} e^{-i\omega T/2} e^{-T/2\tau})$$

$$(n = 0, 1, 2, \ldots\ldots) \qquad\qquad (\text{II-5})$$

Eq. (II-4) & (II-5) are the basic equations (5-1) & (5-2) in Chapter 5.

APPENDIX III

DERIVATION OF EQUATION FOR PHASE SHIFT MEASUREMENT

Two laser beams with ordinary polarization and equal intensity I_0 intersect inside a crystal, which results in an energy exchange signal I_ε and a diffraction signal I_d.

The diffraction efficiency η is given by (Ref. [1], [2])

$$\eta = I_d / I_0 = \sin^2(\kappa d) \qquad\qquad\qquad (\text{III-1})$$

where κ is the coupling constant and d is the thickness of the crystal.

According to Ref.[7], both the real and imaginary part of the space-charge field contribute to the diffraction efficiency. Therefore, κ in eq. (III-1) is given by (Ref. [1], [2], [7])

$$\kappa = \pi \cdot \Delta n / \lambda \cos\theta \quad -$$

$$= (\pi/2\lambda \cos\theta)(n_0^3 r_{eff})[(ReE_{sc})^2 + (ImE_{sc})^2]^{1/2} \qquad (\text{III-2})$$

where ReE_{sc} and ImE_{sc} are real and imaginary part of the space-charge field, respectively. If we write

$$c = (\pi/2\lambda \cos\theta)(n_0^3 r_{eff}) \qquad\qquad\qquad (\text{III-3})$$

Then from eq. (III-1) and (III-2) we can obtain

$$[(ReE_{sc})^2 + (ImE_{sc})^2]^{1/2} = (1/c \cdot d)[\sin^{-1}(\eta^{1/2})] \qquad (\text{III-4})$$

In other hand, the energy-exchange efficiency is (Ref. [1])

$$\varepsilon = I_\varepsilon / I_0$$

The gain of the detected beam is governed by the equation (Ref. [1] and Appendix I)

$$(I_0+I_\varepsilon)/ I_0 = 1+\varepsilon = (1+1)e^{\Gamma d}/(1+e^{\Gamma d}) \qquad (\text{III-5})$$

where Γ is the gain coefficient, which is only due to the imaginary part of the space-charge field (Ref. [7]). Γ is given by (Ref. [4])

$$\Gamma = (2\pi/\lambda \cos\theta)(n_0^3 r_{eff})(ImE_{sc})$$

By using eq. (III-3) Γ becomes

$$\Gamma = 4c(ImE_{sc}) \qquad (\text{III-6})$$

By substituting eq. (III-6) into eq. (III-5), we can obtain

$$ImE_{sc} = (1/4)(1/c \cdot d) \cdot \ln[(1+\varepsilon)/(1-\varepsilon)] \qquad (\text{III-7})$$

The phase shift φ between the grating and the fringe pattern is determined by the equation

$$\tan\varphi = ImE_{sc}/ ReE_{sc}$$

Therefore, by using eq. (III-4) and (III-7) we will get

$$\sin\varphi = \tan\varphi/(1+\tan^2\varphi)^{1/2}$$

$$= ImE_{sc}/[(ReE_{sc})^2+(ImE_{sc})^2]^{1/2}$$

$$= \ln[(1+\varepsilon)/(1-\varepsilon)]/[4\sin^{-1}(\eta^{1/2})] \qquad (\text{III-8})$$

For small coupling which is the case in our experiment, both η and ε are much less than 1. So mathematically, by using Taylor expansion, we can get

$$\ln[(1+\varepsilon)/(1-\varepsilon)] \cong 2\varepsilon \quad \text{for } \varepsilon<1$$

and
$$\sin^{-1}(\eta^{1/2}) \cong \eta^{1/2} \qquad \text{for } \eta<1 \qquad (\text{III-9})$$

By substituting eq. (III-9) into eq. (III-8), we obtain

$$\sin\varphi = \varepsilon/2\eta^{1/2}$$

$$= (I_\varepsilon/I_0)/2(I_d/I_0)^{1/2} \cdot$$

$$= I_\varepsilon/2(I_dI_0)^{1/2} \qquad . \qquad\qquad\qquad (\text{III-10})$$

Equation (III-10) is just equation (6-1) presented in Chapter 6.

APPENDIX IV

NUMERICAL METHOD AND PHYSICAL PARAMETERS

Numerical Calculation for the Space-Charge Field

The equation of space-charge field is time dependent second-order differential equation, the form of which is

$$d^2E_1(t)/dt^2 + A(t)\, dE_1(t)/dt + B(t)\, E_1(t) = C(t)$$

where $E_1(t)$, $A(t)$, $B(t)$ and $C(t)$ are all complex.

Firstly, we have to separate the real and imaginary part of the above equation.

Secondly, we must separate the second-order differential equation into two first-order differential equations by a change in variables.

Thirdly, we utilize Euler's method as a numerical method for solving differential equation.

Fourthly, we write a C program to generate the numerical solution.

Physical Parameters Used for Computer Programs

Dielectric constant $\epsilon = 3000$

Temperature $T = 300\ k$

Optical wavelength $l = 4580\ A^\circ$

181

Photoionization cross section $s = 5 \cdot 10^{-18}$ cm^2

Recombination coefficient $\gamma_R = 1 \cdot 10^{-9}$ cm^3/s

Mobility $\mu = 0.5$ cm^2/vs

Full crossing angle $2\theta = 10°$

APPENDIX V

COMPUTER PROGRAM FOR CALCULATING
PHOTOREFRACTIVE SPACE-CHARGE FIELD

```c
/* Program:  Space-charge field with applied square-wave AC field.c */

#include <stdio.h>
#include <math.h>
#include <stdlib.h>
void main(void)

{
  int i, points=250000, j, l, m;
  long double const0=3.861935e+1, Tplus=8.0e-9, s=5.0e-19, gammaR=2.5e-8,
              gammaRNA=1.25e+8, mu=5.0e-1, k=5.0e+3, NDminusNA=5.0e+16,
              const1=1.66e+9, I0, omega, Tc, TD, hc=1.988e-15, n0, const2, Tdi, TI,
              TE, A1, A2, B1, B2, C1, C2, lemda=4.58e+3, I=2.4e+1, E0=3.0e+3,
              delt=7.0e-9, RE=0.0e+0, IE=0.0e+0, dRE, dIE;
  static long double ReE1[5000], ImE1[5000];

  I0=I*lemda/hc;
  n0=s*I0*(NDminusNA)/(gammaRNA);
  TD=const0/(mu*k*k);
  Tdi=const1/(mu*n0);
  TI=1/(s*I0+(gammaR)*n0);
  TE=1/(k*mu*E0);
  Tc=Tdi*((1+Tplus/TD)*(1+Tplus/TD)+(Tplus/TE)*(Tplus/TE))/
    ((1+Tplus*Tdi/(TD*TI))*(1+Tplus/TD)+Tplus*Tplus*Tdi/(TE*TE*TI));
  omega=(Tplus/TE)*(Tdi/TI-1)/
      (Tdi*((1+Tplus/TD)*(1+Tplus/TD)+(Tplus/TE)*(Tplus/TE)));
  const2=s*I0*((NDminusNA)-n0)/(const1*k);
  A1=1/TD+1/Tdi+1/Tplus;
  A2=1/TE;
  B1=1/(TD*TI)+1/(Tplus*Tdi);
  B2=1/(TI*TE);
  C1=-const2/TE;
  C2=const2/TD;
  dIE=(C2*A1-C1*A2)/(A1*A1+A2*A2);
  dRE=(C1*A1+C2*A2)/(A1*A1+A2*A2);
  ReE1[0]=0.0e+0;
  ImE1[0]=0.0e+0;
  for (l=0; l<=360; l++)
```

```c
  {
  for (i=(2*l*points); i<((2*l+1)*points); i++)
     {
     RE=RE+delt*(dRE);
     dRE=dRE+delt*(C1-A1*dRE+A2*dIE-B1*RE+B2*IE);
     IE=IE+delt*(dIE);
     dIE=dIE+delt*(C2-A1*dIE-A2*dRE-B2*RE-B1*IE);
     }
  ReE1[2*l+1]=RE;
  ImE1[2*l+1]=IE;
  printf("\n%5d   %Le        %Le", (2*l+1), ReE1[2*l+1], ImE1[2*l+1]);
  for (j=((2*l+1)*points); j<(2*(l+1)*points); j++)
     {
     RE=RE+delt*(dRE);
     dRE=dRE+delt*(-C1-A1*dRE-A2*dIE-B1*RE-B2*IE);
     IE=IE+delt*(dIE);
     dIE=dIE+delt*(C2-A1*dIE+A2*dRE+B2*RE-B1*IE);
     }
  ReE1[2*l+2]=RE;
  ImE1[2*l+2]=IE;
  printf("\n%5d   %Le        %Le", (2*l+2), ReE1[2*l+2], ImE1[2*l+2]);
     }
  printf("\n\n");
}
```